

**A RAPID-SCAN OPTICAL INTERFEROMETRIC CROSS-CORRELATOR
FOR TIME-RESOLVED LASER SPECTROSCOPY**

by

RONG ZHU

B.S., Zhongshan University, P. R.China, 1983.

M.S., Anhui Institute of Optics and Fine Mechanics,
Academia Sinica and the University of Science
and Technology of China, P. R. China, 1986

A THESIS SUBMITTED IN PARTIAL FULFILLMENT
OF THE REQUIREMENTS FOR THE DEGREE
OF MASTER OF APPLIED SCIENCE

in

THE FACULTY OF GRADUATE STUDIES

DEPARTMENT OF ENGINEERING PHYSICS

We accept this thesis as conforming
to the required standard

THE UNIVERSITY OF BRITISH COLUMBIA

April 1995

© Rong Zhu, 1995

In presenting this thesis in partial fulfilment of the requirements for an advanced degree at the University of British Columbia, I agree that the Library shall make it freely available for reference and study. I further agree that permission for extensive copying of this thesis for scholarly purposes may be granted by the head of my department or by his or her representatives. It is understood that copying or publication of this thesis for financial gain shall not be allowed without my written permission.

Department of

Physics

The University of British Columbia
Vancouver, Canada

Date

Apr. 28, 1995

ABSTRACT

The rapid progress of short pulse laser technology has provided a concomitant increase in the use of ultrashort lasers for the characterization of the optical and electronic properties of semiconductor nanostructures and devices. As the characteristic timescale of the phenomenon under investigation approaches the optical pulse width that is used, it becomes increasingly important to be able to fully characterize the amplitude and phase of the pulses before and after interacting with a sample in any given experiment. Towards this end, we designed and developed a computerized optical interferometric cross-correlator for femtosecond time-resolved laser spectroscopy, which can be used to extract amplitude and phase information from pulses used to probe a variety of systems.

This electro-optical system, which we refer to as the rapid scan interferometric cross correlation system (RICCS), consists of a femtosecond Ti:sapphire laser source, a custom Mach-Zehnder interferometer for cross correlations, a continuous wave (cw) HeNe laser and a Michelson interferometer for relative path delay decoding, linear optoelectronic detection, electronic processing, computerized device control, and signal acquisition and data analysis. A novel aspect of this system is the use of a mirror mounted on an audio speaker as a rapid scanner to provide the relative path delay between the reference beam and signal beam in the Mach-Zehnder interferometer. Interferograms with up to 500 fringes each scan can be acquired by the computer at rates up to 25 scans per second.

This thesis describes the principles of the operation of this RICCS system, its implementation, and its use in both auto-correlation and cross correlation modes.

TABLE OF CONTENTS

Abstract		ii
Table of Contents		iii
List of Tables		v
List of Figures		vi
Acknowledgement		xi
Chapter 1.	Introduction	1
1.1	Background	1
1.2	Detection of Optical Pulse Breakup in Propagation through Semiconductor Quantum Wells	3
1.2.1	Non-Interferometric Detection	4
1.2.2	Interferometric Detection	6
1.3	Implementation	7
Chapter 2.	Basic Principles	10
2.1	Introduction	10
2.2	Detection	12
2.3	Determination of the Relative Path Delay	16
2.4	Signal Measurement	18
2.5	Sample and Hold Considerations	24
2.6	Signal Pulse Recovery	25
Chapter 3.	System Design	28
3.1	General Description	28
3.2	Interferometers	30
3.3	Laser System	31
3.4	Electronic Signal Processing (Hardware)	32
3.4.1	Impedance matching	33
3.4.2	Computer Board	39
3.4.3	Differential Input Package	40
3.5	Electronic Signal Processing and Analysis (software)	41
3.5.1	Introduction to Labview™	41
3.5.2	Introduction to the Software Package	42
3.5.3	Device Driver	44
3.5.4	DAQ VIs	48

3.5.5	VIs for the Decoding Channel	49
3.5.6	VIs for the Signal Channel	53
Chapter 4.	System Performance	57
4.1	Determination of Relative Path Delay	57
4.1.1	Decoding Error from Sampling	61
4.1.2	Decoding Errors due to the Noises in the Reference Interferogram	62
4.1.3	Decoder Parameter Testing	65
4.2	Signal Interferogram	68
4.2.1	Linear Interferograms	68
4.2.2	Nonlinear Interferograms	79
4.2.3	Power Spectrum of the Reference Pulses	81
4.3	Characterization of Ti:sapphire Laser Output: Auto-Correlator	82
4.3.1	Evolution of Mode-Locking Status	84
4.3.2	Center Wavelength and Pulse Duration	86
4.4	Cross-Correlator	89
4.4.1	Interferogram	89
4.4.2	Analysis	96
Chapter 5.	Conclusions and Suggestions	101
5.1	Conclusions	101
5.2	Recommendations for Future Development	102
References		104
Appendix A.	Configuration for Pump/probe Interferometric Measurement	107
Appendix B.	Synchronized Pump Beam Chopper Package	109

Software package developed in Labview for Windows is enclosed.

LIST OF TABLES

Table 4.1	Test results for reliable decoding at different speaker drive frequencies.
-----------	--

LIST OF FIGURES

Fig. 1.1	A generic experimental setup for carrying out pump-probe experiments.	2
Fig. 1.2	(a) Time-integrated up-conversion signals: no pump pulses for solid line and with -20 ps delayed pump pulses for dash line. (b) the interferogram without pump pulse. (c) showing an expanded view of (b) (solid) and also a sine simulation of the interferogram without pump pulse (dashed)(From Ref.20).	5
Fig. 1.3	Two typical approaches to implement interferometric measurements. (a). the approach with active feedback. (b). the rapid-scan approach without active feedback.	8
Fig. 2.1	(a) Modified Mach-Zehnder Interferometer for Pulsed Signal Processing. (b) Michelson Interferometer for Relative Delay Decoding. The basic components of the interferometers include beam splitters, fixed and oscillating mirrors, a nonlinear optical crystal (optional), and photodiodes. The beam paths shown as solid lines include a variable delay line that is periodically modulated in length. The dashed beam paths are fixed in length. The two separate beams are combined through polarizing beam splitters at the output ports.	11
Fig.2.2	Equivalent circuit for electrical conditioning between the detector and the sample-and-hold amplifier.	13
Fig.2.3	A schematic diagram of the real time interferogram from the relative path delay decoding interferometer. This was simulated for a 900 nm cw laser source, a scanning period of 25 Hz and a scan range of ± 100 fs.	15
Fig.3.1	System schematic for the optical interferometers and the optoelectronic detection. The components within the dashed box comprise the Michelson interferometer, those within the dashed-dotted box comprise the Mach-Zehnder interferometer, and those within the dotted box are for nonlinear interferometric detection.	29
Fig.3.2	Beam Path for fsec Tsunami Configuration.	31

Fig.3.3	Schematic diagram of the interface. AI stands for analog input channel, DAC stands for data signal output channel, and DAQ stands for data acquisition.	33
Fig.3.4	(a) The real time interferogram for the HeNe laser source, from D1, before impedance matching. (b) The real time interferogram for the cw Ti:sapphire laser source, from D2, before impedance matching.	34
Fig.3.5	Electrical circuit for signal channel with impedance matching.	35
Fig.3.6	(a) The frequency response of the signal conditioning for decoding channel at different matching impedences for fixed input from the Michelson interferometer. (b) The frequency response of the signal conditioning for signal channel at different matching impedences for fixed input from the Michelson interferometer.	37
Fig.3.7	(a) The relative signal amplitude at the output of the matching circuit of the decoding channel for fixed input from the Michelson interferometer, at the frequency of 20 kHz, for different matching impedences. (b) The relative signal amplitude at the output of the matching circuit of the signal channel for fixed input from the Michelson interferometer, at the frequency of 20 kHz, for different matching impedences.	38
Fig.3.8	Differential input configuration.	40
Fig.3.9	Flow diagram for the software package.	43
Fig.3.10	The block diagram for Generate Sig. & Sync.vi.	46
Fig.3.11	The panel for Generate Sig. & Sync.vi.	47
Fig.3.12	Two scan cycles of the real time interferogram from Ch0 corresponding to one round trip of the scanner.	51
Fig.3.13	The schematic diagram showing the moving windows on both sides of a turning point.	52
Fig.4.1	(a) A single cycle real time interferogram generated by the relative path delay interferometer.	

	(b) The time dependent relative path delay decoded from the interferogram in Fig.4.1(a).	58
Fig.4.2	(a) 4 cycle real time interferogram from relative path delay decoding interferometer, and (b) its decoded relative path delay in real time space. (c) and (d) its scale-expanded relative path delay near the turning points of the speaker's motion in real time space.	59
Fig.4.3	The real time interferogram in the low frequency region generated by the relative path delay decoding interferometer.	60
Fig.4.4	The error in relative path delay decoding in the full relative path delay range.	64
Fig.4.5	(a) The relative path delays deduced from a real time interferogram generated by the relative path delay decoding interferometer with scanning frequency of 10 Hz, and (b) the worst part in the decoding above.	66
Fig.4.6	(a) Effects of too high scanning frequency: the relative path delays deduced from a real time interferogram generated by the relative path delay decoding interferometer with scanning frequency of 25 Hz but the same scanning amplitude as that in Fig.4.6, and (b) the worst part of the relative path delay decoding above.	67
Fig.4.7	(a) A linear signal interferogram in real time space with a speaker frequency of 25 Hz and an amplitude of 0.065 V.	69
Fig.4.7	(b) The linear signal interferogram in relative path delay space converted from the real time interferogram in Fig.4.8(a).	70
Fig.4.8	The interferogram consisting of samples from 8 cycles of the scanner.	72
Fig.4.9	(a) The interferogram averaged from the 8 cycle interferogram generated by the signal generating interferometer with an averaging window width of 0.2fs.	73
Fig.4.9	(b) The polynomial simulation of the interferogram in Fig.4.9 (a).	74
Fig.4.9	(c) The interferogram in Fig.4.9 (a) and its polynomial simulation in expanded scale.	75

Fig.4.9	(d) The residuals of the polynomial simulation of the interferogram in Fig.4.9 (a).	76
Fig.4.10	Quantitative evaluation of the efficiencies of the multicycle averaging method on noise reduction.	78
Fig.4.11	The nonlinear signal interferogram in relative path delay space with a speaker frequency of 25 Hz and an amplitude of 0.065V.	80
Fig.4.12	The intensity spectrum of a 70 fs pulse with center wavelength of 805.1 nm from the FFT of the interferogram generated by this system and that obtained by the FTIR from Bomem Co.	82
Fig.4.13	(a) The interferogram in relative path delay space generated from a poor mode-locked Ti:sapphire laser output. (b) the interferogram in relative path delay space generated from a better mode-locked Ti:sapphire laser output.	85
Fig.4.13	(c) the interferogram in relative path delay space generated from a well mode-locked Ti:sapphire laser output.	86
Fig.4.14	Center wavelength calibrations of the output pulses from a Ti:sapphire laser implemented by this system and the FTIR from Bomem Co.	87
Fig.4.15	Pulse durations from a well mode locked Tisapphire laser at different center wavelegths.	88
Fig.4.16	The autocorrelation interferogram from the pulse of duration τ_p of 75 fs and λ_c of 790.45 nm.	90
Fig.4.17	The cross correlation interferogram from the pulse of $\tau_p=75$ fs and $\lambda_c=790.45$ nm with 4 mm piece of quartz glass inserted in the signal path.	91
Fig.4.18	The cross correlation interferogram from the pulse of $\tau_p=75$ fs and $\lambda_c=790.45$ nm with 8 mm piece of quartz glass inserted in the signal path.	92
Fig.4.19	The envelopes of the interferograms in Fig.4.16, Fig.4.17 and Fig.4.18.	93

Fig.4.20	The phase shifts in the interferograms in Fig.4.16, Fig.4.17 and Fig.4.18.	94
Fig.4.21	The difference between the envelope of the cross correlation interferogram with glass and that without glass as a function of the relative path delay.	95
Fig.4.22	The refractive index n of quartz glass (fused silicon) in the region around the center wavelength $\lambda_c = 790.45$ nm of the laser pulse.	96
Fig.A1	System schematic for pump/probe interferometric measurement.	108
Fig.B1	Synchronized chopper package.	109
Fig.B2	(a) The input waveform to the synchronized chopper package at 50 Hz. (b) The output waveform from the synchronized chopper package at 50 Hz.	111

ACKNOWLEDGEMENT

I would like to thank my supervisor, Dr. Jeff Young. His great assistances in all aspects enable me to succeed in fulfilling my M.A.Sc. program. Without his insightful advice and his research experience, the outcome from this research will never have been achieved. I would also like to thank Dr. John Eldridge for reading of this thesis. As well, I would like to give a big thank to Alex Busch and Paul Paddon for their great help in the preparation of this thesis, and to Isaac Leung for help with initial software development.

CHAPTER 1. INTRODUCTION

1.1 BACKGROUND

The rapid progress of short-pulse laser technology has enabled a concomitant increase in the use of ultrashort laser pulses for studying a variety of transient phenomena directly in the time domain. Titanium sapphire (Ti:sapphire) lasers capable of stably producing pulses of duration less than 75 fs in the near infrared part of the electromagnetic spectrum are now commercially available. Microscopic timescales characteristic of technologically important materials such as semiconductors (eg. silicon, gallium arsenide, etc.) are comparable to these pulse durations (eg. the period of an optical phonon vibration is ~ 150 fs, the time for an energetic electron to emit an optical phonon is ~ 200 fs, and the time for electron-electron scattering to thermalize a nonequilibrium electron population is between 10 fs and 10 ps depending on the density of the electrons) [Ref.1-5]. Many of these materials have band gaps that overlap the tuning range of the Ti:sapphire laser system.

Numerous optical techniques have been developed to take advantage of this situation to study a number of fascinating phenomena [Ref.1-13]. The majority of these techniques are based on the so-called "pump-probe" approach in which a pump pulse is used to excite the sample under study, and a probe pulse, synchronized with femtosecond resolution to the pump pulse, is used to time-resolve some dynamic response of the excited system. The majority of these pump-probe techniques, some of which are briefly summarized below, measure the time-integrated or time-resolved amplitude of the response as a function of the pump-probe delay time. However, the fact that 75 fs represents only 25 optical periods at a vacuum wavelength of 900 nm motivates the development of interferometric techniques that can monitor both the amplitude and phase of the

probe response [Ref.14-24]. The purpose of this thesis work was to develop and test a relatively simple and inexpensive method of achieving this goal.

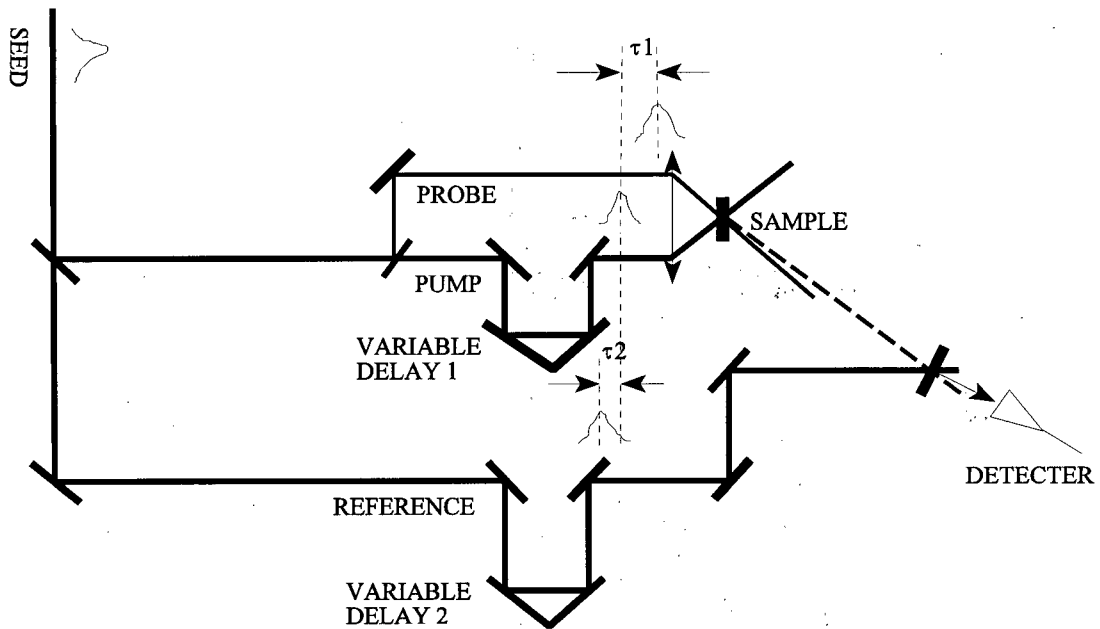


Fig.1.1 A Generic Experimental Setup for Carrying out Pump-Probe Experiments.

A generic experimental setup for carrying out pump-probe optical experiments is schematically illustrated in Fig. 1.1. The pump, probe, and reference pulses can all be derived from a single seed pulse by the use of beam splitters and coherent frequency conversion techniques. Their relative arrival times at any given position are typically limited by mechanical vibrations to a few optical wavelengths (corresponding to ~ 10 fs). The pump pulse typically modifies the equilibrium properties of the material by exciting real and/or virtual elementary excitations, the presence of

which modifies its reflection, transmission, diffraction, and/or emission properties. The pulse delayed by a time τ_1 with respect to the pump pulse is used to probe one or more of these modified properties in order to infer the temporal dynamics of the excitations induced by the pump pulse. In some instances, a third pulse, delayed by τ_2 with respect to the pump pulse, is used to gate the detection of delayed emissions from the excited volume of the sample. We distinguish between two types of pump-probe experiments according to whether or not they incorporate an optical phase sensitive detection system. Non-interferometric techniques are capable of temporally and/or spectrally resolving the intensity of the emission from the sample that results from the application of the pump and probe pulses. All information regarding the phase of the emitted light is lost. Techniques that incorporate some sort of custom interferometer (optical phase sensitive element) can, in principle, extract the maximum available information about the amplitude and phase of the actual electric field emanating from the sample.

To illustrate the additional insight that can be gained by extracting both amplitude and phase information from the signal beam, the following two sections briefly describe two published measurements of the distortion of femtosecond pulses that results from propagation through semiconductor quantum well samples. Section 1.2.1 and 1.2.2 describe non-interferometric and interferometric measurements, respectively.

1.2 DETECTION OF OPTICAL PULSE BREAKUP IN PROPAGATION THROUGH SEMICONDUCTOR QUANTUM WELLS

In most studies of semiconductors and their nanostructures using picosecond pulsed spectroscopes, the results are analyzed assuming that the pulse shape distortion in the sample can

be ignored. With femtosecond laser pulses, the distortion can become important, especially when the pulse spectrum overlaps the resonances in the material response.

Kim, et. al. [Ref. 20] recently demonstrated the pulse breakup phenomena that can occur when 150 fs pulses propagate through semiconductor multiple quantum well (MQW) samples that have an excitonic resonance near the frequency of the laser pulses. This produces a nice example that illustrates the utility of obtaining both amplitude and phase information from pump/probe experiments..

1.2.1 NON-INTERFEROMETRIC DETECTION

In the first instance, Kim, et. al. used a non-interferometric up-conversion technique to measure the temporal evolution of the probe pulse transmitted through a MQW. The set-up is similar to that in Fig. 1.1. A passively mode-locked, tunable Ti:sapphire laser with 150 fs pulse duration was used as the seed pulse. The pump pulse was used to change the exciton and free-carrier populations and thus to modulate the exciton dephasing time T_2 . The low intensity probe pulse propagated through the region that was irradiated by the pump pulse in the sample. Then the transmitted pulse overlapped with the reference pulse in a nonlinear crystal to generate a frequency up-converted signal [Ref. 5]. The time-integrated up-converted emission was proportional to the intensity of the reference pulse and that of the transmitted pulse. By tuning the optical delay, τ_2 , between the reference pulse and the transmitted pulse, the temporal evolution of the amplitude of the transmitted probe pulse was determined.

Fig. 1.2 (a) shows one of the results. This is the temporal evolution of the probe pulse amplitude transmitted through a GaAs MQW sample [Ref. 5] at a temperature of 10 K with the

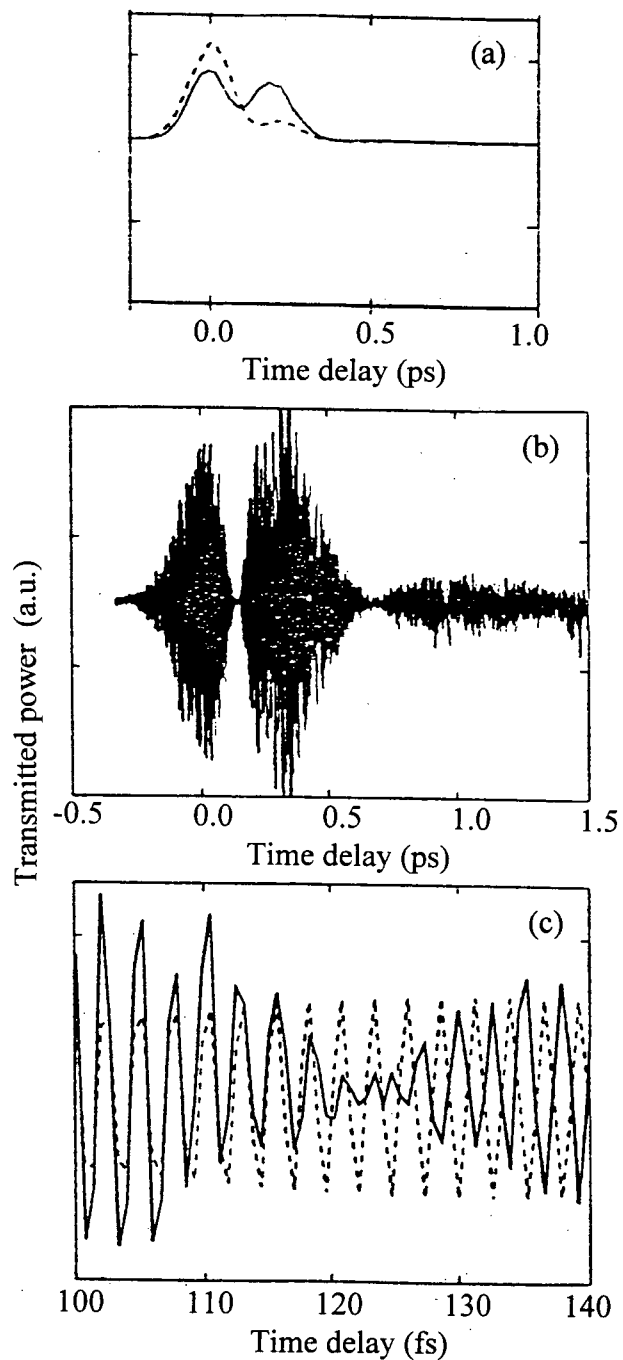


Fig.1.2 (a) Time-integrated up-conversion signals: no pump pulses for solid line and with -20 ps delayed pump pulses for dash line. (b) the interferogram without pump pulse. (c) showing an expanded view of (b) (solid) and also a sine simulation of the interferogram without pump pulse (dashed) (From Ref.20).

laser centered on the heavy hole exciton resonance. The solid line shows the result without the pump pulse and the dashed line shows that with the pump pulse delayed by -20 ps relative to the probe pulse. These results demonstrate the break-up of the transmitted pulse: the initial peak is followed by a tail consisting of another peak that is comparable to the initial peak amplitude. The introduction of the pump pulse increases the intensity of the initial peak and shortens the tail. This suggests that the signal is due to free-induction decay (FID), because it is well-known that an increase of the exciton and free-carrier populations leads to a reduction in the exciton dephasing time, T_2 . The interferometric measurement of the transmitted pulses, described in the next section, provides additional information about the phase evolution of the transmitted pulses, which unequivocally demonstrates that the signal is due to FID.

1.2.2 INTERFEROMETRIC DETECTION

In this example, the interferometric detection was done by putting the sample in one arm of a modified Michelson interferometer and no pump pulse was used. The other arm of the interferometer carries the reference beam. The output signal is then due to the light field formed by collinearly superimposing the fields of the reference beam and the transmitted beam from the sample. The interference pattern detected as a function of the relative delay between the two arms of the interferometer therefore provides information on both the amplitude and the phase of the transmitted pulses in a way that is described in other chapters of this thesis.

Fig. 1.2 (b) shows the interference pattern between the original and the distorted pulses for the sample studied by non-interferometric detection, excited at the heavy hole resonance at 10 K. The horizontal axes is the variable optical delay between both arms in the interferometer provided

by a translation stage. The envelope of the pattern clearly repeats the feature obtained in the temporal evolution measurement using non-interferometric detection; there are three peaks, the intensity of the second peak is comparable to the initial peak, and the break-up is aperiodic. However, with the phase sensitive detection the two nodes are much clearer. Closer examination of the first nodal region and fits of the prenodal and postnodal interference patterns to sinusoidal waves reveal a change of sign (or π phase change) at the node as shown by Fig. 1.2 (c). With the sample removed, and with appropriate adjustment of the delay, neither the nodes nor the phase shift are present.

The phase shift comes from the fact that at resonance, the polarization of the medium is $\pi/2$ out of phase with the incident radiation, and the reradiation from this induced polarization is another $\pi/2$ out of phase. A slight detuning of the laser from resonance shows that, indeed, the trailing part of the pulse has the frequency of the exciton resonance, whereas the frequency of the leading part is determined by the center laser frequency (i.e. the frequency in the transmitted pulse has a instantaneous jump around the node.). The additional information from the interferometric detection allows an unequivocal association of the pulse break-up with the reradiation from the induced polarization.

1.3 IMPLEMENTATIONS

There are two basic ways of implementing an interferometric cross correlator. The first, which to our knowledge is the only approach that has been reported to date, is to set up a stable Mach-Zender type interferometer that incorporates active feedback to fix the relative path lengths to within a fraction of an optical fringe. The delay between the reference and the probe paths in the

interferometer is controlled by moving one mirror in an optical delay line using a computer controlled translation stage (Fig.1.3 a). The output signal is averaged for some period of time and then the delay is changed to a new value and the process is repeated. The critical elements in this approach are the high-precision computer-controlled translation stage, and the active feedback mechanisms. A means of counting fringes is also required to obtain the optimum temporal resolution.

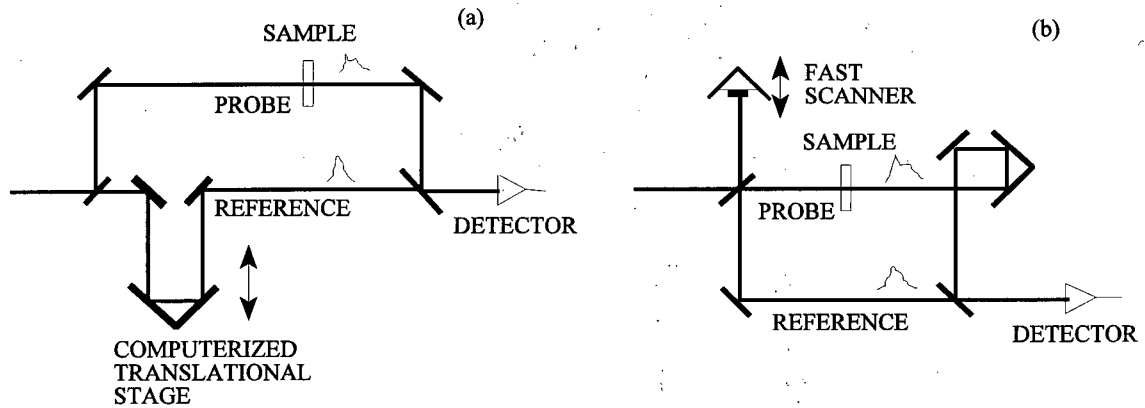


Fig.1.3 Two typical approaches to implement interferometric measurements. (a). the approach with active feedback (b). the rapid-scan approach without active feedback.

An alternative, "rapid-scan" approach is to allow the relative path length to vary without active feedback, and to rapidly scan the relative delay between the reference and probe beams in a periodic fashion (Fig.1.3 b). This requires continuous monitoring of the relative path length in the two arms of the interferometer, which shifts the technological challenge from the servo and translation stage hardware to the electronics and software domain. Given the rapidly evolving

capabilities of electronics and software technology, it seems that this latter approach might offer a simpler, more flexible, and more economical solution in the long term.

The work reported in this thesis summarizes the development and testing of what to our knowledge is the first rapid-scan interferometric cross correlator for use in femtosecond pulsed spectroscopy. The basic principles behind the design are described in Chapter 2. The optical, electrical, and software components of the system are described in detail in Chapter 3. Chapter 4 describes various tests performed on the system using ~ 75 fs pulses from a commercial Ti:sapphire laser system, while Chapter 5 summarizes the findings and discusses the potential and limitations of the apparatus.

CHAPTER 2. BASIC PRINCIPLES

2.1 INTRODUCTION

The main purpose of the system developed in this work is to measure the amplitudes and phases of pulsed optical signals in the time domain by using optical interferometric correlation techniques. To achieve this goal a Mach-Zehnder interferometer, which we call the signal generating interferometer, is used to collinearly and coherently superimpose reference and signal fields that have a sinusoidally varying relative phase shift (see Fig.2.1(a)). The properties of the superposition field at the output of the interferometer can then be characterized using square-law photodiodes to detect the interferogram of the raw signal, or the nonlinear optical signal produced by passing the superposition field through a nonlinear optical crystal (a harmonic generation process). In the ideal case where the reference beam consists of a transform limited optical pulse, the amplitude and phase of the signal beam can be extracted by processing the linear correlation signal.

The technique requires that the relative path lengths between the two arms of the signal generating interferometer be known within a fraction of an optical wavelength at all times while data is being collected from the detector in this interferometer. This information can be obtained by monitoring the interferogram produced by a continuous wave laser that passes through both arms of a Michelson interferometer that uses the same moving mirror as the signal generating interferometer (see Fig.2.1 (b)). We call this Michelson interferometer the relative delay decoding interferometer.

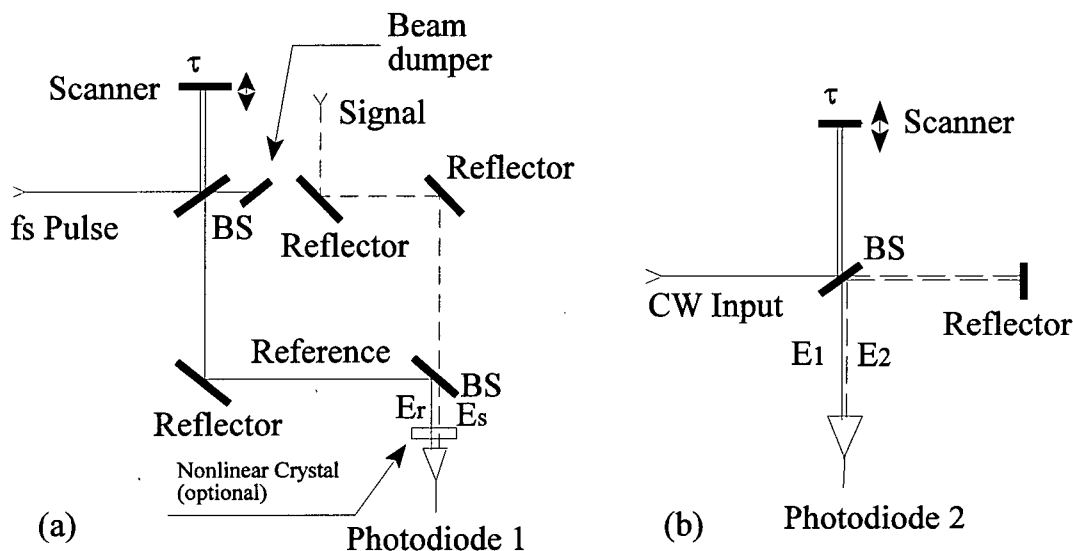


Fig.2.1 (a) Modified Mach-Zehnder Interferometer for Pulsed Signal Processing. (b) Michelson Interferometer for Relative Delay Decoding. The basic components of the interferometers include beam splitters, fixed and oscillating mirrors, a nonlinear optical crystal (optional), and photodiodes. The beam paths shown as solid lines include a variable delay line that is periodically modulated in length. The dashed beam paths are fixed in length. The two separate beams are combined through polarizing beam splitters at the output ports.

The remainder of this chapter is organized as follows. The optoelectronic conversion of the optical fields to electrical current by the photodiodes is described in Sect. 2.2. Sect. 2.3 describes the way in which the relative delay decoding interferometer is used to determine the relative path delay, and Sect. 2.4 describes how the signal generating interferometer is used to deduce the amplitude and phase of the signal field given a transform-limited reference pulse and the relative delay information. Throughout the thesis it is assumed that all optical pulses contain sufficient photons to justify a classical treatment of the electromagnetic field.

2.2 DETECTION

The photodiodes used in this system are square-law detectors. This means that, $I(t)$, the short-circuit electrical current generated by an optical field, $E_{total}(t, x, y)$, incident on the photodiode plane is given approximately by the rate equation [Ref.28]:

$$T' \frac{dI(t)}{dt} + I(t) = \frac{\eta e}{h\nu} \iint_D dx dy |E_{total}[t, \tau(t), x, y]|^2 \quad (2.1)$$

where $T' = T_r T_t / (T_r + T_t)$ is the response time of the photodiode expressed in terms of the recombination time, T_r , and the effective carrier transit time, T_t , η is the quantum efficiency, D is the area of the photodiode, $h\nu$ is the average energy of each photon in the optical field, $\tau(t)$ is the relative delay in the arrival time of the two fields due to the scanner, and e is the charge of an electron.

Eqn.(2.1) has a solution,

$$I(t) = \frac{\eta e}{h\nu T'} \int_{-\infty}^t dt' \exp[-(t-t')/T'] \iint_D dS |E_{total}[t', \tau(t'), x, y]|^2. \quad (2.2)$$

In practice the fields at the detector surface are approximately constant over the active area of the photodiode so we take

$$I(t) = \frac{\eta e D}{h \nu T'} \int_{-\infty}^t dt' \exp[-(t-t')/T'] |E_{total}[t', \tau(t')]|^2. \quad (2.3)$$

In the frequency domain, the short-circuit current can be expressed in terms of its Fourier transform,

$$\hat{I}(s) = \frac{\eta e D}{h \nu T'} \frac{1}{s + \frac{1}{T'}} \mathcal{F}\{|E_{total}[t, \tau(t)]|^2\} \quad (2.4)$$

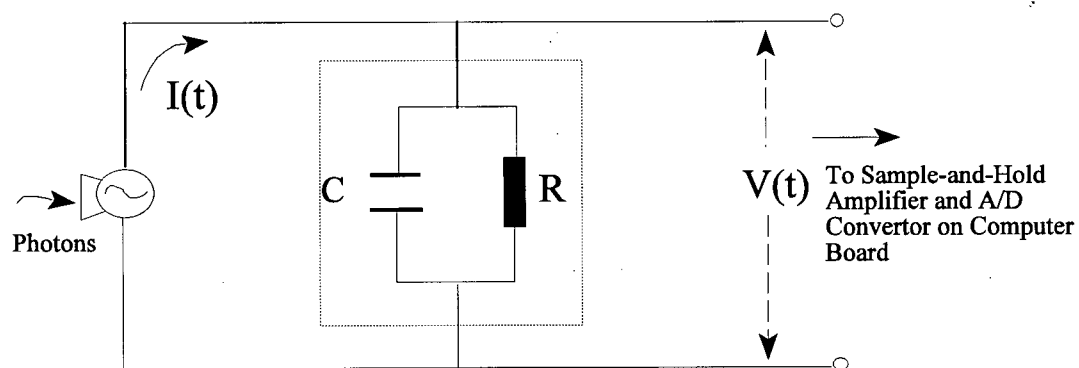


Fig.2.2 Equivalent circuit for electrical conditioning between the detector and the sample-and hold amplifier.

where $s=i\omega$, and the last term on right hand side is the Fourier transform of $|E_{\text{total}}(t, \tau)|^2$, which we refer to as $\hat{J}(s)$.

The signal from the photodiode is put through a simple signal conditioning circuit and then it is sampled by a sample-and-hold (SAH) circuit that interfaces with a computer. A schematic equivalent circuit is shown in Fig.2.2.

The voltage signal seen at the SAH is therefore given in the frequency domain by

$$\hat{V}(s) = \frac{\eta e D}{h\nu C T'} \frac{1}{s + \frac{1}{RC}} \frac{1}{s + \frac{1}{T'}} \hat{J}(s) \quad (2.5)$$

with R and C being the equivalent resistance and capacitance between the photodiode and the SAH.

The objective is to record faithful representations of the homodyne components of $\hat{J}(s)$ that carry the information required to i) accurately determine the relative path delay $\tau(t)$ in the relative path delay decoding interferometer, and ii) deduce the cross correlation of the reference and signal pulses in the signal generating interferometer. The following two sections develop expressions for $\hat{J}(s)$ for the two interferometers. The components of these signals that are needed to extract the complex field amplitude and phase in the signal arm of the Mach-Zehnder interferometer are identified. The frequency content of these signals determines the choice of detectors, and the matching circuitry.

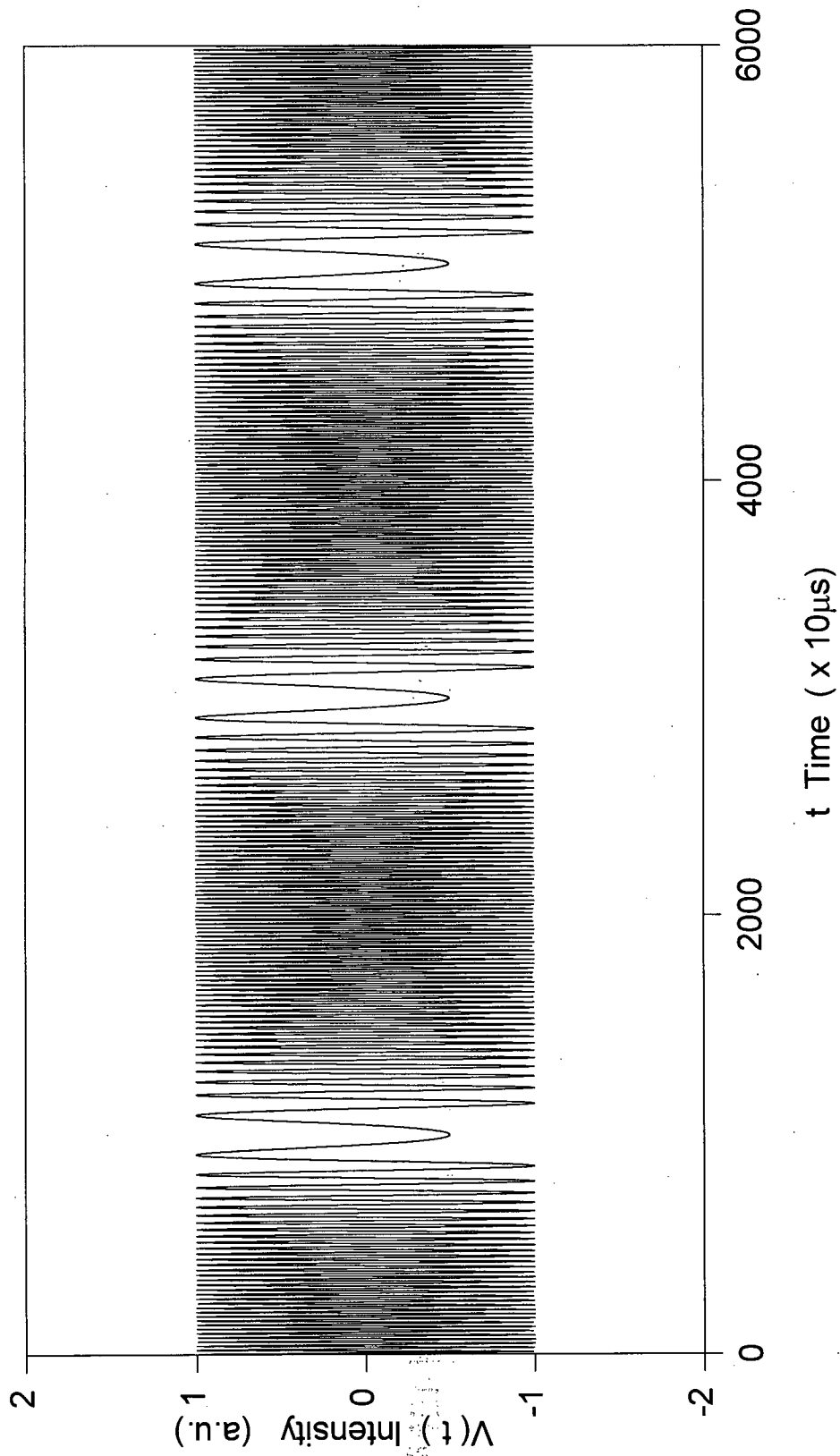


Fig.2.3 A schematic diagram of the real time interferogram from the relative path delay decoding interferometer. This was simulated for a 900 nm cw laser source, a scanning period of 25 Hz and a scan range of ± 100 fs.

2.3 DETERMINATION OF THE RELATIVE PATH DELAY

In the relative path delay (RPD) decoding interferometer, for a periodically varying path length difference between the two arms (sinusoidal with period T in the present system), the signal $V(t)$ at the SAH input is a periodic function with high-frequency oscillations as schematically illustrated in Fig. 2.3. As the scanned mirror position changes by one half of the cw laser wavelength, an interference fringe is generated. The signal can therefore be used to deduce the RPD once it is stored in the computer.

Because the coherence length of the cw laser is much longer than the range of the moving mirror, the total field at the output of the RPD decoding interferometer can be expressed as

$$E_{rtotal}(t, \tau(t)) = E_1(t) + E_2(t + \tau(t)) \quad (2.6)$$

where the fields with frequency ω_r from two different arms have time independent amplitudes and phases:

$$\begin{aligned} E_1(t) &= f_1 \cos[\omega_r t] \\ E_2(t) &= f_2 \cos[\omega_r t] . \end{aligned} \quad (2.7)$$

In the following development we treat the noise-free, ideal situation and use the fact that the fields are essentially uniform over the area of the photodiode.

We begin by substituting Eqn. (2.7) into Eqn. (2.6) to get:

$$\begin{aligned}
|E_{rtotal}(t)|^2 = & \frac{f_1^2}{2} + \frac{f_2^2}{2} + f_1 f_2 \cos[\omega_r \tau(t)] + \frac{f_1^2}{2} \cos[2\omega_r t] \\
& + \frac{f_2^2}{2} \cos[2\omega_r t + 2\omega_r \tau(t)] + f_1 f_2 \cos\left[\omega_r t + \frac{\omega_r \tau(t)}{2}\right] .
\end{aligned} \tag{2.8}$$

The optical frequency components are completely averaged by the square-law detector and signal conditioning circuitry, so we can immediately simplify Eqn.(2.8) to the form used to generate the signal shown in Fig.2.3. One obtains,

$$|E_{rtotal}(t)|^2 = \frac{f_1^2}{2} + \frac{f_2^2}{2} + f_1 f_2 \cos[\omega_r \tau(t)] . \tag{2.9}$$

$|E_{rtotal}(t)|^2$ contains frequency components ranging from DC up to $\omega_{\max} = \max[d(\omega_r \tau(t))/dt]$, the maximum instantaneous frequency of the cosine term. By designing the signal conditioning circuits and choosing the proper detector, we can acquire a signal $V_r(t)$, which is proportional to $|E_{rtotal}(t)|^2$ below ω_{\max} . We do this by choosing RC and T', such that their transfer functions $1/(s+1/RC)$ and $1/(s+1/T')$ have cutoff frequencies well above ω_{\max} , and by choosing an appropriately high sampling frequency. The resulting signal, $V_r(t)$, being proportional to $|E_{rtotal}(t)|^2$, is used to deduce $\tau(t)$ by

$$\tau(t) = \frac{1}{\omega_r} \arccos \left(\frac{V_r(t) - \frac{(V_{rmax} + V_{rmin})}{2}}{\frac{V_{rmax} - V_{rmin}}{2}} \right) \quad (2.10)$$

where $V_{rmax} = (f_1^2 + f_2^2 + 2f_1f_2)\eta eDR/(\hbar\omega_r)$, and $V_{rmin} = (f_1^2 + f_2^2 - 2f_1f_2)\eta eDR/(\hbar\omega_r)$ are the maximum and minimum signal levels in the real time interferogram generated by the relative path delay decoding interferometer, respectively. Eqn.(2.10) is the basic inversion formula used to determine the relative path delay as a function of real time.

2.4 SIGNAL MEASUREMENT

At the output port of the signal generating interferometer, there are two collinearly superimposed fields that independently travel through the reference path, $E_r(t)$, and the signal path, $E_s(t)$. Then the superposition field on detector plane:

$$E_{total}(t) = E_r(t + \tau(t)) + E_s(t) \quad (2.11)$$

Each field consists of a series of ultrashort laser pulses of durations less than 1 ps separated by the round trip time in the laser, $\Delta t \approx 12$ ns.

We can write the total electric field on the photodiode plane as:

$$\begin{aligned}
E_{total}(t) &= \sum_m E_{mtotal}(t) \\
&= \sum_m [E_{rm}(t + \tau(t)) + E_{sm}(t)]
\end{aligned}
\tag{2.12}$$

where $E_{mtotal}(t)$ is the total electric field on the photodiode plane resulting from the m th reference pulse and the m th signal pulse, each assumed to be identical except for its location in time.

$$\begin{aligned}
E_{rm}(t) &= f_r(t - t_m) \cos[\omega_c t + \varphi_r(t - t_m)] \\
E_{sm}(t) &= f_s(t - t_m) \cos[\omega_c t + \varphi_s(t - t_m)]
\end{aligned}
\tag{2.13}$$

where $t_m = m \Delta t$, m being an integer and ω_c is the center frequency of the optical pulses.

In the equation above $f_r(t)$, and $f_s(t)$ are the real, slowly varying amplitudes of a single reference and signal pulse respectively, and $\varphi_r(t)$ and $\varphi_s(t)$ are the corresponding slowly varying phases. Since the pulses are much much shorter than the interpulse separation, $f_r(t)$ and $f_s(t)$ are zero outside $[-\Delta t/2, \Delta t/2]$.

For the purpose of determining the signal field we require knowledge of the correlation, $C(\tau)$, between any two individual reference and signal pulses

$$C(\tau) \triangleq \int_{-\infty}^{+\infty} dt E_{r0}(t + \tau(t)) E_{s0}(t) .
\tag{2.14}$$

In practice this is achieved by varying τ periodically in real time, ie. $\tau = \tau(t)$ periodic with period T , while successive reference and signal pulses (all assumed identical except for their delays) are interferometrically overlapped and effectively integrated by the detector. The detailed analysis of

this process follows.

Combining Eqn.(2.11) and Eqn.(2.12), we can obtain $\hat{J}_s(s) = \mathcal{F}\{|E_{\text{total}}(t)|^2\}$, the Fourier transform of the intensity of the total pulsed field at the detector plane. It is

$$\begin{aligned} \hat{J}_s(s) &= \int_{-\infty}^{+\infty} dt \exp(st) \sum_{m=-\infty}^{+\infty} (E_{rm}^2[t + \tau(t)] + E_{sm}^2[t] \\ &\quad + 2E_{rm}[t + \tau(t)]E_{sm}[t]) \\ &= \sum_{m=-\infty}^{+\infty} \int_{-\infty}^{+\infty} dt \exp(st) (E_{rm}^2[t + \tau(t)] + E_{sm}^2[t] \\ &\quad + 2E_{rm}[t + \tau(t)]E_{sm}[t]) \end{aligned} \tag{2.15}$$

where we have assumed the range of the relative delay is much smaller than 12 ns, the repetitive period of the laser pulse, and therefore we have neglected any overlap between a reference pulse and the signal pulse generated by another reference pulse.

Four groups of very different characteristic frequencies contribute to the $\hat{J}_s(s)$ in Eqn.(2.15). Just as in the previous section, there are optical frequency components that we can immediately dismiss. There are frequency components due to the interference fringes generated due to the sinusoidally varying $\tau(t)$. These are the important components we ultimately want to deal with, however these must be separated from the high frequency modulation due to the femtosecond pulses. Finally, each pulse pair provides an almost instantaneous sampling of the desired interferogram at a very high sampling rate of 1/(12 ns). The following analysis shows how the desired interferogram is obtained at the input to the computer interface.

Substituting Eqn.(2.13) into Eqn.(2.14) shows that the frequency response of $J_s(s)$ ranges from DC to approximately $\omega_{\text{smax}} = \omega_c \max[d\tau(t)/dt]$. The phase shift due to the relative path delay change during the pulse, $\delta_{\text{phase}}(t)$, is

$$\begin{aligned} \delta_{\text{phase}}(t) &\equiv \omega_c \frac{d\tau(t)}{dt} \tau_p \\ &\leq \omega_c \max \left[\frac{d\tau(t)}{dt} \right] \tau_p \end{aligned} \quad (2.16)$$

where τ_p is the pulse duration. For ideal sinusoidal scanning of the moving mirror with period T and amplitude τ_{max} ,

$$\tau(t) = \tau_{\text{max}} \sin \left(\frac{2\pi t}{T} \right) \quad (2.17)$$

Typically, in this system, $T=1/25$ s, $\tau_{\text{max}}=300$ fs, and the optical frequency $\omega_c=2\pi c/800$ nm $\approx 3.8 \times 10^{14}$ rads/sec, and hence the maximum signal frequency is $\omega_{\text{smax}} \approx 20$ kHz and the maximum phase shift is $\delta_{\text{phase}}(t) \approx 1.5 \times 10^{-9} \times 2\pi$ radians. Because $\delta_{\text{phase}}(t)$ is small, we assume the delay during the pulse is constant, and we can set $\tau(t)=\tau(t_m)$ in the integrands in Eqn.(2.15). Similarly, at the low frequencies of interest ($\sim \omega_{\text{smax}} \ll 1/\tau_p$) the phase in the exponential term in Eqn.(2.15) will vary little over each pulse and hence at these frequencies the exponential in Eqn.(2.15) can also be safely evaluated at $t=t_m$. Finally for those frequencies well below the inverse pulse width, we express Eqn.(2.15) as

$$\hat{J}_s(s) \cong \sum_{m=-\infty}^{+\infty} \exp(st_m) \int_{-\infty}^{+\infty} dt (E_{rm}^2[t] + E_{sm}^2[t] + 2E_{rm}[t + \tau(t_m)]E_{sm}[t]). \quad (2.18)$$

Since we assume each pulse in the reference and signal beams is identical except for a m-dependent time delay, we have

$$\hat{J}_s(s) = \sum_{m=-\infty}^{+\infty} \exp(sm\Delta t) \int_{-\infty}^{+\infty} dt' (E_{r0}^2[t'] + E_{s0}^2[t'] + 2E_{r0}[t' + \tau(m\Delta t)]E_{s0}[t']) \quad (2.19)$$

which is a periodic function of ω with a period $2\pi/\Delta t$.

The last term in Eqn.(2.19) is in fact the discrete Fourier transform of the correlation function of interest, Eqn.(2.14), expressed in real time rather than relative path delay. The discreteness merely replicates the continuous Fourier transform of $C(\tau(t))$ at multiples of $2\pi/\Delta t$. Thus we can rewrite Eqn.(2.19) as

$$\hat{J}_s(s) = \int_{-\infty}^{+\infty} ds' \hat{C}'(s') \sum_{i=-\infty}^{+\infty} \delta(s' - (s - \frac{i2\pi}{\Delta t})) \quad (2.20)$$

where

$$\hat{C}'(s) = \int_{-\infty}^{+\infty} dt \exp(st) \left(\int_{-\infty}^{+\infty} dt' [E_{r0}^2(t') + E_{s0}^2(t') + 2E_{r0}(t' + \tau(t)) E_{s0}(t')] \right). \quad (2.21)$$

In Eqn.(2.21) the last term is proportional to $\hat{C}(s)$, the Fourier transform of the correlation function, $C(\tau(t))$ that we seek.

Including the effects of the detector and circuit, the voltage signal available at the computer input is

$$\hat{V}_s(s) = F_1(s) F_2(s) \hat{J}_s(s) \quad (2.22)$$

where $F_1(s)$ and $F_2(s)$ are the transform functions of the detector and the signal conditioning circuit:

$$F_1(s) = \frac{\eta e D}{h\nu T' \Delta t} \frac{1}{s + \frac{1}{T'}} \quad (2.23)$$

$$F_2(s) = \frac{1}{C} \frac{1}{s + \frac{1}{RC}}.$$

Because, as we already showed, the maximum frequency component in $\hat{C}'(s)$ is much less than the repetitive frequency of the laser pulses, $2\pi/\Delta t$, the cutoff frequencies of $F_1(s)$ and $F_2(s)$ now serve two functions. First, they must be low enough to cut out all but the lowest term in Eqn.(2.20), and second, they must be higher than the maximum frequency component in $\hat{C}'(s)$. When these conditions are satisfied $V_s(s)$ will be proportional to, $\hat{C}(s)$, the fourier transform of the desired

correlation function, plus a DC offset.

2.5 SAMPLE AND HOLD CONSIDERATIONS

The voltage signals described in the last two sections are digitally acquired by a computer board. In addition to the above considerations we must also consider the effects of sampling on the signals. According to the well-known Nyquist sampling theorem [Ref.29], in order to digitally store all of the information necessary to reconstruct the actual input signal with maximum frequency component ω_{\max} , it is required to have the sampling rate be at least twice ω_{\max} . In this system, the useful frequency range is from 0 to $\max\{\omega_{r\max}, \omega_{s\max}\}$. Typically the sampling rate is chosen $\approx 4 \times \max\{\omega_{r\max}, \omega_{s\max}\}$.

Until now we have not considered the effect of the integration process on the sampled signal $V_s(t)$. We know that the sampling consists of three processes: integration, hold and A/D conversion. The integration process will contribute to the sampled signal $V_s(s)$ by its transfer function. The transfer function for an integration process with time constant T_i has bandwidth of $2\pi/T_i$. In this system the bandwidth of the integration transfer function is larger than 10 MHz [Ref.35], which is much greater than $\max\{\omega_{r\max}, \omega_{s\max}\}$. Then the integration process transfers faithful information of the signal $V_s(t)$ in the frequency region we are interested in.

When the requirements above are met by careful design, the relationship between the reference signal measured, $V_r(t)$, and the relative path delay, $\tau(t)$, is described by Eqn.(2.10). Neglecting the effects of the energies of the reference and signal pulses, the signal measured in the signal generating interferometer, $V_s(t)$, is related to the correlation between the reference pulse field

and the signal pulse field as

$$V_s(t) = \alpha \int_{-\infty}^{+\infty} dt' E_r[t' + \tau(t)] E_s[t'] \quad (2.24)$$

or

$$V_s(t) = \beta \int_{-\infty}^{+\infty} dt' f_r[t' + \tau(t)] f_s[t'] \cos[\omega\tau(t) + \phi_s(t') - \phi_r(t' + \tau(t))] \quad (2.25)$$

The constants, α and β , are system related, and $E_r(t)$ and $E_s(t)$ are the fields of single reference and signal pulses, respectively.

2.6 SIGNAL PULSE RECOVERY

To conclude this chapter, we discuss one way to extract the amplitude and phase functions for the signal field from the measurement based on Eqn.(2.10), Eqn.(2.24) and Eqn. (2.25) above. Various means can be used to extract the phase information contained in the correlation signal $\propto C(\tau)$, assuming the reference field is well-characterized. The method of analyzing the fringe shifts on τ to identify instantaneous phase shifts was demonstrated by Kim, et. al. [Ref.3], and Chelma, et. al. [Ref. 4]. Various model-specific techniques for simulating $C(\tau)$ are also of course possible.

Here we describe a more general approach.

The sampled version of the correlation function, $V_s(t)$, as described in Sect.2.5, can be converted from real time space to relative path delay space, using the $\tau(t)$ obtained from decoding the reference channel signal as described in Sect.2.3. Assuming the scan amplitude is large enough to record the complete interferogram (ie. a factor of ~ 2 larger than the sum of the reference and signal pulse durations), the Fourier Transform of the correlation function, $\hat{C}(s)$, can be obtained with respect to τ , using software. We obtain

$$\hat{C}(s) = \gamma \hat{E}_r(s) \hat{E}_s(s) \quad (2.26)$$

where γ is a system related constant.

Now if $\hat{E}_r(s)$ is known, and is non-zero over the entire range of $\hat{C}(s)$, then the complex signal field $\hat{E}_s(s)$ can be recovered using

$$\hat{E}_s(s) = \frac{\hat{C}(s)}{\gamma \hat{E}_r(s)} \quad (2.27)$$

Thus in order to use this technique to unambiguously determine $\hat{E}_s(s)$ one would ideally use a transform-limited reference field with pulse duration short enough that the reference pulse bandwidth exceeds the signal pulse bandwidth. In practice the reliability of the technique will therefore depend on the quality of and the ability to characterize the reference pulses. These practical considerations are discussed further in later chapters.

Assuming \hat{E}_r is a symmetric transform-limited pulse, we have, switching from s to ω frequency arguments,

$$\hat{E}_r(\omega) = \hat{E}_r(-\omega) = \hat{E}_r^*(\omega). \quad (2.28)$$

In this case $\hat{E}_r(\omega)$ can be determined from the autocorrelation signal obtained by putting the reference pulses through both arms of the Mach-Zehnder interferometer. The Fourier Transform of the autocorrelation signal, $V_s(\tau)$ with respect to the relative path delay, τ , is

$$\hat{A}(\omega) = \sqrt{Y} \hat{E}_r^*(\omega) \hat{E}_r(\omega). \quad (2.29)$$

Thus

$$\hat{E}_r(\omega) = \frac{1}{\sqrt{Y}} \hat{A}^{\frac{1}{2}}(\omega). \quad (2.30)$$

Finally, this gives us an expression for the experimentally measured frequency spectrum of the signal pulse

$$\hat{E}_s(\omega) = \sqrt{Y} \frac{\hat{C}(\omega)}{\hat{A}^{\frac{1}{2}}(\omega)} \quad (2.31)$$

whose inverse Fourier Transform will give the signal pulse profile, including both its amplitude and phase information. Differences between the reference and signal fields reveal the influence of material interactions on the signal field, which can in general be time and frequency-dependent.

CHAPTER 3. SYSTEM DESIGN

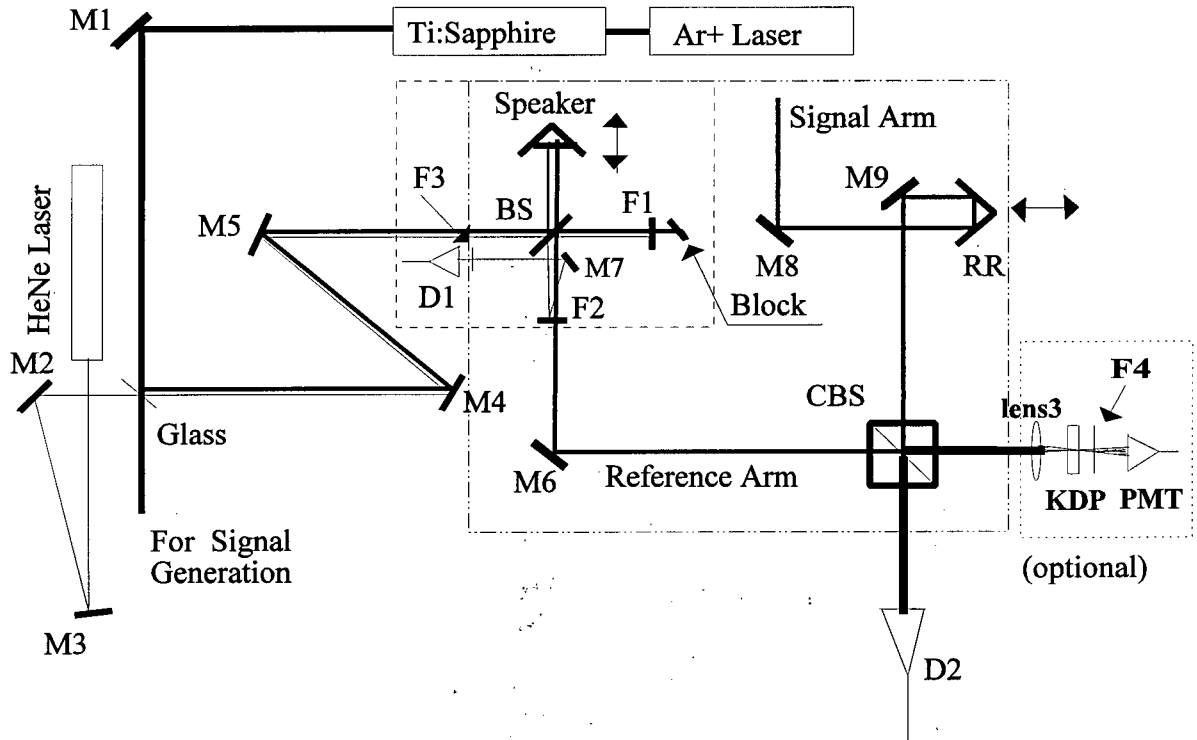
3.1 GENERAL DESCRIPTION

In this chapter we consider the design of the optical interferometric cross-correlator system. Fig.3.1 is the schematic diagram showing the optical interferometers and the optoelectronic detection parts of this system. The Michelson interferometer is used for relative path decoding, and the Mach-Zehnder interferometer is for homodyne detection of the signal pulses. A more complex configuration suitable for pump/probe interferometric measurements can be found in Appendix A.

A cw HeNe laser is used as a reference beam for decoding the true motion of the fast scanner. This beam goes through the alignment system consisting of reflections from mirrors M2 and M3, passage through the thin glass plate, and reflections from mirrors M4 and M5, which direct it into the Michelson interferometer.

Approximately 4% of the mode-locked pulse train from the Ar⁺ laser-pumped Ti:sapphire laser is reflected from the front surface of a glass plate and steered by mirrors M4 and M5 into the reference arm of the Mach-Zehnder interferometer. The signal beam, which could be derived from a separate experimental apparatus to which the remaining 92% of the mode-locked train is directed, enters the other arm of the interferometer via M8.

The outputs from the interferometers are detected by photodiode detectors D1 and D2. The electrical signals from D1 and D2 are filtered and sampled by a fast analog to digital converter board in an Intel 486 personal computer. The various sub-components of this system are described



The speaker is controlled by a computer, and the electronic signals from detectors, D1 and D2, are input to the computer.

Fig.3.1 System schematic for the optical interferometers and the optoelectronic detection. The components within the dashed box comprise the Michelson interferometer, those within the dashed-dotted box comprise the Mach-Zehnder interferometer, and those within the dotted box are for nonlinear interferometric detection.

in detail below.

3.2 INTERFEROMETERS

A modified Michelson interferometer is used for decoding the position of the scanned mirror. It consists of the beam splitter BS, the mobile mirror on the fast scanner, and a fixed dielectric mirror, F1. The output from the Michelson interferometer is directed by the dielectric mirror, F2, and mirror M7 to the detector, D1. To minimize any asymmetry in the Mach-Zehnder interferometer, F2 is the same type of mirror as F1, and is tilted at only a small angle of ~ 0.05 rads from the optical axis. The choice of F1 and F2 depends on the wavelength of the mode-locked reference beam. In its current configuration, the Ti:sapphire laser can be tuned from 730 nm to 850 nm. Dielectric coatings on both F1 and F2 reflect over 85% of the HeNe laser output (wavelength 632.8 nm) and pass over 85% of the mode-locked laser output. The filter, F3, is used to prevent residual reflections of the mode-locked laser output off F2 from entering the detector for reference decoding.

A modified Mach-Zehnder interferometer is used to generate the signal interferogram. It consists of the mirror mounted on the fast scanner, a beam splitter, BS, mirrors M6, M8 and M9, a retroreflector, RR, and a cubic beam splitter, CBS. The signal pulses are reflected by the retroreflector and M9, and then enter the cubic beam splitter. The retroreflector, RR, is used to manually compensate the relative path difference between the reference and signal beams. After the BS, the reference beam is overlapped with the signal beam on the CBS. There are two reasons why we use a cubic beam splitter at the output port of the Mach-Zehnder interferometer. First, it provides two outputs that can be used for independent processing. As shown in Fig.3.1, the setup in the

dotted box is for independent nonlinear interferometric measurement. Second, it minimizes asymmetries in the two arms.

Finally, we note that both interferometers share the beam splitter, BS, and the fast scanner. In both interferometers, the input light fields are reflected by the first surface of beam splitter BS to avoid asymmetry in the two arms due to the finite thickness of the beam splitter BS. The fast scanner used in this system consists of a mirror glued to the centre cone of a commercial audio speaker, an AVI Sound International Ltd. Model SL-300 woofer with an impedance of 4Ω and a resonant frequency of 30.9 Hz [Ref.30].

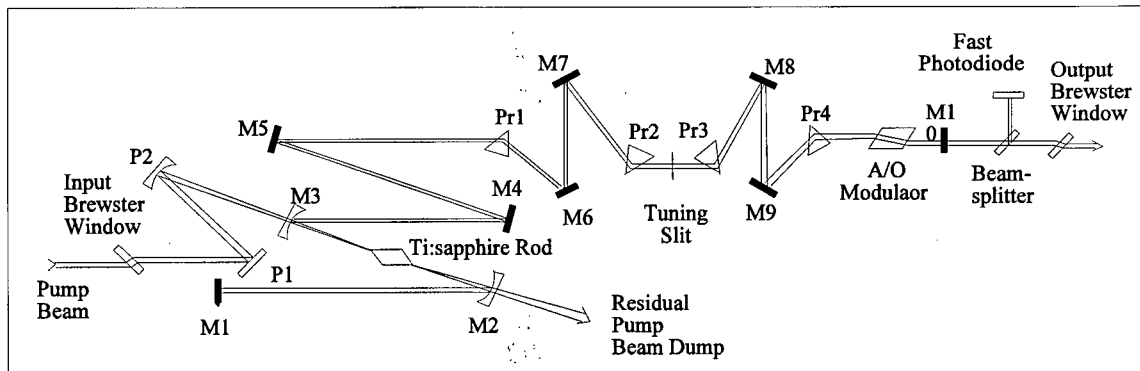


Fig. 3.2 Beam Path for fsec Tsunami Configuration.

3.3 LASER SYSTEM

The HeNe laser output must have a coherence length much longer than the maximum

excursion of the scanner, and it should have as little fluctuation in its intensity as possible. The laser used in the present setup has a coherence length of ~ 0.6 m and an intensity stability of $< 1\%$ [Ref.31].

The mode-locked Ti:sapphire solid state laser, Model 3960-S1S, is pumped by a Model BeamlokTM 2060 CW Ar⁺ laser, both of which are manufactured by Spectral-Physics Lasers Co.[Ref.34]. In pulsed-mode operation, it produces pulses of ~ 70 fs duration at a repetition rate of 82 Mhz. Its center wavelength is tunable from 730 nm to 850 nm, and the average output power can be up to 500 mW using a high quality 6 W TEM pump. Fig.3.2 shows the cavity configuration used to obtain this output performance. A slot mounted on a micrometer and inserted in the optical path between the prisms is used to tune the center wavelengths of the laser pulses. The characteristics of these pulses are discussed further in Chapter 4. The mechanism responsible for generating these short pulses is described in Ref. 34.

3.4 ELECTRONIC SIGNAL PROCESSING (HARDWARE)

The overall system is controlled by a 50 MHz Intel 486-based computer that has a multifunction input/output (I/O) board, AT-MIO-64F-5 from National Instruments [Ref.35], which interfaces with the experimental hardware. The following subsections discuss the various hardware components in Fig.3.3. A discussion of the synchronized pump beam chopper package is deferred to Appendix B.

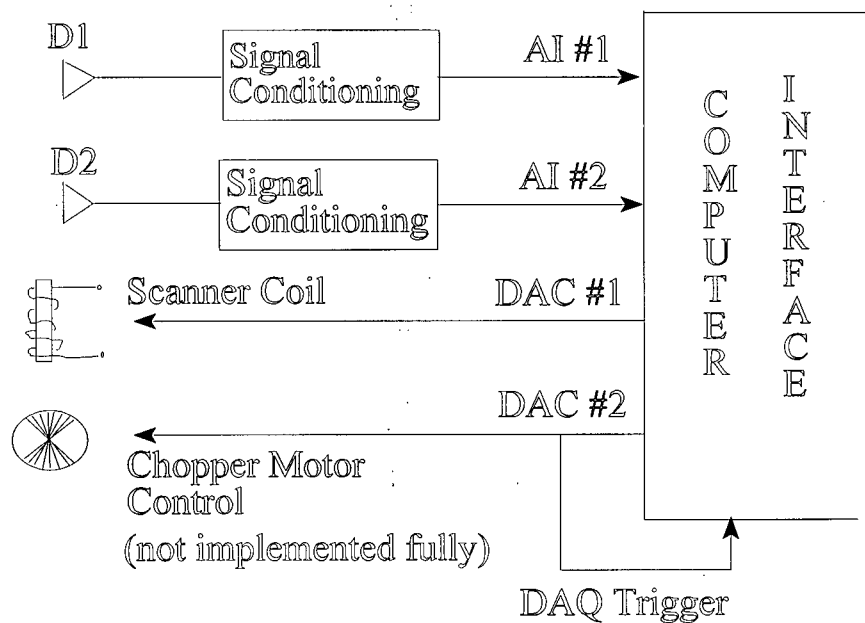


Fig.3.3 Schematic diagram of the interface. AI stands for analog input channel, DAC stands for data signal output channel and DAQ stands for data acquisition.

3.4.1 IMPEDANCE MATCHING

In Chapter 2, we derived the criteria that the detectors and matching circuitry must meet to ensure faithful recording of the signals needed for decoding the relative path delay and deducing the signal field amplitude and phase. Fig.3.4 shows the real time interferograms acquired from the two interferometers when the detectors are not matched to meet the criteria. Ideally the detector and matching circuitry transfer functions should be flat from DC to the maximum frequency components of the relevant interferograms, and they should rapidly decay to zero for higher frequencies.

The maximum frequency component in the decoding channel can be simply estimated by

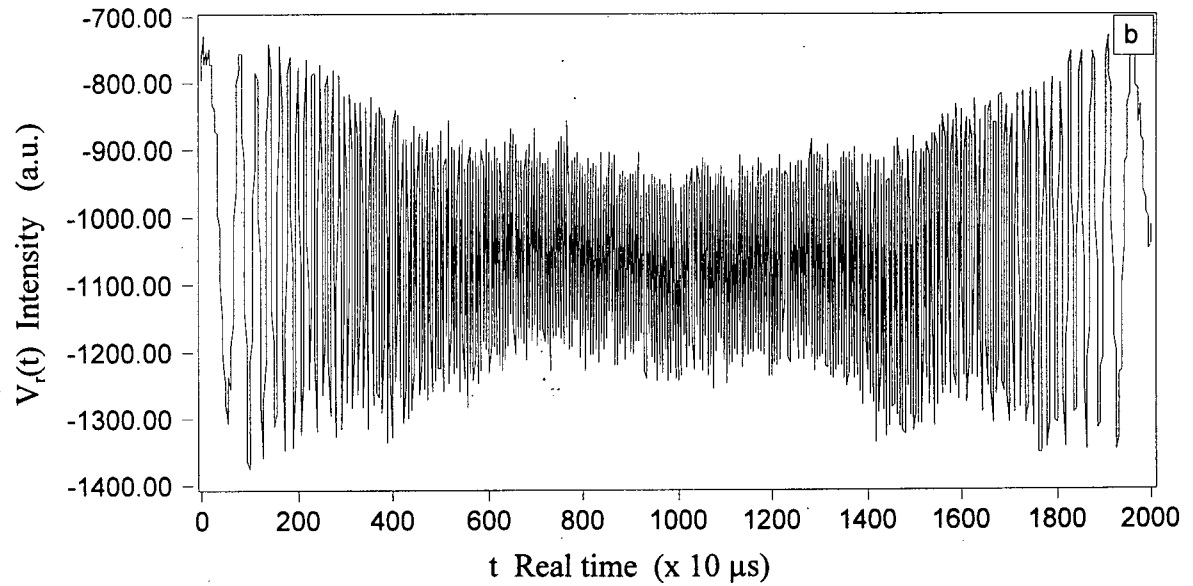
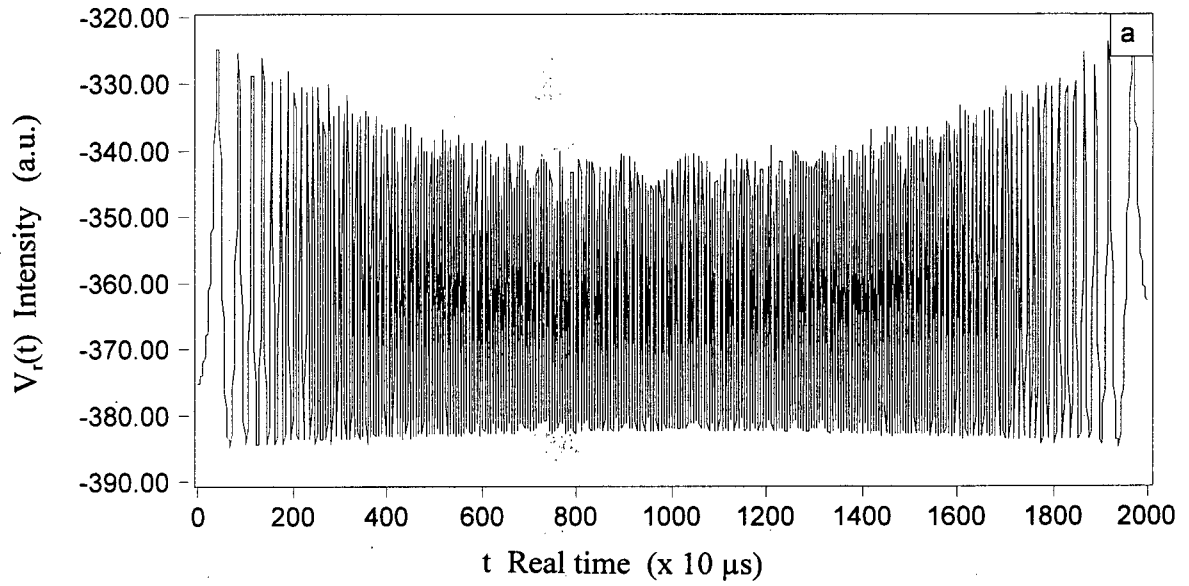


Fig.3.4 (a) The real time interferogram for the HeNe laser source, from D1, before impedance matching. (b) The real time interferogram for the cw Ti:sapphire laser source, from D2, before impedance matching.

expressing the relative path delay provided by the speaker as $\tau = \tau_{\max} \sin(\Omega t)$, where Ω is the driving angular frequency of the speaker. The highest real time frequency component in the decoding channel signal will therefore correspond to the rate that interference fringes are formed by the HeNe laser as one arm of the interferometer is moving at its maximum velocity. From Eqn.(2.16), this is just

$$v_{\max}^{\text{decode}} = \frac{c}{\lambda_{\text{HeNe}}} \Omega \tau_{\max} \quad (3.1)$$

where c is the light velocity in vacuum. A similar analysis for the signal channel yields essentially the same estimate with λ_{HeNe} replaced by λ_c , the center wavelength of the Ti:sapphire laser pulse. This center wavelength can be tuned, as we have said, but its lowest value is around 720 nm. Thus the highest real time frequency component is found in the signal from the decoding channel, and hence a limit on the amplitude and frequency that may be used in the scanner, and the maximum sampling rate of the computer board puts a limit on v_{\max} that can be decoded. The details are described below, but the maximum rate that each of the decoding and signal channels can be sampled is 100 kHz/channel. Therefore, by The Nyquist theorem, we must have $v_{\max} \leq 50$ kHz each, and we in fact keep $v_{\max} \leq 25$ kHz/channel. In practice, the high cutoff frequency of the matching circuitry is set 5 ~ 8 times larger than v_{\max} , or ~ 200 kHz.

Theoretically, we can find the corresponding impedance needed for the

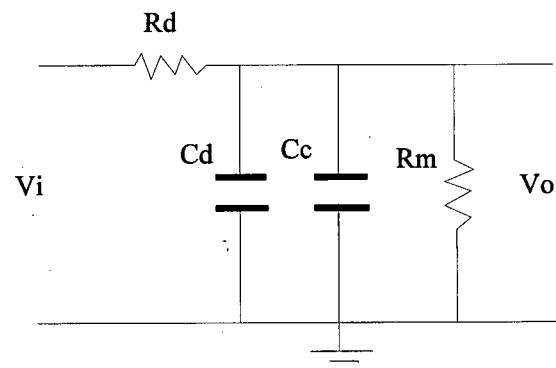


Fig.3.5 Electrical Circuit for Signal Channel with Impedance Matching.

matching circuitry. In this system, the detector for the decoding channel is unbiased, and that for the signal channel is biased. As an example, we present the analysis for the signal channel here. Fig. 3.5 is the equivalent circuit for the signal channel after impedance matching, where R_d is the output impedance of the detector, C_d its residual capacitance, C_c the capacitance of the transmission cables and R_m the matching impedance. The transfer function of this circuit to the input from the photodiode junction is:

$$G(\nu) = \frac{V_o}{V_i} = \frac{R_m}{(R_d + R_m) + j2\pi\nu R_d R_m (C_d + C_c)} \quad (3.2)$$

with half gain point

$$\nu \Big|_{\frac{1}{2}} = \frac{1}{2\pi} \frac{R_d + R_m}{R_m R_d (C_d + C_c)} \quad (3.3)$$

For the parameters of the photodiode used as the detector for the signal channel, a Model 818-BB-21 battery biased silicon PIN detector from Newport Co. [Ref.33], we have: $R_d = 50 \Omega$, $C_d = 0.1 \text{ pF}$, and $C_c = 0.2 \text{ pF}$ for 6 ft cable. To enable the detector matching circuitry have the high cutoff frequency of 200 kHz, we find $R_m = 22 \text{ k}\Omega$ is the required matching impedance.

Figs. 3.6 (a) and (b) show the experimentally measured frequency responses for different matching impedances, and Figs. 3.7 (a) and (b) show their gains at 20 kHz. These characteristics were determined by the following method. Taking the signal generated by cw HeNe laser source from the Michelson interferometer as a fixed input to the signal conditioning circuits, for each matching impedance, we acquired an interferogram, and then the amplitude for each fringe

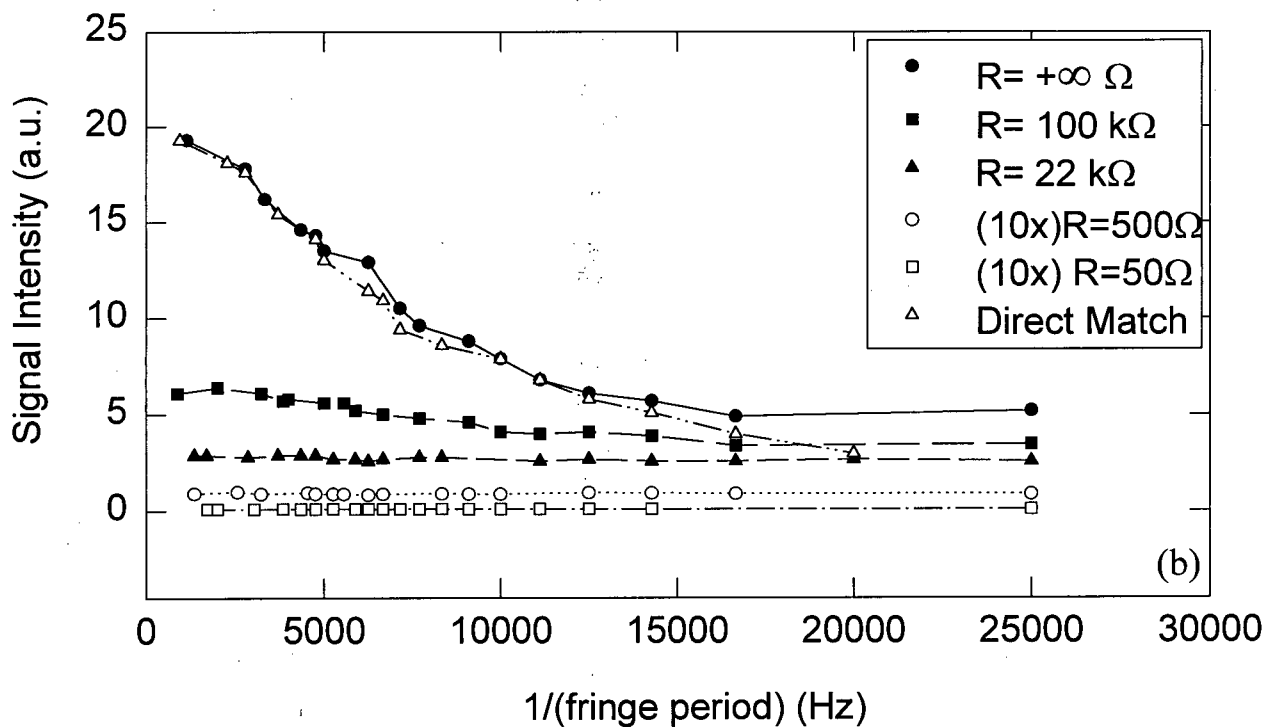
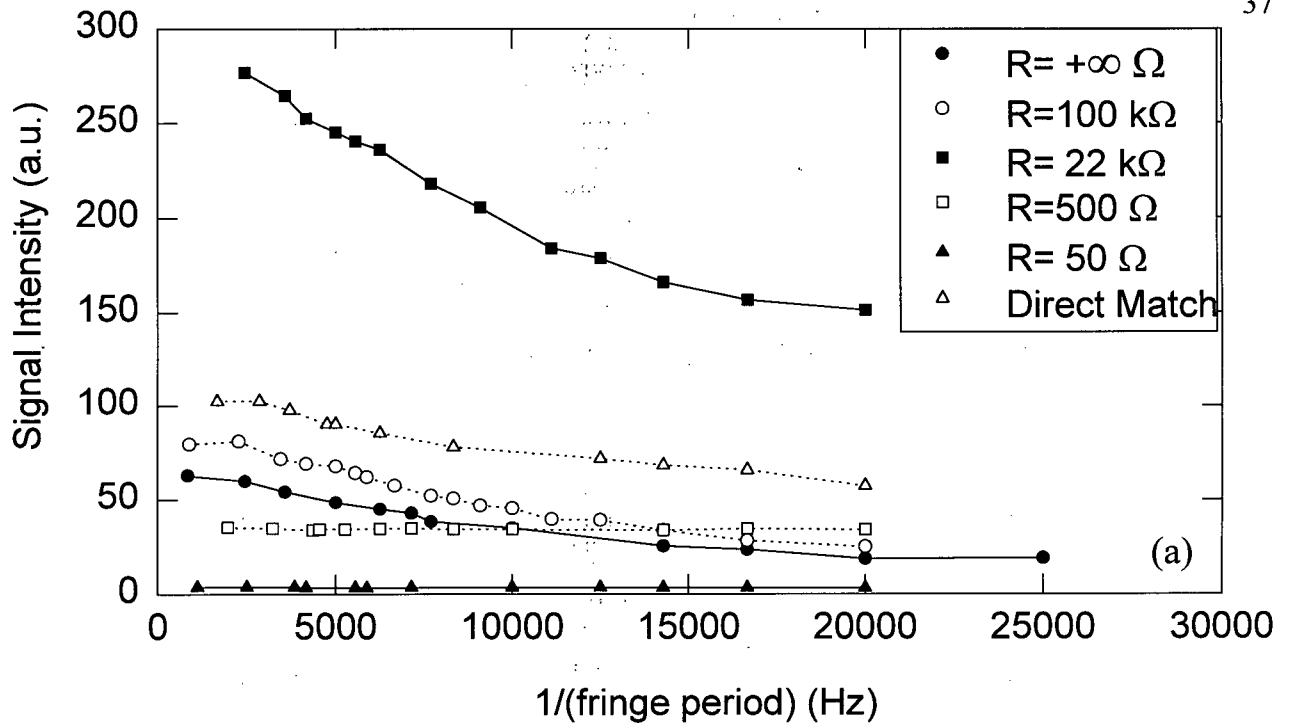


Fig.3.6 (a) The frequency response of the signal conditioning for the decoding channel at different matching impedences for a fixed input from the Michelson interferometer. (b) The frequency response of the signal conditioning for signal channel at different matching impedences for a fixed input from the Michelson interferometer.

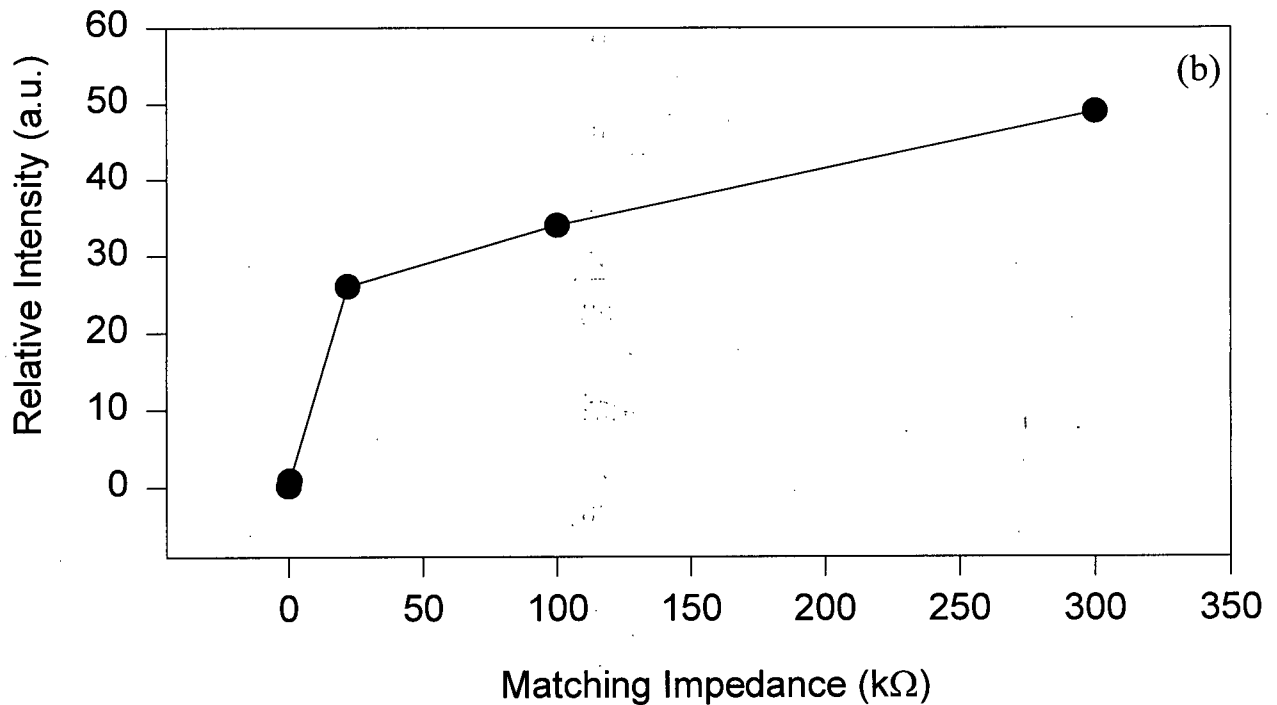
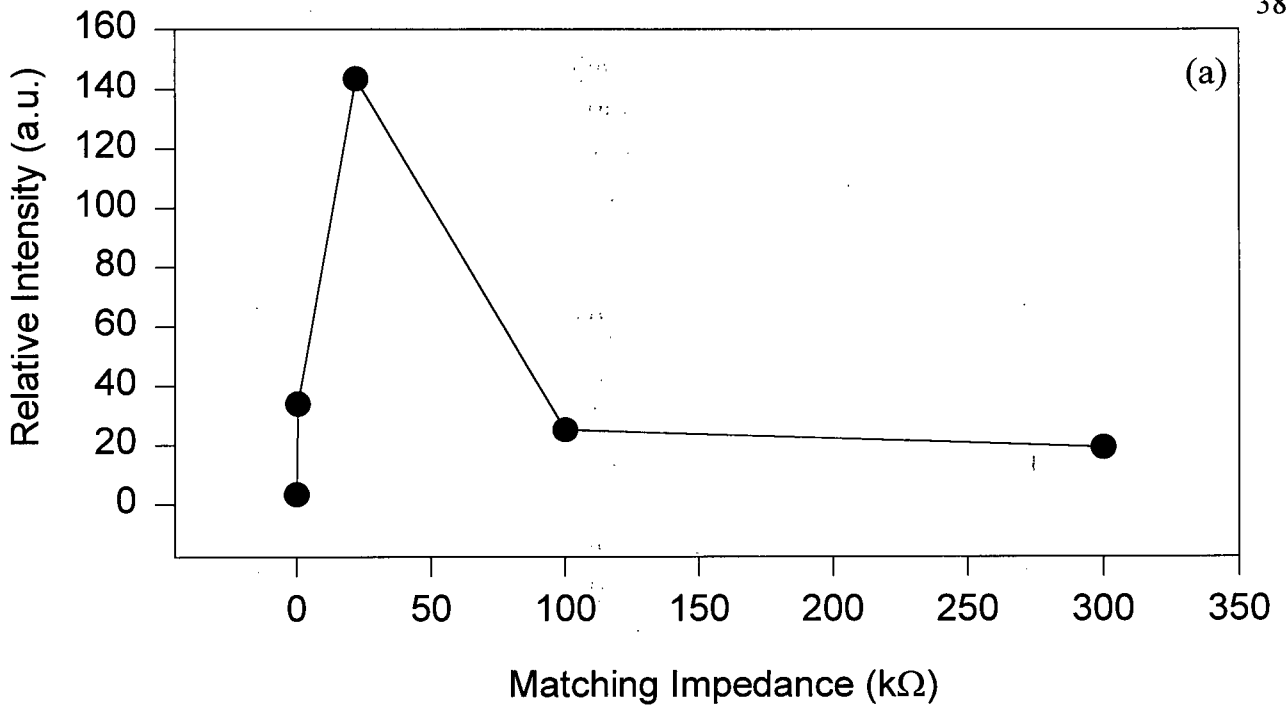


Fig.3.7 (a) The relative signal amplitude at the output of the matching circuit of the decoding channel for fixed input from the Michelson interferometer, at the frequency of 20 kHz, for different matching impedances. (b) The relative signal amplitude at the output of the matching circuit of the signal channel for fixed input from the Michelson interferometer, at the frequency of 20 kHz, for different matching impedances.

period is measured, the inverse of which is taken as the a frequency on the graphs. We can see that the frequency responses are optimum, with a matching impedance of $R_m=22\text{ k}\Omega$ for the signal channel and $R_m=500\ \Omega$ for the decoding channel. For a flat frequency response, the trade off is that the gain is reduced.

3.4.2 COMPUTER INTERFACE BOARD

The computer ADC board is an AT-MIO-64F-5 multifunction I/O board for PC AT/EISA manufactured by National Instruments Co.[Ref.35]. This board is a high-performance multifunction analog, digital, and timing I/O board. It has a 4.6 μsec and 12-bit sampling ADC, which can monitor a single input channel or scan through 64 single-ended (32 differential channels) at programmable gain of 0.5, 1, 2, 5, 10, 20, 50, or 100, for unipolar or bipolar input ranges. A 12-word ADC FIFO buffer can perform seamless data acquisition at the maximum rate without data loss. Internal or external triggerings are supported.

This board also has two double-buffered multiplying 12-bit DACs that may be configured as a unipolar or bipolar voltage output range. An on-board +10 V reference is the internal reference to the circuitry of the DAC. A 2,048-word DAC FIFO buffer allows seamless waveform generation at the maximum rate without data loss. The DAC FIFO can perform cyclic waveform generation directly from the FIFO, independent of the PC interface.

In the present system, the two analog output channels are used to drive the fast scanner, and to trigger the data acquisition. The triggering signal can also be converted to drive the synchronized motor mounted with an optical chopper for use in pump/probe interferometric measurements, as described in Appendix B. The analog input channels are used to acquire the electronic signals from

the two photodetectors. The board is operated at the maximum data acquisition rate of 200 K samples per second, 100 K per channel, to maximize the useable delay range.

3.4.3 DIFFERENTIAL INPUT PACKAGE

For the signal and decoding interferogram acquisitions, we use the differential input configuration. The performance of this system can benefit from this configuration in two aspects. By putting the raw signal into one input and a low-pass filtered and amplified version of the same raw signal into its matched input, the useless DC components, and low-frequency noise components can be removed from the raw signal. In the case where the amplitude of the signal beam is much lower than that of the reference beam, this approach has the added advantage of allowing the

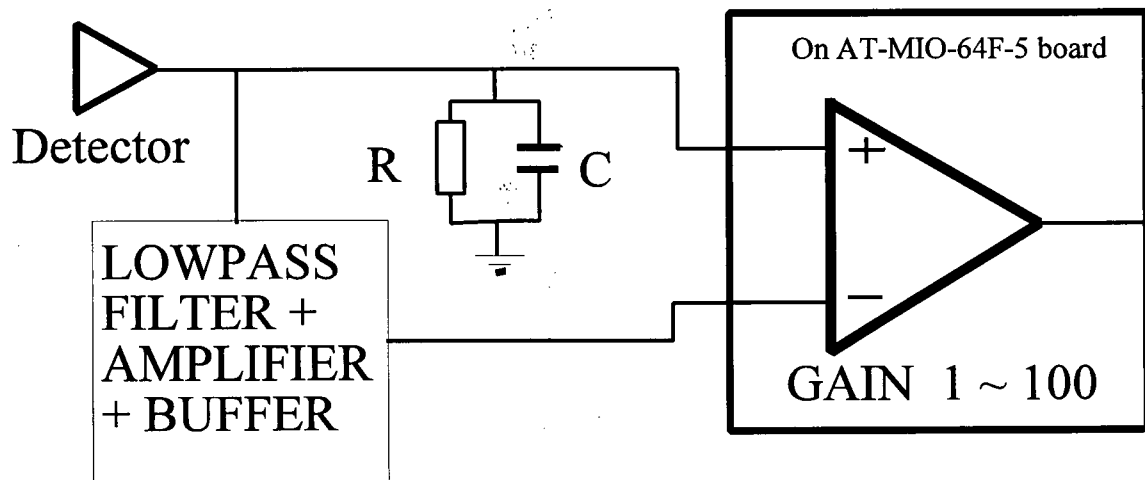


Fig.3.8 Differential Input Configuration

programmable gain of the AT-MIO-64F-5 board to be used to boost the relevant parts of the signals.

Fig.3.8 shows the schematic diagram used for the differential input package. The electronic signal from the detector is split electronically into two branches. One is input directly to the positive input end of the differential amplifier on the board. The other goes through an electronic processing package, then is input to the negative input end of the differential amplifier. This electronic processing package includes a low-pass filter, an amplifier and a current buffer. The low-pass filter is designed to have a high cutoff frequency at 120 Hz.

3.5 ELECTRONIC SIGNAL PROCESSING AND ANALYSIS (SOFTWARE)

The whole software package for data acquisition, device drivers, and signal processing and analysis is written using Labview for Windows™ provided by National Instrumentation Inc. In this section, we give a brief introduction to this graphical programming tool and generally describe the virtual instruments (VIs) we developed for the device drivers, the decoding channel and the signal channel data processing and analysis.

3.5.1 INTRODUCTION TO LABVIEW™

Labview™ is a program development tool that uses a graphical programming language, G, to create programs in block diagram form. The difference between Labview™ and conventional program developing packages like C or Basic is analogous to that between individual electronic devices and integrated circuits (IC).

Like C or Basic, Labview™ is a general-purpose programming system with extensive libraries of functions and subroutines for many programming tasks. It also contains application-

specific libraries for data acquisition, GPIB and serial instrument control, data analysis, data presentation, and data storage. It also includes conventional program development tools, so users can set breakpoints, animate the execution to see how data passes through the program, and single-step through the program to make debugging and program development easier.

Labview™ programs are called virtual instruments (VIs) because their appearance and operation imitates actual instruments. However, they are identical to functions from conventional language programming. Applications are divided into a series of tasks and subtasks. Programming consists of building VIs to accomplish each subtask and then combining these VIs to accomplish the larger task. Finally, the top-level VI, which accomplishes the larger task, contains a collection of sub VIs, which accomplish subtasks comprising the larger task. Every VI has an interactive user interface, called a front panel; because it simulates the panel of a physical instrument. The front panel can contain knobs, push buttons, graphs, and other controls and indicators. Each VI receives instructions from a block diagram, which is a pictorial solution to a programming problem constructed in the C language. The icon and connector of a VI work like a graphical parameter list so that other VIs can pass data to a sub VI.

3.5.2 INTRODUCTION TO THE SOFTWARE PACKAGE

Fig.3.9 is the flow diagram for the software package developed to control and interface with the interferometers. This package consists of a device driver, a data acquisition VI, DAQ,

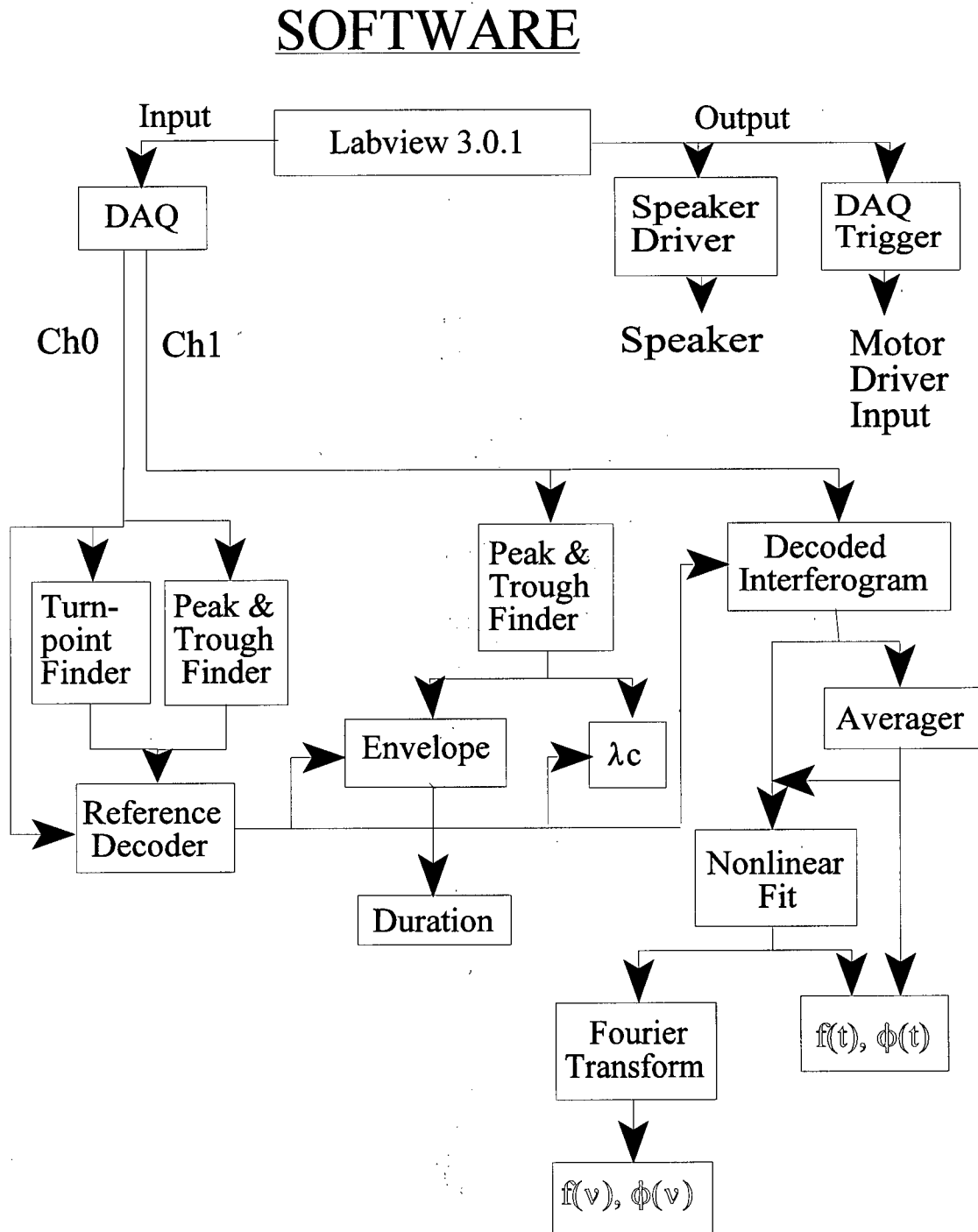


Fig.3.9 Flow Diagram For the Software Package

and the VIs for relative path delay decoding and signal processing.

The device driver generates appropriate waveforms to drive the speaker, and to trigger the data acquisition (this trigger may also be used to drive the pump beam chopper as described in Appendix B.). The data acquisition VI, DAQ, controls the sample-and-hold amplifier, the A/D converter and the buffer on the computer board. It acquires data from two channels: the decoding channel (ch0) from detector, D1, and signal channel (ch1) from detector, D2, in Fig.3.1. The data acquired from ch0 is processed by the turnpoint finder, the peak & trough finder, and reference decoder to decode the relative path delay. The data acquired from ch1 is the signal interferogram in real time space. With the output from the relative path delay decoding, it can be transformed to relative path delay space. After processing by the peak & trough finder, the duration finder, and the wavelength finder, this transformed data can be used to extract the duration of the input pulse and its center wavelength when the interferometer is used as an autocorrelator. In the case of cross correlations, the general ch1 interferogram can be processed by the averager VI to reduce the random noise, and the averaged interferogram can be processed by the nonlinear fit VI to extract the amplitude and phase information. The fitted result can be Fourier transformed to recover the signal pulse as discussed in Sect.2.6.

Detailed descriptions for each VI in this package can be found by running the enclosed floppy disk in Labview™.

3.5.3 DEVICE DRIVER

The filename for the device driver VI is **Generate Sig. & Sync.vi**. It generates sine and square waveforms for the two output channels (ch0 and ch1 in this VI), DAC#1 and DAC#2, on the

computer board, respectively. The sine signal output from the DAC#1 is used directly to drive the audio speaker that forms the heart of the fast scanner. The square wave signal is split into two branches. One branch is routed back into the computer board to trigger the analog input data acquisition (DAQ) for the input channels, and the other one is input to the synchronized pump beam chopper package, described in Appendix B, to synchronously drive the pump beam chopper after appropriate signal conditioning. The top level VI consists of hardware configuration VIs, data update control VIs, and waveform generation VIs, etc. as shown in Fig.3.10. In the panel of this top VI as shown in Fig.3.11, different waveforms can be selected from a choice of Sine wave, Square wave, and Triangle wave for different channels. The amplitudes and frequencies of the two output channels can be varied independently, and also their relative phase can be controlled.

The default parameters for this VI are set to be $\Omega_0=2\pi \times 25$ Hz for the frequency of ch0, $\Omega_1=2\pi \times 50$ Hz for the frequency of ch1, $\phi=0$ for the phase difference, $A_0=0.065$ V for the amplitude of ch0, and $A_1=5$ V for the amplitude of ch1. When changing the amplitude and frequency for ch0, one must recall that the relative path delay scan range is approximately proportional to the amplitude of ch0, $\tau_{\max} \propto A_0$. Also for faithful information extraction from the interferogram, the Nyquist frequency, i.e. half of the sampling rate f , should be larger than the highest frequency component: $f/2 > (c/\lambda_{\text{HeNe}}) \tau_{\max} \Omega_0$. Thus, in order to have a large enough sampling frequency for the decoding, A_0 and Ω_0 must be chosen so that

$$\frac{A_0 \Omega_0 \lambda_{\text{HeNe}}}{f} \leq 3.2 \text{ (V/m)}. \quad (3.4)$$

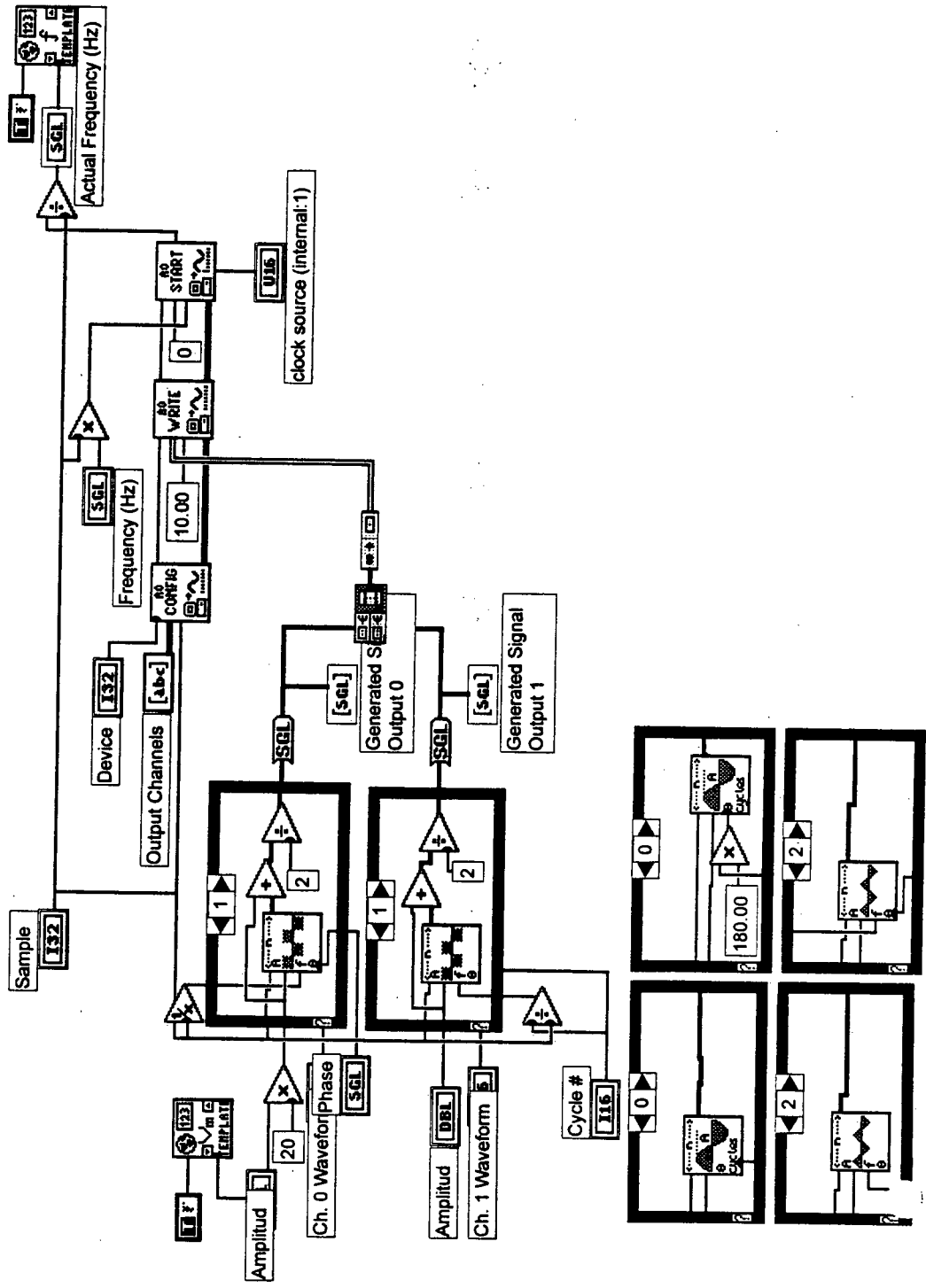


Fig.3.10 The block diagram for Generate Sig. & Sync.vi

Front Panel

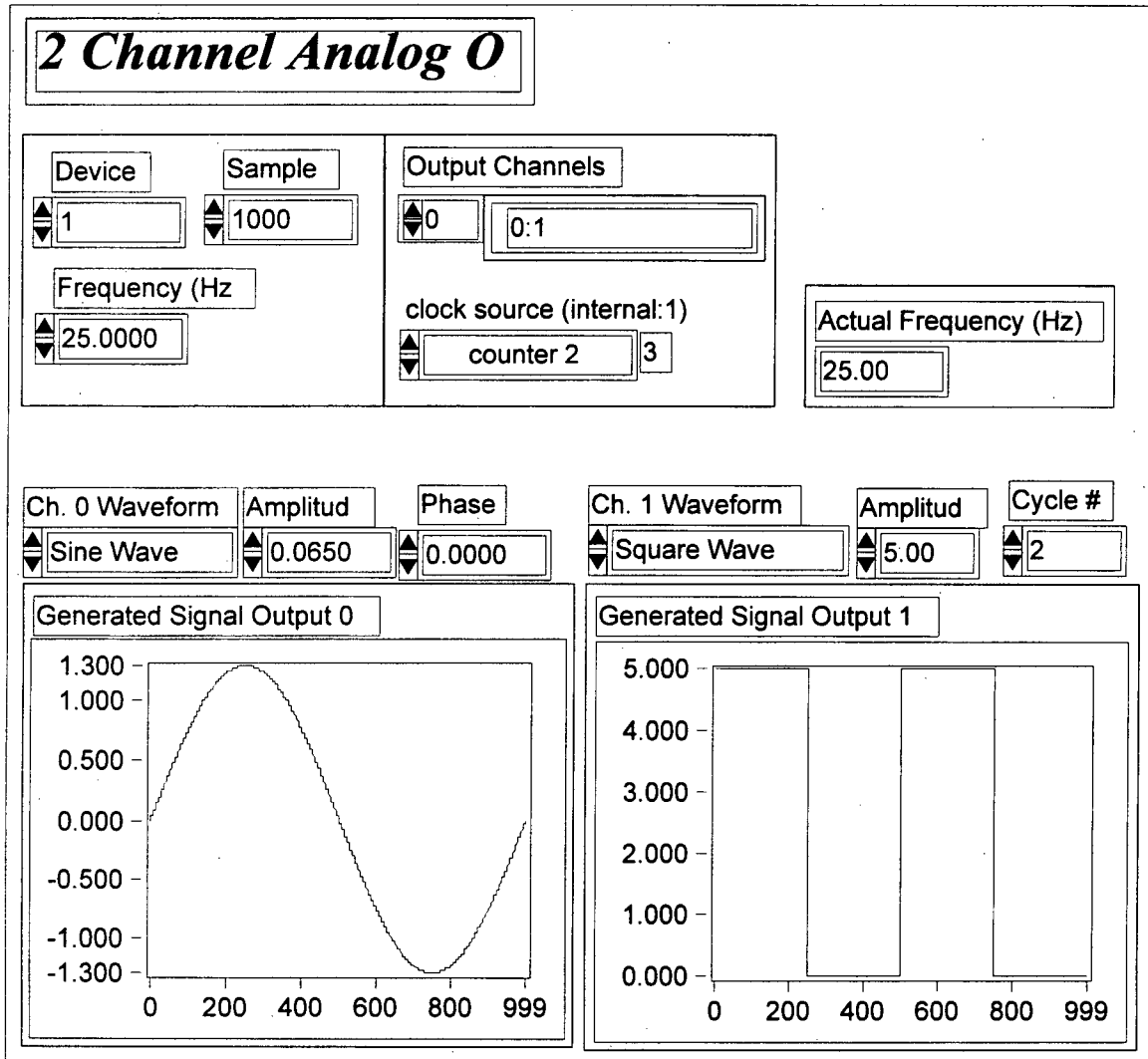


Fig.3.11 The panel for Generate Sig. & Sync.vi

3.5.4 DAQ VIS

Each top VI in this package consists of data acquisition sub VIs, data processing sub VIs and data analysis sub VIs for both the reference channel and the signal channel. They are **Acq & Proc (only single CH).vi**, **Acq & Proc (only two channels).vi**, **Acq & Proc (reference channel).vi**, and **Acq & Proc (Two channels).vi** respectively. They all acquire data from the computer board. **Acq & Proc (only single CH).vi** and **Acq & Proc (reference).vi** are used to observe the interferogram from only one channel, **Acq & Proc (reference).vi** is used only for finding proper input parameters for relative path delay decoding as we will describe in next section. **Acq & proc (only two channels).vi** is used to acquire signal data from only decoding channel and signal channel and to process and analyze these data. **Acq & Proc (Two channels).vi** can be used to acquire signal data from any two channels and to process and analyze them. The user can set them to acquire signal data, then store these data either before data processing or after data processing, depending on the size of the data set and the memory size of the computer.

Other top VIs were developed to acquire signal data from data files stored on disk. They are useful for some situations, such as when the data set is too big to be acquired and processed at the same time, or when we just want to acquire signal data and to process them afterward to save time. They are **Proc & Analysis (Two channels).vi**, **Proc & Analysis (only two channels).vi**, **Read & Proc (stream).vi**, and **Read & Proc (Datalog).vi**, and differ in the format of the data they read: **Read & Proc (stream).vi** is used for data files stored in stream format, **Read & Proc (Datalog).vi** is used for data files stored in datalog format, and the others are used for data files stored in text format.

Another VI, **Acq for Pump-probe.vi**, was developed for acquiring, processing and analyzing signal data in a conventional pump-probe configuration. It is described in Appendix A.

3.5.5 VIs FOR THE DECODING CHANNEL

The decoding channel has its own independent data processing VIs, which includes **Turnpoint.vi**, **Peak & Trough Finder.vi** and **Reference Decoder.vi** and their subVIs. All of these VIs are for relative path delay decoding as mentioned in Chapter 2. In this system, we use the reference interferogram sampled in real time space to decode the true motion of the fast scanner. This provides the signal channel the corresponding relative path delay generated by the scanning mirror at each sampling point in real time space. For each scan cycle of the fast scanner in real time space, the distance between a peak to an adjacent trough in the reference interferogram represents a $\lambda_{\text{HeNe}}/2$ position shift of the mirror on the fast scanner. Similarly, that from the trough to the next peak represents another $\lambda_{\text{HeNe}}/2$ position shift of the mirror. So by finding the sampling points corresponding to the peaks and troughs in the real time interferogram and then decoding the position shifts of the mirror relative to these peaks and troughs for every sampling point using Eqn.(2.10), we determine the exact relative positions of the mirror for all sampling points in a single scan. As demonstrated below, one of the advantages of using a fast scanner is that several concurrent scan cycles can be acquired in a very short time. This can minimize the effects of low frequency noise. All cycles in relative path delay space must have the same reference position to make sure we only average the data points at the same position in relative path delay space.

To take full advantage of this capability, the exact position of the speaker must be determined for the entire multi-cycle data stream, which requires registration from one cycle to the next. This

in turn requires that the turning point (zero velocity position in the speaker's motion) between half cycles in different direction be determined in software. The drawback of the speaker-based fast scanner used in the present system is its sensitivity to acoustic noise: it essentially acts as a microphone. Fig.3.12 is a reference interferogram in real time space, which corresponds to 2 scan cycles of the fast scanner in relative path delay space, and corresponds to 1 cycle of the fast scanner in real time space. Various turning points have different shapes, which reflects the fact that the extremity of the speaker travel varies by a fraction of a wavelength from cycle to cycle (the microphone effect). So long as the turning points are accurately identified in software, this slightly non-periodic motion of the speaker does not present a fundamental obstacle because the (known) position at the last fringe before the turning point can be directly associated with the position at the first fringe following the turning point, using symmetry. The procedure for doing this in software consists of finding all turning points in the sampled data set first, then finding the peak (trough) nearest to each turning point, and dumping all of the (irrelevant) data points between this peak (trough) in one scan cycle and the corresponding peak (trough) in the next scan cycle. Finally the data set left will be well decoded.

The algorithm for accomplishing this task is implemented in **Turn Point Finder.vi**. The input to this VI is the real time decoding interferogram, and it outputs the turning points of the scanner in real time space. The principle to find the turning points in the acquired reference channel data set is based on the inversion symmetry property of the decoding interferogram about the turning point. Properly choosing a window in the scan cycle right ahead of the turning point and choosing another window with the same width in the scan cycle right after the turning point, fixing the distance between both windows, and shifting both windows together in either direction, we always can find a position at which the data point distribution in one window is symmetric or correlates with

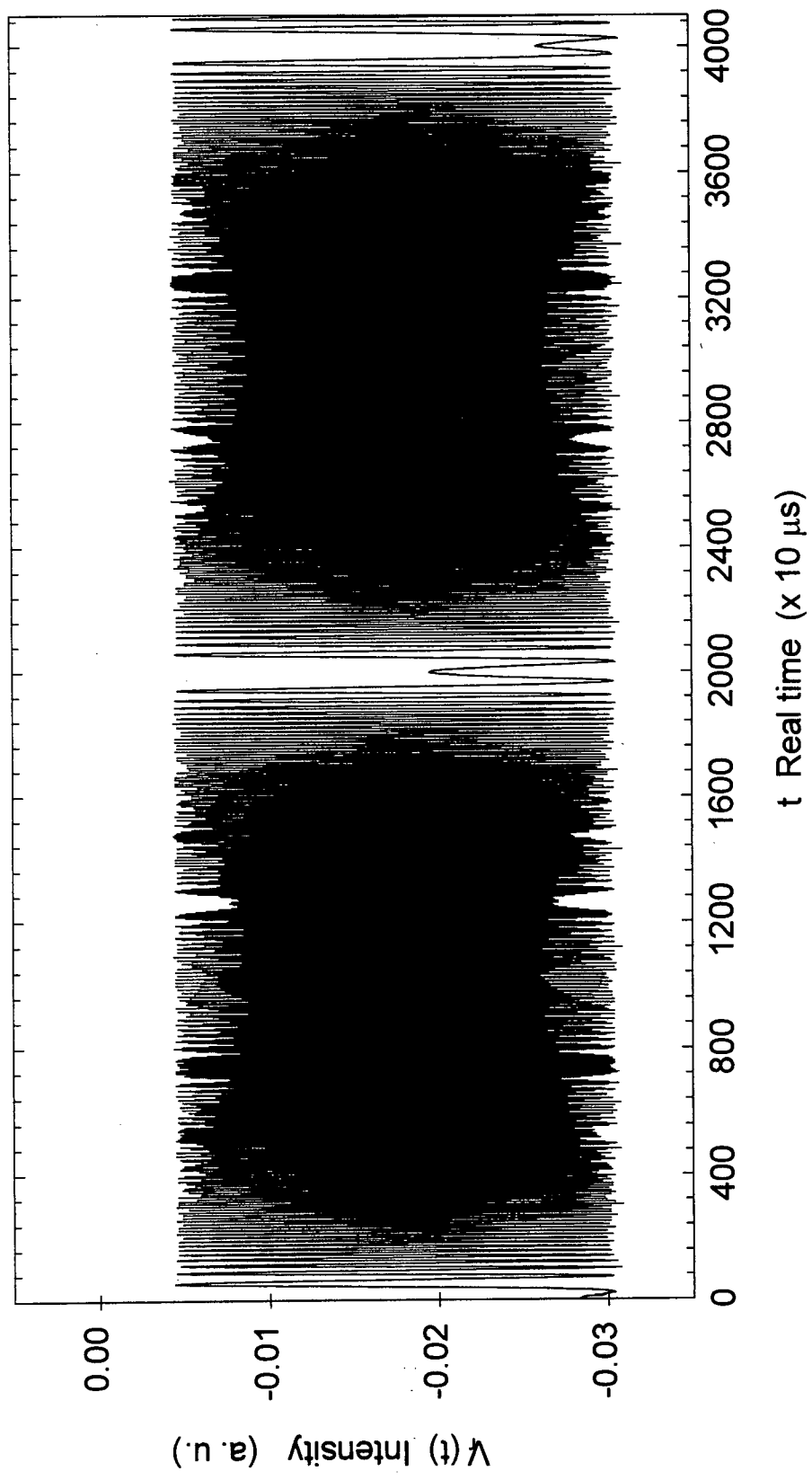


Fig.3.12 Two scan cycles of the real time interferogram from Ch0 corresponding to one round trip of the scanner.

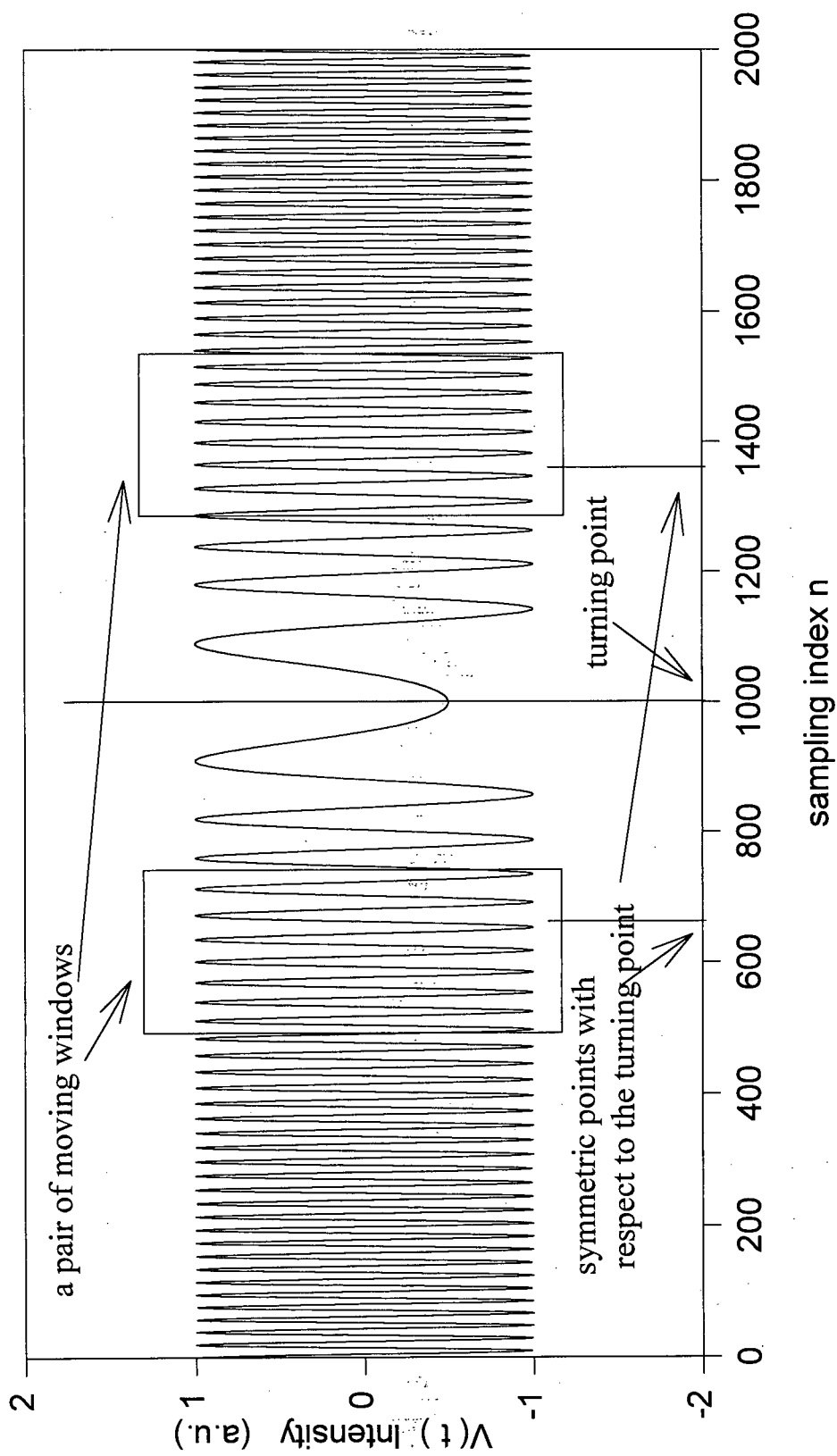


Fig.3.13 The schematic diagram showing the moving windows on both sides of a turning point.

that in the other window, then the center point between both windows is about the turning point position in real time space, as shown in Fig.3.13. The window width, the distance between both windows and the cutoff data number, which is the data number dumped to get rid of the effects of the unrepeatability of the motion of the fast scanner, in the panel of **Turn Point Finder.vi** should be chosen properly from experimental observation. After the **Turn Point Finder.vi**, the peaks and troughs are found by the VI: **Peak & Trough Finder.vi**. The inputs to this VI are the real time decoding interferogram and the output from the turning point finding VI: **Turnpoint.vi**, and it outputs the sampling positions of the peaks and troughs in the input data set in real time sampling space. The determination of the peak and trough positions is based on real time derivatives and the signal strengths relative to the background level.

Finally, the real time decoding interferogram, and the outputs from **Turnpoint.vi** and **Peak & Trough Finder.vi** are input to the decoding VI, **Reference Decoder.vi**, to decode the relative path delay for all sampling points, using Eqn.(2.10). Finally this transformation from real time space to relative path delay space is output to the signal channel to convert the signal interferogram from real time space to relative path delay space. In the **Reference Decoder.vi**, the **SUB Reference Decoder.vi** is used to decode the relative path delays for real time sampling points between peaks and their next troughs based on Eqn.(2.10).

3.5.6 VIs FOR THE SIGNAL CHANNEL

Along with the top VIs shared with the reference channel, the signal channel has its own sub VIs for data processing, analysis and display. They are **Decoder for 2nd Channel.vi**, **Real Time to Delay Convertor.vi**, **Interpolator.vi**, **Signal Peak & Trough Finder.vi**, sub **Peak & Trough**

Finder.vi, Data Sorter & Selector.vi, Data Averager.vi, Envelope & Its Duration.vi, Pulse Duration Finder.vi, Signal Averager (envelope).vi, Nonlinear Fitting.vi, Amp & Phase.vi and FFT.vi.

Real Time to Delay Convertor.vi and **Interpolator.vi** are the sub VIs of the VI, **Decoder for the 2nd Channel.vi**, whose input is the output from the **Reference Decoder.vi**. Due to the alternate sampling of the two channels by the computer, the samples for the signal channel are interleaved with those in the decoding channel, in real time space. Thus the relative path delay output from the **Reference Decoder.vi** must be used to interpolate to provide the relative path delay for every sampling point in the signal interferogram.

For characterization of input pulses obtained by running in autocorrelation mode with $E_r(t)$ in each arm of the signal generating interferometer, the **Signal Peak & Trough Finder.vi** and its sub V, **sub Peak & Trough Finder.vi**, locate the peaks and troughs in their inputs, the real time signal interferogram, and provide inputs for **Envelope & Its Duration.vi**. The algorithm here is the same as that in the **Peak & Trough Finder.vi** of decoding channel. The inputs to **Envelope & Its Duration.vi** are the output from the **Decoder for the 2nd Channel.vi** and that from the **Peak & Trough Finder.vi**. It is used to output the envelope of the interferogram in real time space or in relative path delay space, and it also outputs the duration of input pulse, which is based on the sech^2 shape model, the detail of which will give in Chapter 4.

Another VI, **Wavelength Finder.vi**, is used to find the center wavelength of the input pulse: as we know, if there are n peaks and m troughs in the interferogram, and the first peak is located at d_0 in relative path delay space and the last peak is located at d_f , then an estimation of the center wavelength λ_c of the input pulse is provided by

$$\lambda_c = \frac{2(d_f - d_0)}{(n + m)} \quad (3.5)$$

This can therefore be obtained from the outputs of the **Peak & Trough Finder.vi** and the **Decoder for the 2nd Channel.vi**.

The advanced data processing VIs in this package are used for noise reduction, numerical simulation to give the amplitude and phase information in relative path delay space, and Fourier Transformation of the signal interferogram to recover the signal pulse. **Data Averager.vi** is used to average more than one scan cycle interferogram into only one cycle interferogram. It has a sub VI: **Data Sorter and Selector.vi**. The procedure of this VI is that first it sorts the input multicycle interferogram in relative path delay space according to the value of the relative path delay in every pair of relative path delay and interferogram intensity, then divides the relative path delay scan range into small sections with controllable width, and finally averages the intensity data of all pairs in each small section to form a single pair in the final single cycle interferogram. **Nonlinear Fitting.vi** is the top VI of **Target Func.vi**, they are used to simulate the interferogram in relative path delay space using the models set in **Target Func.vi**, which can ultimately provide information about the ultrafast processes occurring in the studied system in time domain. The inputs to this VI are the interferogram in relative path delay space, estimated fit parameters, and the model function input to **Target Func.vi**. **FT.vi** is a VI to generate the Fourier Transform of the simulated interferogram in relative path delay space from the **Nonlinear Fitting.vi**. In this procedure, before numerical calculation of the FFT we extend the interferogram data set by adding data points at the background signal level to smooth the Fourier Transform [Ref.38]. It has applications in the measurement of the power spectrum and the recovery of the signal pulse profile as we discussed in Chapter 2.

The rest of the package includes VIs for data communications between VIs and devices. They include VIs for writing data to disk and reading data from disk, and global parameter VIs to communicate data from one VI to another VI.

CHAPTER 4. SYSTEM PERFORMANCE

This chapter presents performance test results of the interferometric cross correlation system.

Precise determination of the relative path delay is a key factor in this system, and hence the performance of this sub component is discussed first. The use of the system to characterize the femtosecond pulses is then discussed, and the results are compared to power spectral measurements of the same pulses obtained using a commercial interferometric spectrometer.

Finally, the results of cross correlating the reference pulses with reference pulses that pass through 4 and 8 mm pieces of quartz glass are presented.

4.1 DETERMINATION OF RELATIVE PATH DELAY

In Chapter 2, the method used for relative path delay decoding was described. In this section, the results obtained by implementing that method are presented. Fig.4.1 (a) shows a typical single cycle interferogram from the decoding channel in real time space. It is clear that the fringe spacing is not uniform in real time due to the nonlinear motion of the speaker. In the center part, which we refer as the high frequency region, corresponding to the maximum speaker velocity, the fringe density is much higher than that near the turning points of the speaker motion, which we refer as the low frequency region. Fig.4.1 (b) is the decoded relative path delay in real time space, which is approximately a sinusoidal function of real time. Ideally, the motion of the speaker would be perfectly periodic in which case the decoding could be done just once, and all interferograms from different cycles could be co-added as they are acquired. However, as Fig.4.2 illustrates, the speaker motion occasionally varies up to a few optical wavelengths from cycle to cycle, hence the decoding

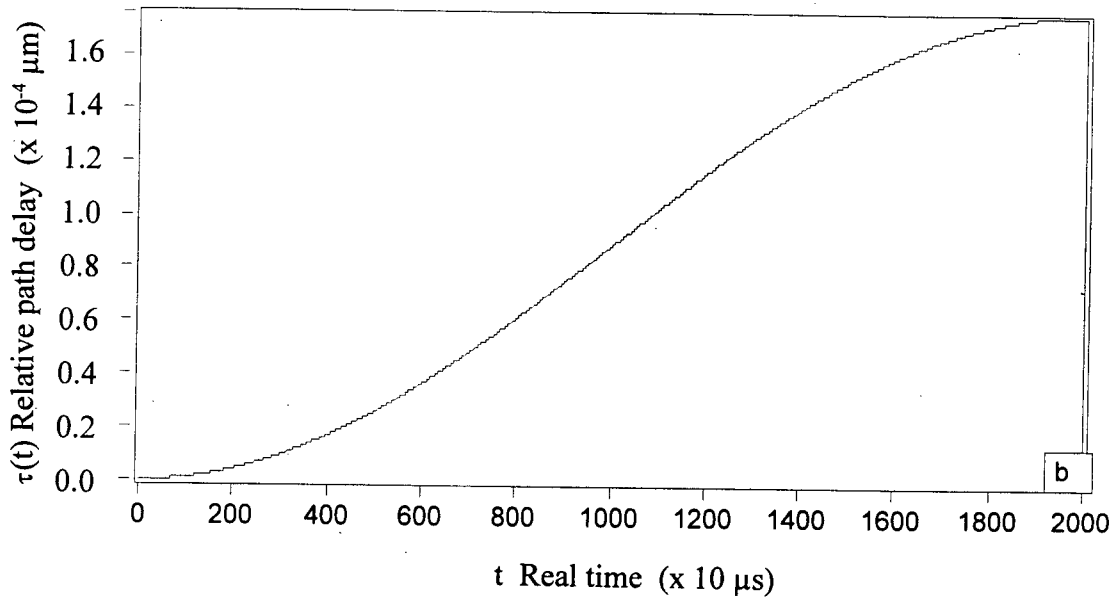
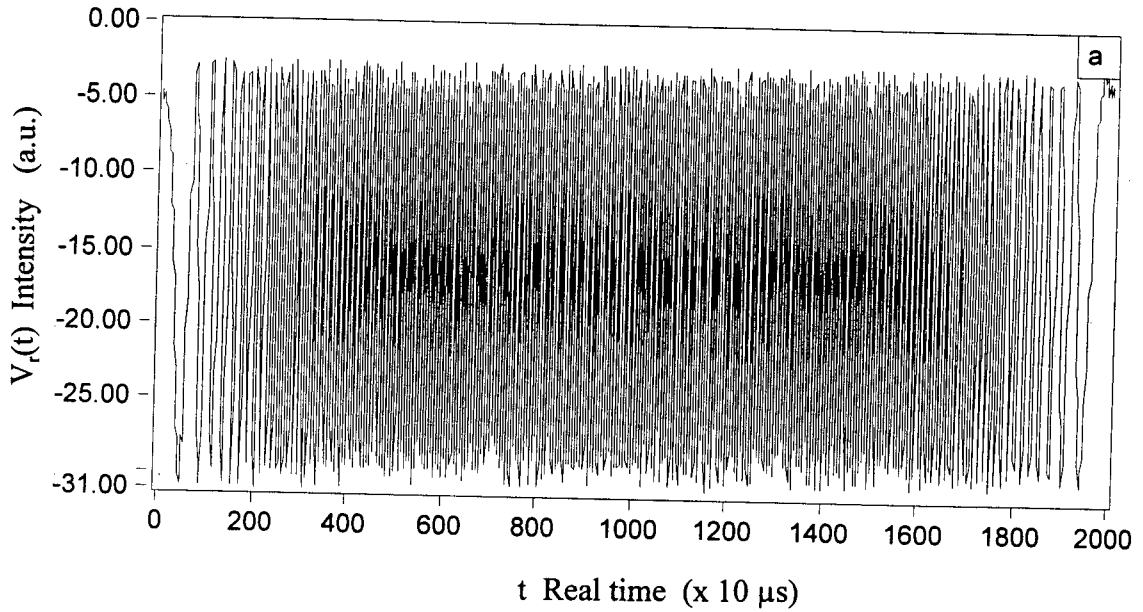


Fig.4.1 (a) A single cycle real time interferogram generated by the relative path delay interferometer. (b) The time dependent relative path delay decoded from the interferogram in Fig.4.1(a).

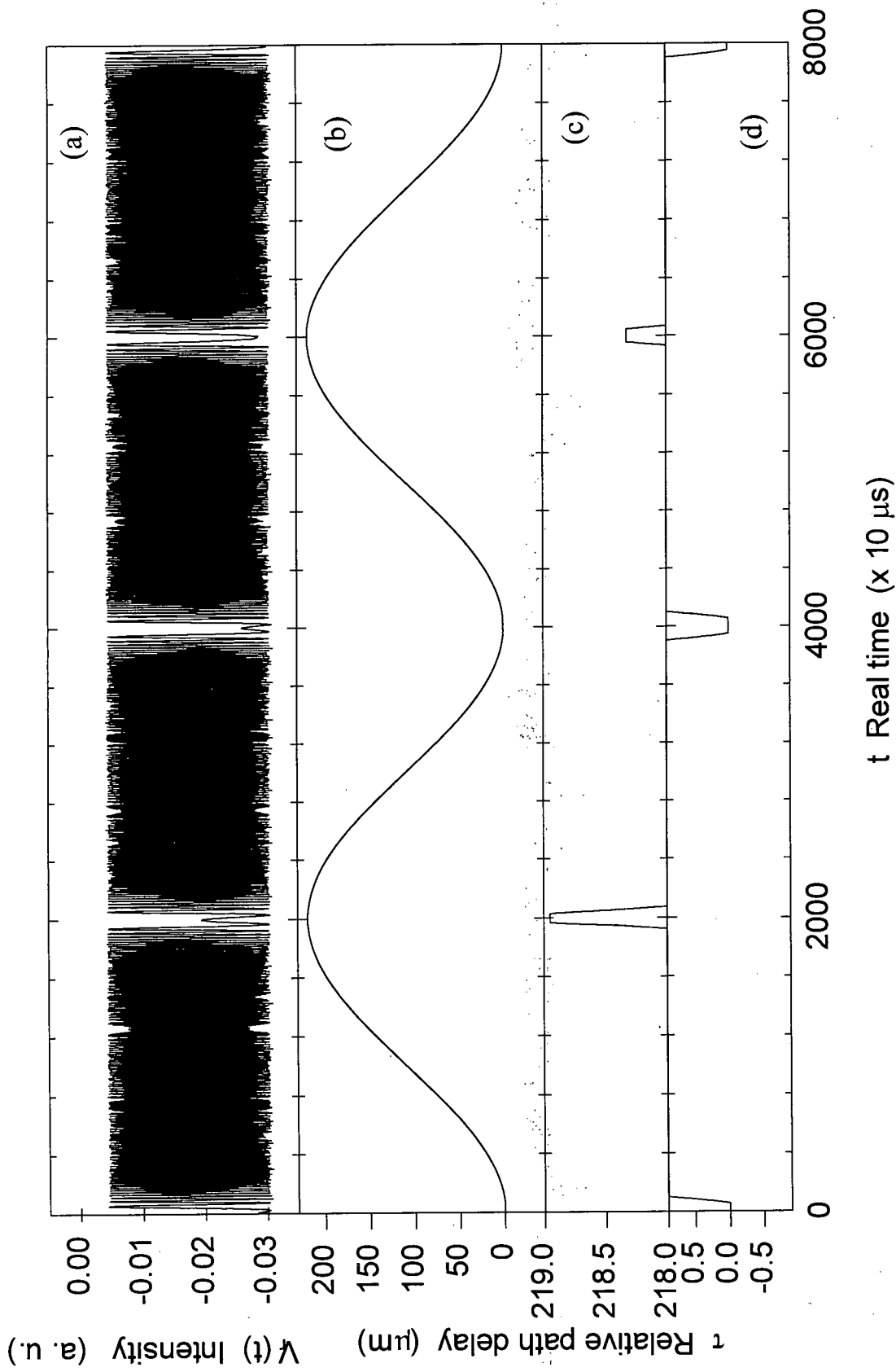


Fig.4.2 (a) 4 cycle real time interferogram from the relative path delay decoding interferometer, (b) its decoded relative path delay in real time space, and (c) and (d) its scale-expanded relative path delay near the turning points of the speaker's motion in real time space.

and signal interferograms must both be continuously recorded in order to actually map each cycle correctly onto relative path delay space. The non-periodicity of the speaker motion is largely due to low frequency acoustic "pickup": the speaker acts as a microphone.

The flat topped peaks in Fig.4.2 around the turning points are an artifact of the method used to identify the turning points (see discussion in Sect. 3.4). Fig.4.3 shows the reference interferogram signal near a turning point. In decoding, the algorithm uses symmetry to identify the turning point and to ascribe the same absolute relative path delay to points A and B in Fig.4.3. Detailed information about the relative path delay for points between these two points is difficult to obtain (see noise spikes on signal in Fig.4.3) and it is not needed, hence no decoding is done between points A and B.

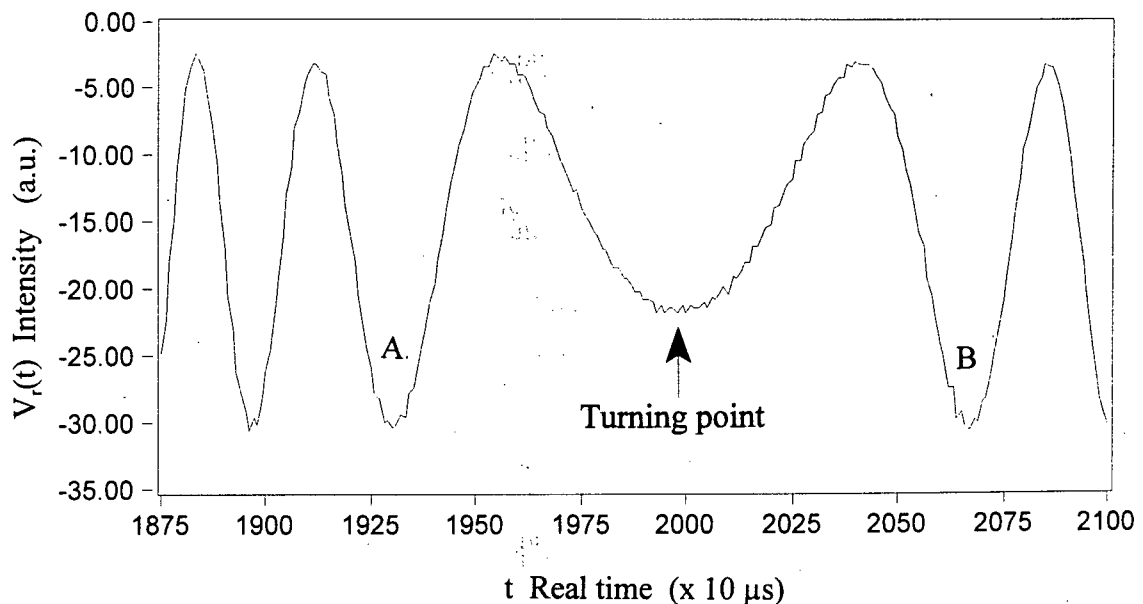


Fig.4.3 The real time interferogram in the low frequency region generated by the relative path delay decoding interferometer.

The analysis of the decoding algorithm in Chapter 2 assumed a noise-free interferogram and an arbitrarily high sampling rate. In the following two subsections, we discuss the decoding errors due to a limited sampling rate and due to noise in the decoding interferogram.

4.1.1 DECODING ERRORS FROM SAMPLING

Eqn. (2.10) can only be used to determine the relative path delay within one half wavelength. To keep track of the absolute relative path delay through the whole interferogram, it is necessary to identify each peak and trough in the interferogram and to increment the absolute relative path delay accordingly. Because the reference interferogram acquired by the computer consists of a set of discrete data points, due to sampling, there is always some error associated with the locations of peaks or troughs. If the closest sampled point to a peak or trough is assigned a half integral value for the corresponding relative path delay (in units of optical frequency), the maximum error for these points is

$$\delta\tau_{\max} \cong \frac{1}{2} \frac{\lambda_{\text{HeNe}}}{c} \frac{1}{N} \quad (4.1)$$

where c is the light velocity in vacuum and N is the number of samples per fringe.

In the present system the nonlinear speaker motion means that the uncertainty for fringe peak or trough location in the high frequency region is higher than that in the low frequency region. The minimum value of N is in practice $N_{\min}=5$, for which Eqn.(4.1) gives a maximum error in the decoded relative path delay of 0.2 fs.

4.1.2 DECODING ERRORS FROM NOISE IN THE REFERENCE INTERFEROGRAM

The accuracy of decoding sampled points between peaks and troughs, according to Eqn. (2.10), is not affected by any errors discussed above associated with the relative path delays at the peaks and troughs. However the accuracies of their decoding are affected by noise in the decoding interferogram signal due to fluctuations in the HeNe laser intensity and frequency, imperfect motion of the speaker, and detector noise.

In Chapter 2, the relationship between the relative path delay, τ , the measured interferogram signal, I_p , the signal intensity for the light field in one arm of the decoding interferometer, I , and the frequency, ν , was expressed as

$$\cos(2\pi\nu\tau) = \frac{I_p - (1 + \alpha^2) I}{2\alpha I} \quad (4.2)$$

where α is the branching ratio of the beam splitter.

The fractional error in the decoded delay, e_τ , therefore depends on the fractional errors in the interferogram intensity, e_{I_p} , the frequency, e_ν , and the peak interferogram envelope, e_I , as

$$e_\tau = e_\nu + \text{abs}\left\{ \frac{(1 + \alpha^2) + 2\alpha \cos(2\pi\nu\tau)}{4\pi\alpha\nu\tau \sin(2\pi\nu\tau)} \right\} (e_I + e_{I_p}) \quad (4.3)$$

The fractional error due to the stability in the frequency of the HeNe laser is less than 10^{-5} , so it can be neglected. The errors in decoding due to the HeNe laser mainly come from the stability

of the HeNe laser's output intensity and the detector noise. Remember that the τ in Eqn.(4.2) is the relative path delay with respect to an adjacent peak or a trough. The error in τ therefore tends to diverge near peaks or troughs. For simplification, let $\alpha = 1$ and assume there are N samples per fringe. Then the error in the decoded relative path delay for the n th sample after a peak or trough is

$$\begin{aligned} \delta\tau(t_n) &\approx \frac{4}{4\pi\nu \text{Sin}[2\pi\nu\tau(t_n)]} (e_{I^+} e_{I_p}) \\ &\approx \frac{1}{\pi\nu \text{Sin}(n\pi/N)} (e_{I^+} e_{I_p}). \end{aligned} \quad (4.4)$$

The bigger the sampling density, the more samples there will be near peaks or troughs, hence the larger the error is resulting from the noise in the interferogram. Thus, the decoding in the low frequency region is more sensitive to the fluctuation in the output of HeNe laser and the noise in the interferogram than that in the high frequency region. With realistic values of $N=50$, $n=1$, $e_I=1\%$ and $e_{I_p}=5\%$ in this equation,

$$\delta\tau \leq 0.6 \text{ fs}$$

in the low frequency region. But in the high frequency region ($N=5$), $\delta\tau < 0.1$ fs for points away from the peaks and troughs, and hence in this regime the errors are dominated by those due to sampling.

Fig.4.4 shows our measurement of $\delta\tau$ in the relative path delay decoding from a real time interferogram generated by the relative path delay decoding interferometer, in which $\delta\tau$ is defined as the difference between τ_e , the experimental decoding, and τ_{th} , the delay from a model fit

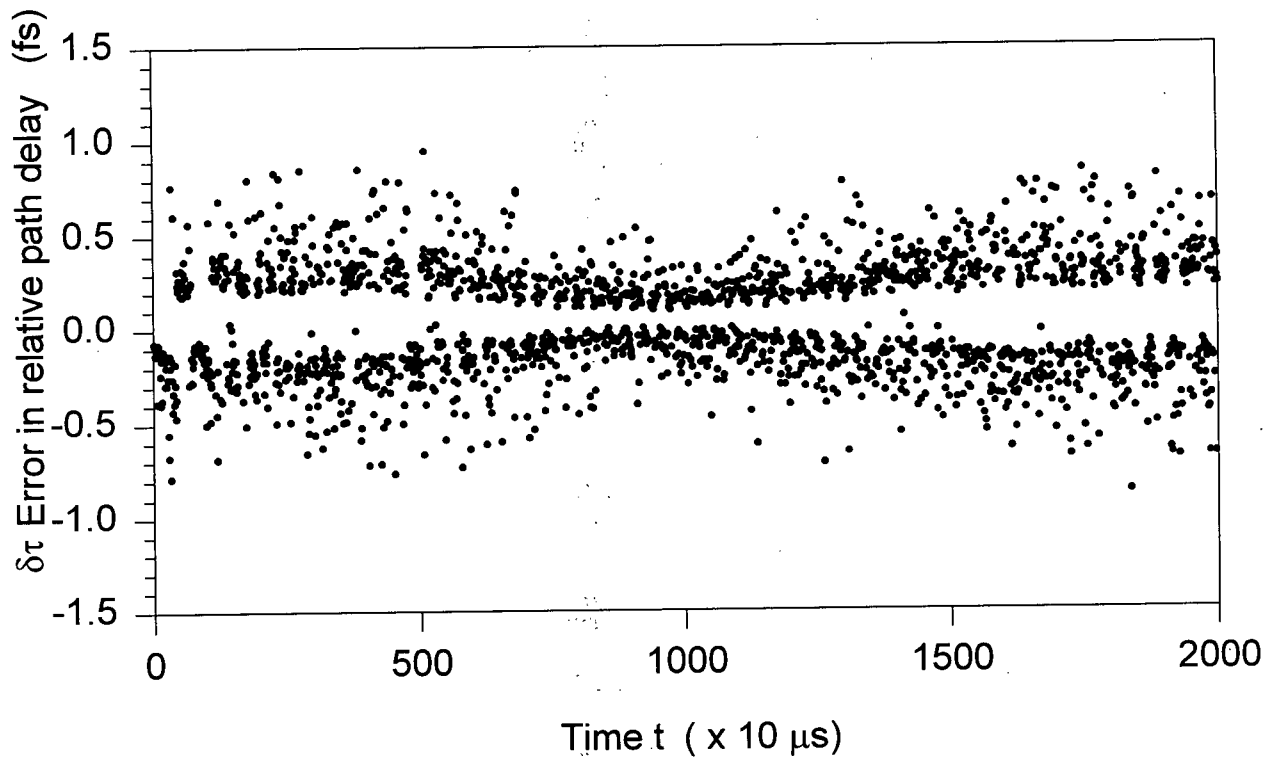


Fig.4.4 The error in relative path delay decoding over the full relative path delay range.

to the experimental data using

$$\tau(t) = a_0 + a_1 t + (a_2 + a_3 t) \cos(\omega t + \varphi) \quad (4.5)$$

where a_0 and a_2 describe the nominal shift and vibrational amplitude, respectively, φ describes the initial phase of the motion of the speaker, and a_1 and a_3 describe slow fluctuations of the null level and amplitude, respectively. From statistical analysis, 95% of the $\delta\tau$ are in the range of ± 0.6 fs, which gives a standard deviation of $\delta\tau \sim 0.3$ fs, which is consistent with the above error analysis.

Therefore, for this technique, errors due to the finite sampling rate alone, in a noise free situation, limit peak and trough locating accuracy to, at worst, 0.2 fs, in the high frequency part of the interferogram. Noise in the decoding interferogram signal introduces errors that are largest near peaks and troughs, and are therefore important in the low frequency parts of the interferogram where there is a high sampling density. Still this error is limited to ≤ 0.6 fs. Therefore if we define that the relative path delay resolution in this system as the maximum uncertainty in τ over the full relative path delay span, then it is better than 0.6 fs.

4.1.3 DECODER PARAMETER TESTING

Fig.4.5 (a) and (b) shows the decoded relative path delay for a fixed speaker amplitude of $A_0=0.065$ V and a speaker frequency of 10 Hz. At 10 Hz, the decoding is correct and limited only by the noise factors discussed above. The minimum number of sample points per fringe is $N_{\min}=5$. Fig.4.6 (a) and (b) show the same decoded signal but with the speaker frequency changed to 25 Hz. There are clearly errors in decoding, due to "missed" peaks and troughs in the high frequency regime where at 25 Hz there are only 2 samples per fringe. With at least 5 samples per fringe the decoding is robust. This can be achieved for a variety of combinations of the speaker amplitude and frequency. The lower the frequency the larger the total span of the speaker motion as expressed by Eqn. (3.4). Usable parameters and the corresponding maximum relative path delay spans are summarized in Table 4.1.

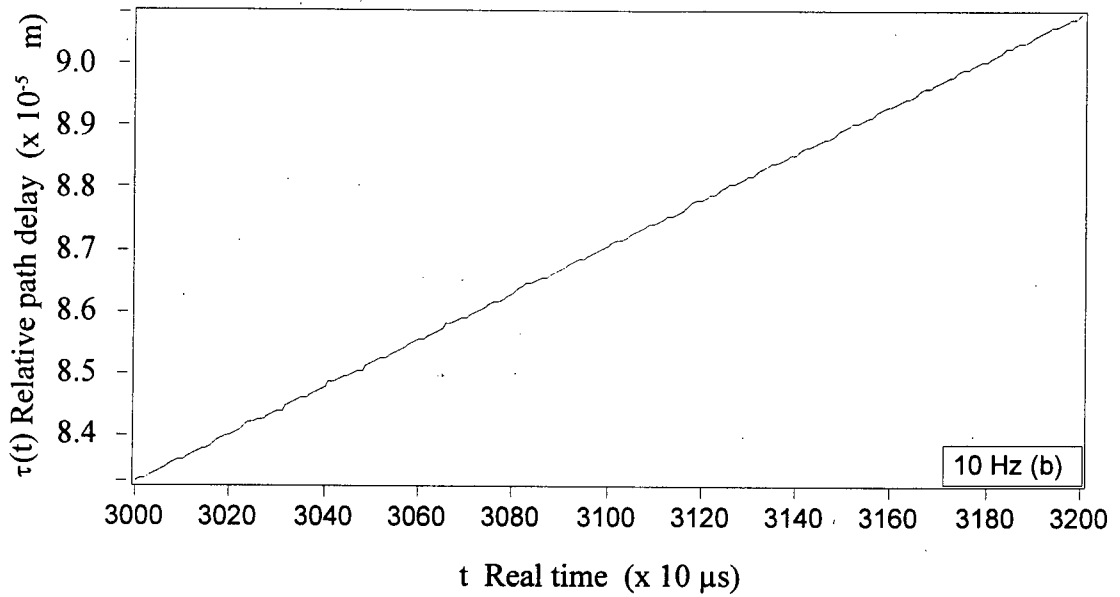
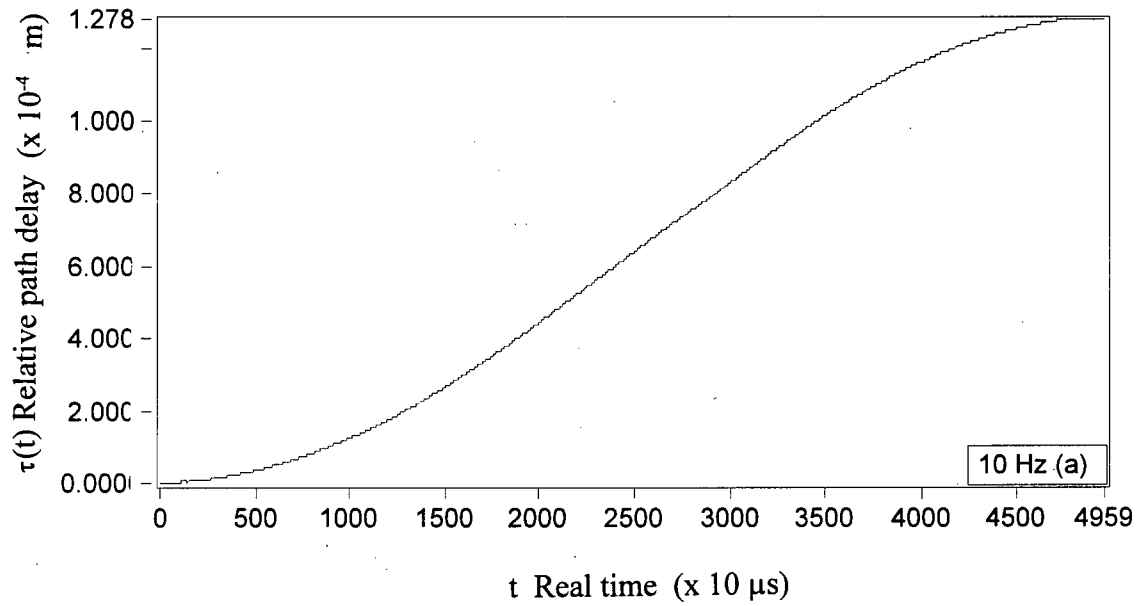


Fig.4.5 (a) The relative path delays deduced from a real time interferogram generated by the relative path delay decoding interferometer with scanning frequency of 10 Hz, and (b) the worst part in the decoding above.

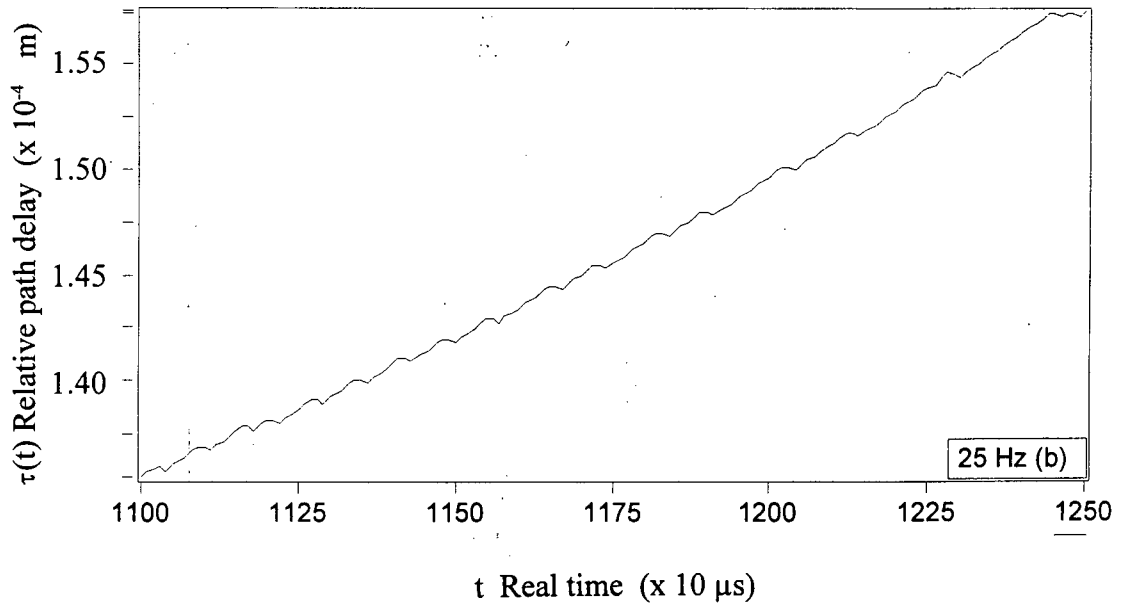
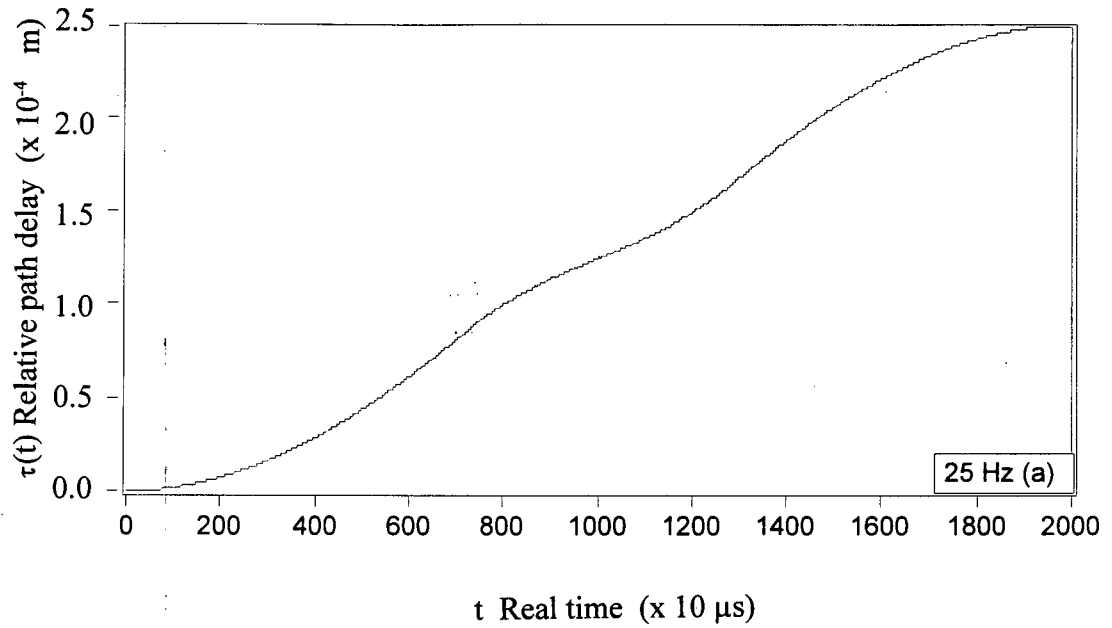


Fig. 4.6 (a) Effects of too high scanning frequency: the relative path delays deduced from a real time interferogram generated by the relative path delay decoding interferometer with scanning frequency of 25 Hz but the same scanning amplitude as that in Fig.4.6, and (b) the worst part of the relative path delay decoding above.

Table 4.1 Test results for reliable decoding at different speaker drive frequencies

Driving Frequency (Hz)	Driving Voltage (V)	Optical Delay Span (fs)
10	0.250	1088.3
20	0.170	1010.3
25	0.092	763.6

4.2 SIGNAL INTERFEROGRAMS (AUTOCORRELATION MODE)

This section describes the results obtained from the complete system when used in an autocorrelation mode with laser reference pulses in both arms of the signal generating interferometer. Since in this configuration the system is basically serving as an interferometric spectrometer, the results are quantitatively compared with those obtained from a commercial interferometric spectrometer from Bomem™.

4.2.1 LINEAR INTERFEROGRAMS

Fig.4.7(a) shows the linear interferogram signal in real time space obtained with approximately equal intensity mode-locked laser pulses in both arms of the signal generating interferometer. The interferogram consists of an aperiodic oscillation modulated by a slowly

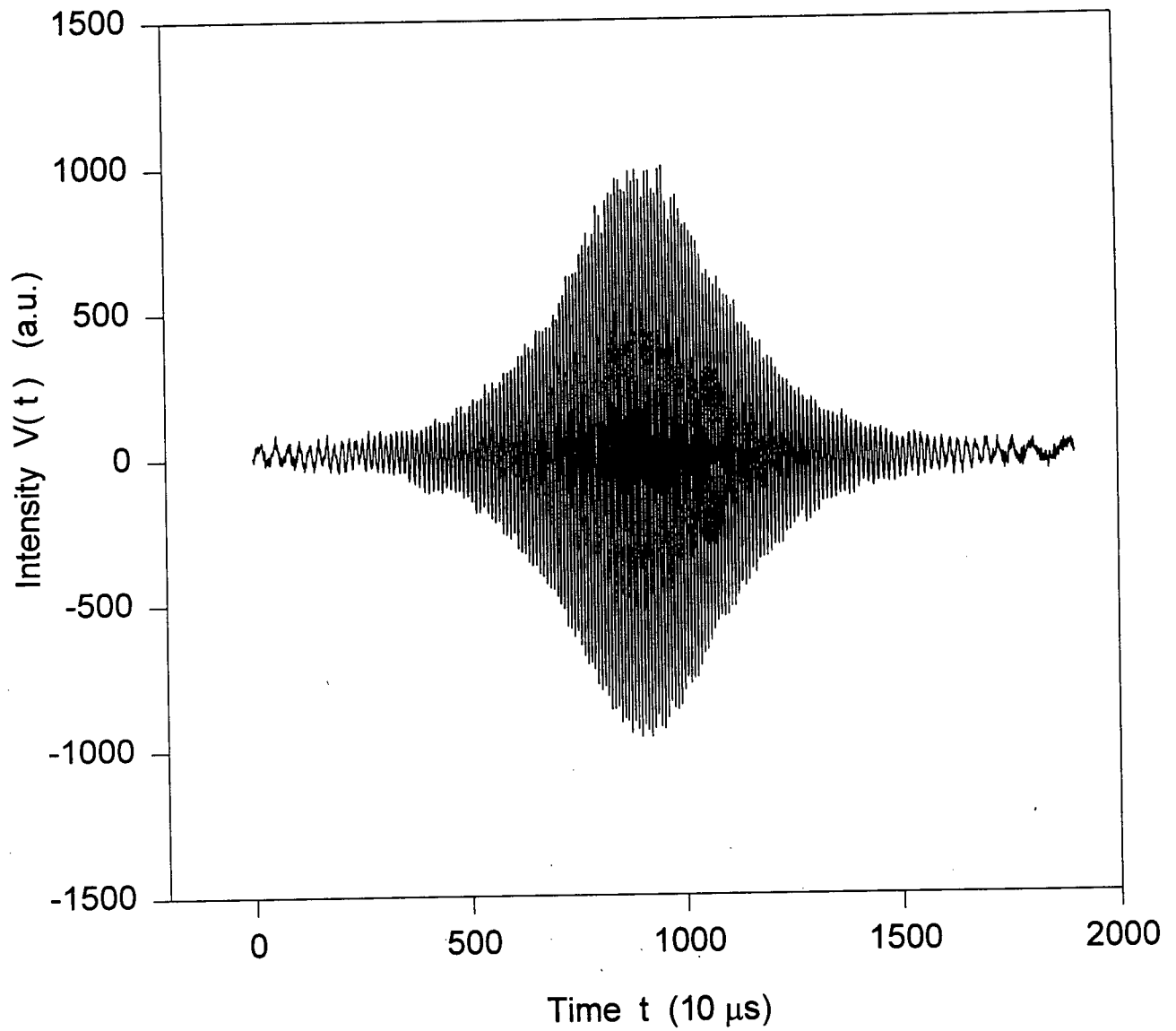


Fig.4.7 (a) A linear signal interferogram in real time space with a speaker frequency of 25 Hz and an amplitude of 0.065 V.

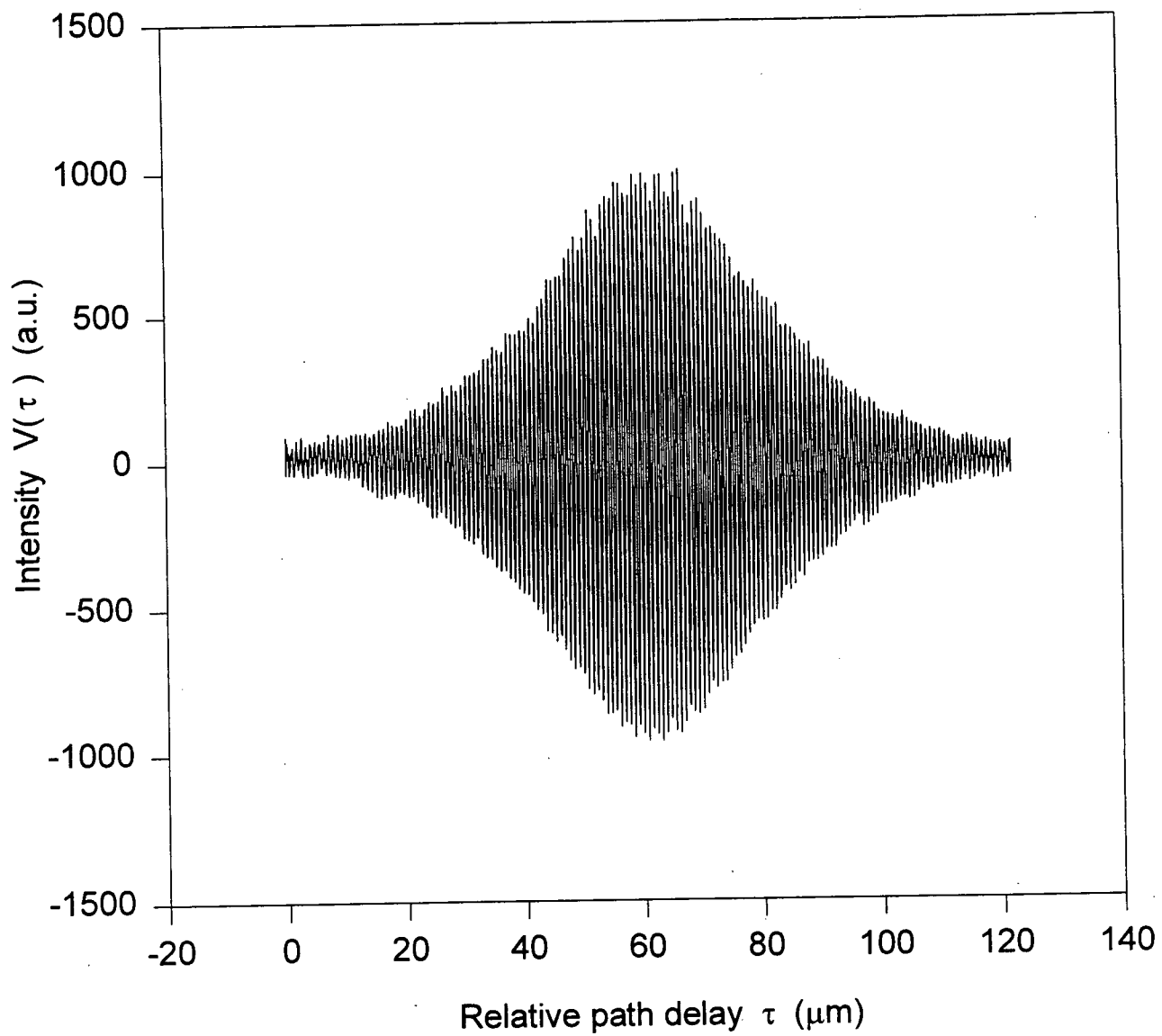


Fig.4.7 (b) The linear signal interferogram in relative path delay space converted from the real time interferogram in Fig.4.7(a).

varying envelopes. Fig.4.7 (b) shows the same signal in relative path delay space obtained using the corresponding decoding channel interferogram. As expected, the interferogram in relative path delay space is basically a modulated monotone.

The interferogram signal in Fig.4.7 appears "noisy". This is partly due to the printing resolution, but there is also a contribution from true system noise. It is well known that noise due to mechanical vibrations, etc. is the biggest problem in interferometer performance. In standard slow-scan interferometers it can be reduced by the use of servo-vibration-reducing optical components and by the co-addition of multiple interferograms. Part of the motivation for testing the present rapid-scan system was to avoid the need for low frequency servo systems by acquiring several complete interferograms on relatively short time scale. Co-addition of these interferograms should improve the signal to noise ratio by reducing effects of random noise. Effects due to systematic errors, from, for instance, the decoding algorithm, will not be removed by this procedure.

The procedure developed to reduce the random noise by multicycle averaging in this system is as follows. First, data consisting of several consecutive cycles of interferograms is acquired. Second, the relative path delay for the entire set of data is decoded from the decoding interferogram. Third, the data pairs (relative path delay and intensity) from all cycles are sorted into equal width relative path delay space bins according to the value of the relative path delay for each data pair. Then, the relative path delay axis is partitioned into several bins with identical widths. Finally, the intensity average and the standard deviation for each bin are obtained to produce an averaged single cycle interferogram.

Fig.4.8 shows eight consecutive decoded interferograms overlapped on an expanded relative path delay space scale. On choosing a suitable bin width for averaging there are tradeoffs between

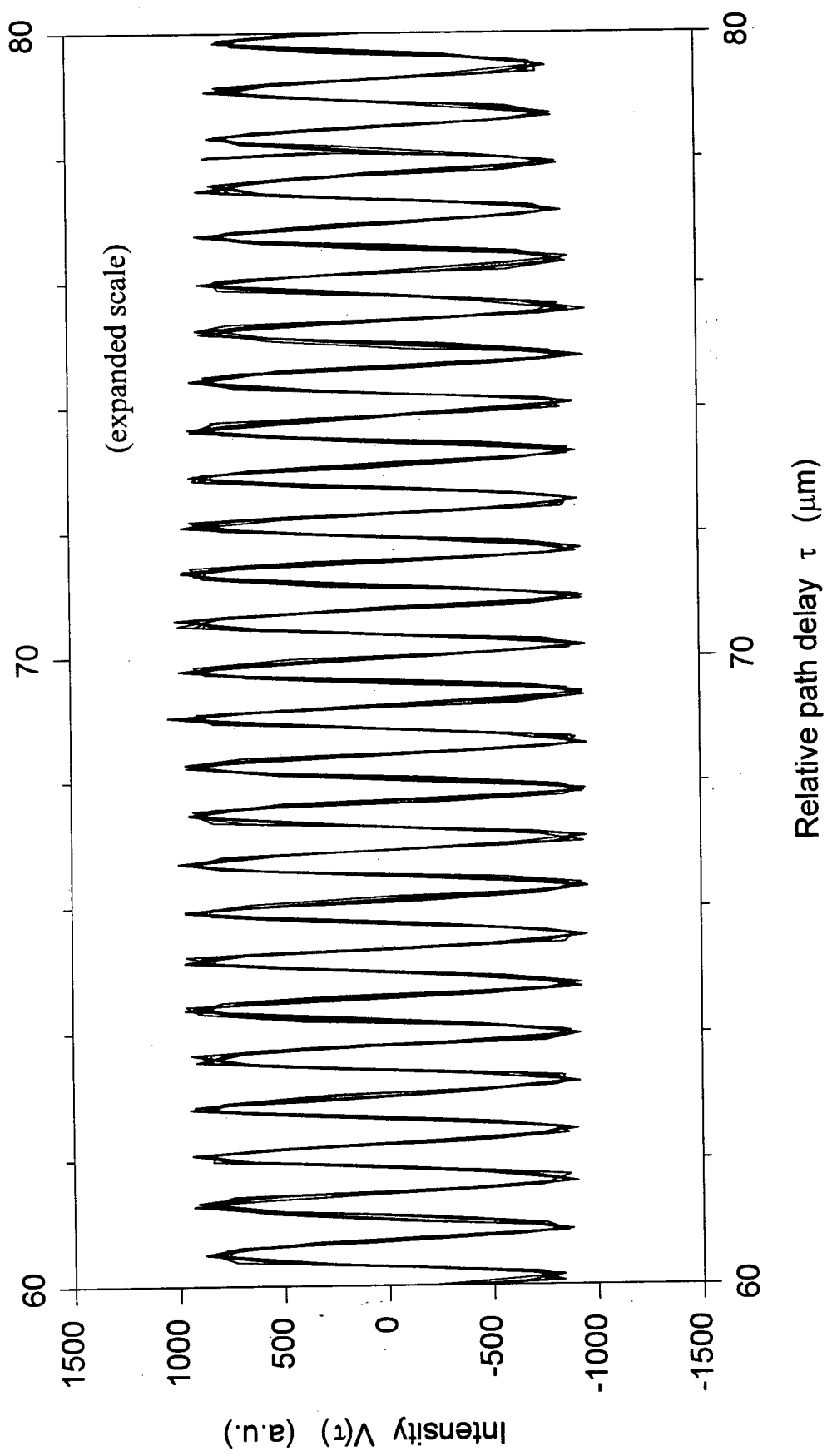


Fig.4.8 The interferogram consisting of samples from 8 cycles of the scanner.

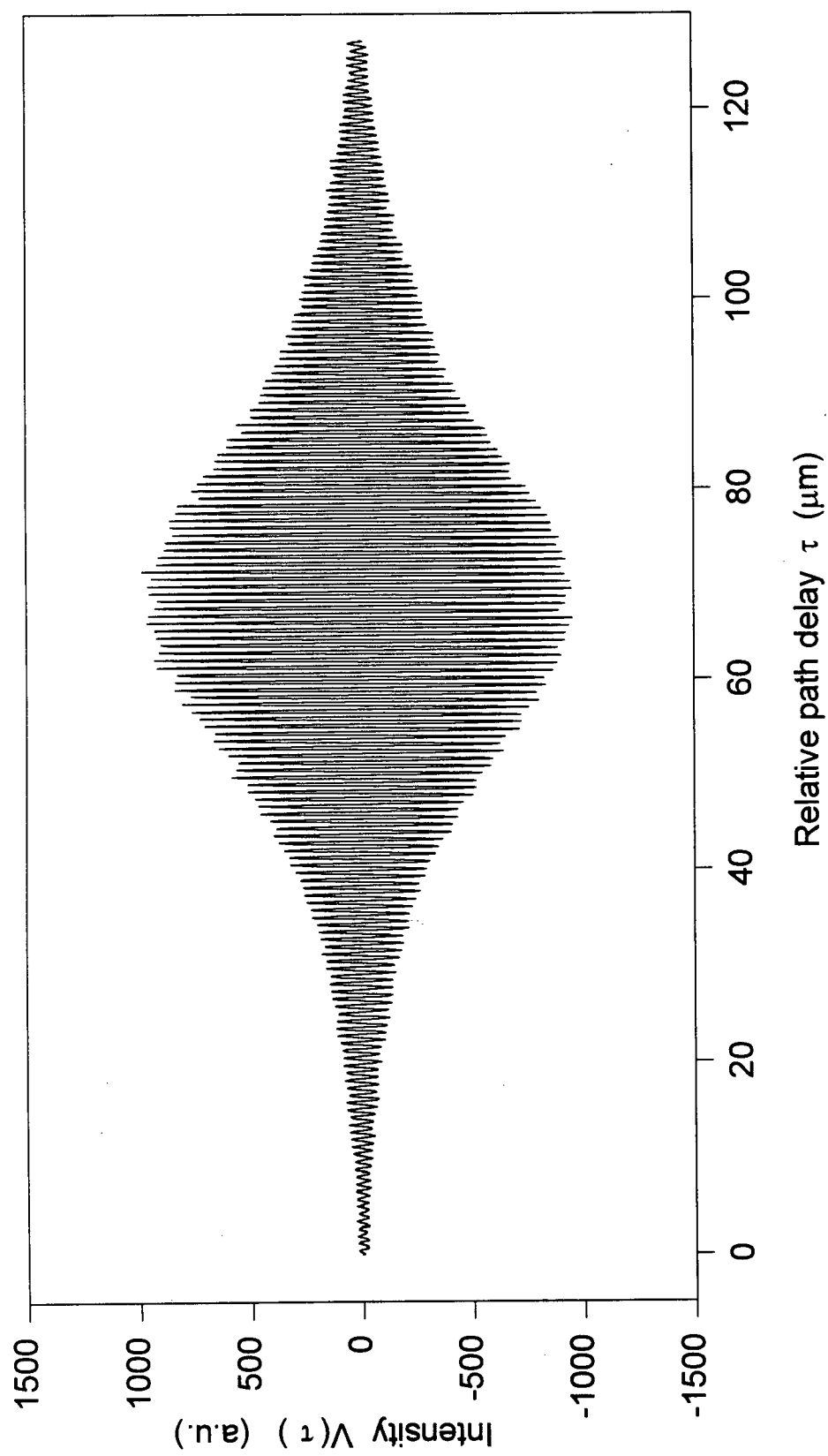


Fig.4.9 (a) The interferogram averaged from the 8 cycle interferogram generated by the signal generating interferometer with an averaging window width of 0.2 fs.

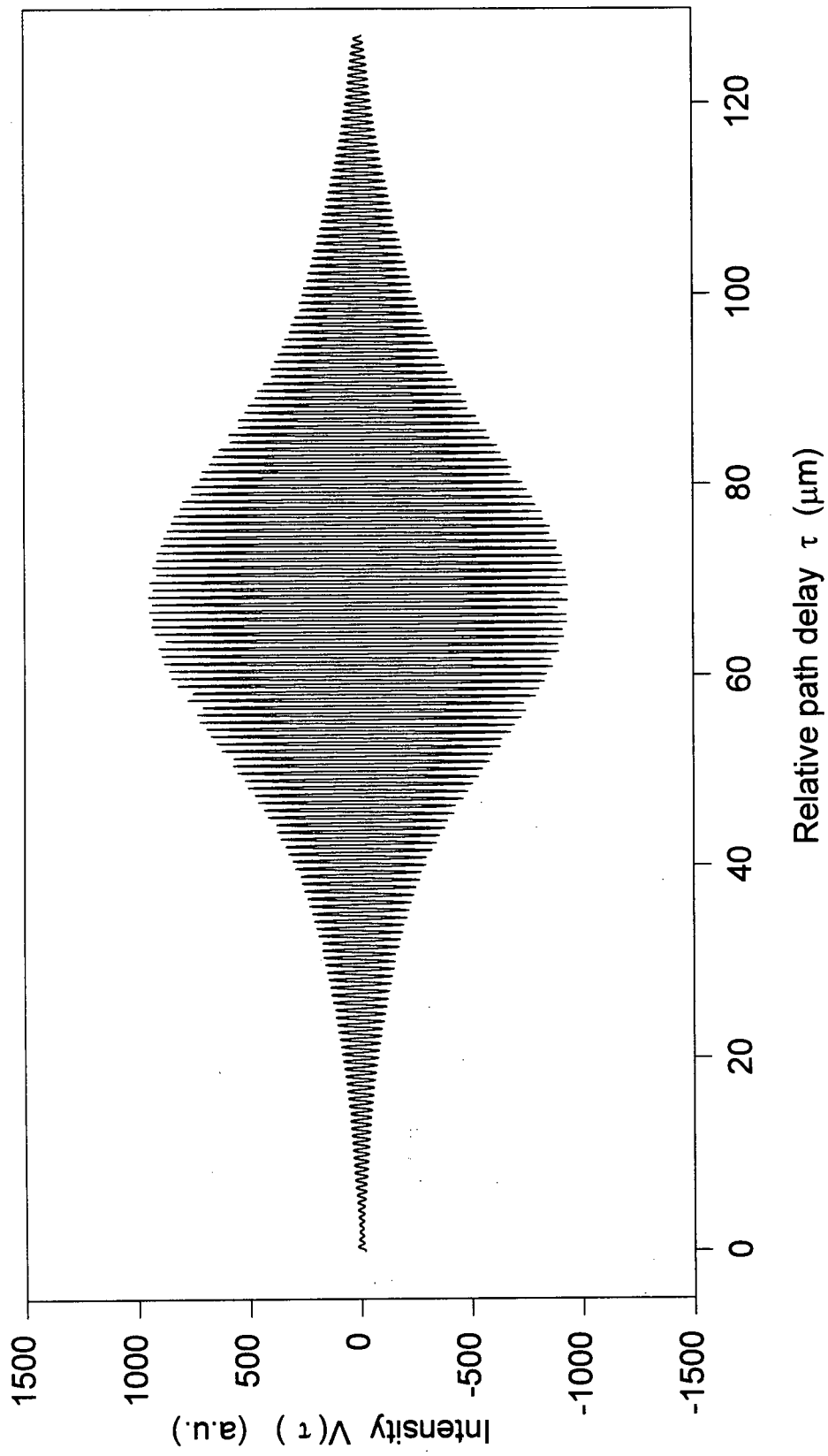


Fig.4.9 (b) The polynomial simulation of the interferogram in Fig.4.9 (a).

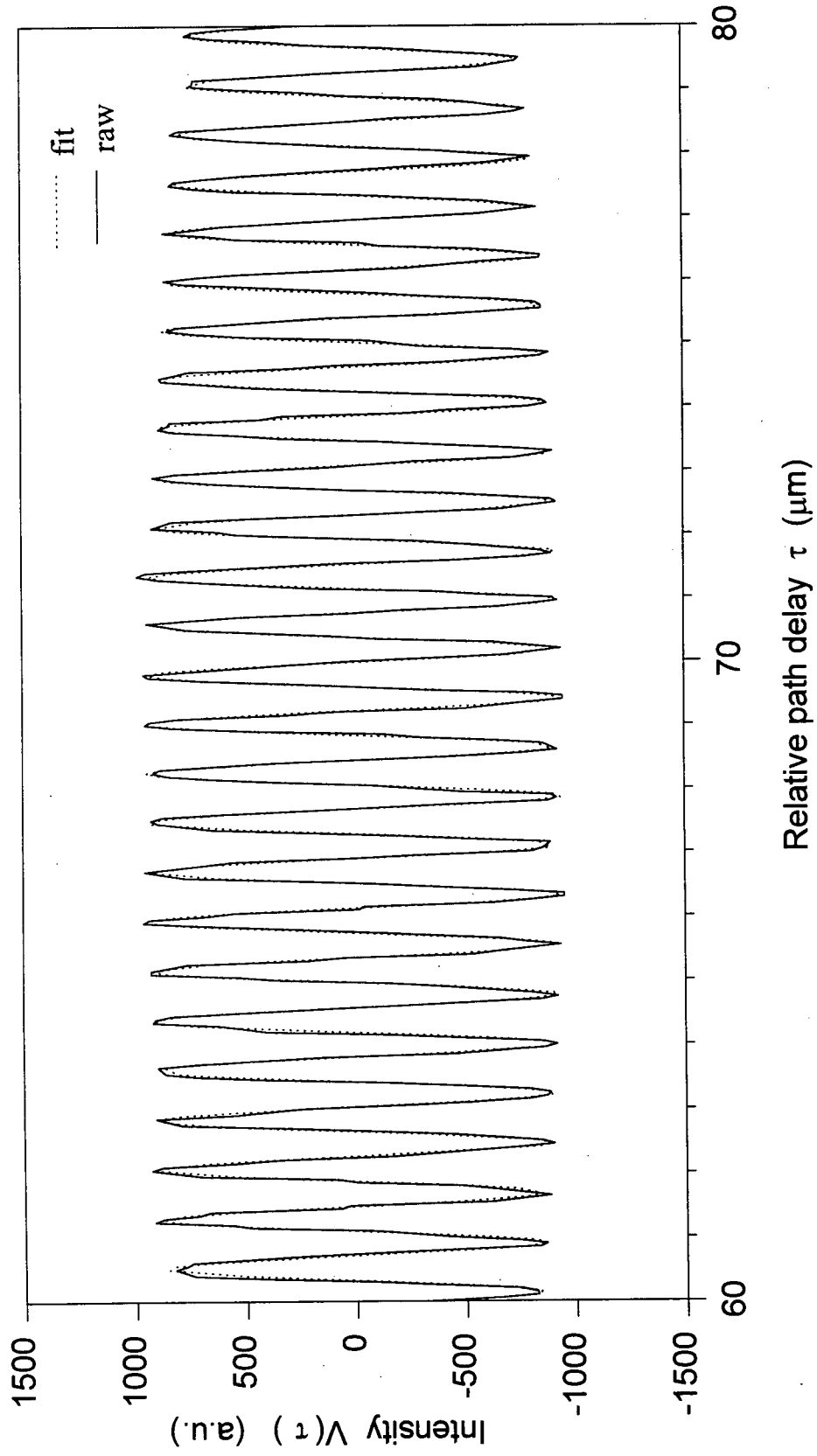


Fig.4.9 (c) The interferogram in Fig.4.9 (a) and its polynomial simulation in expanded scale.

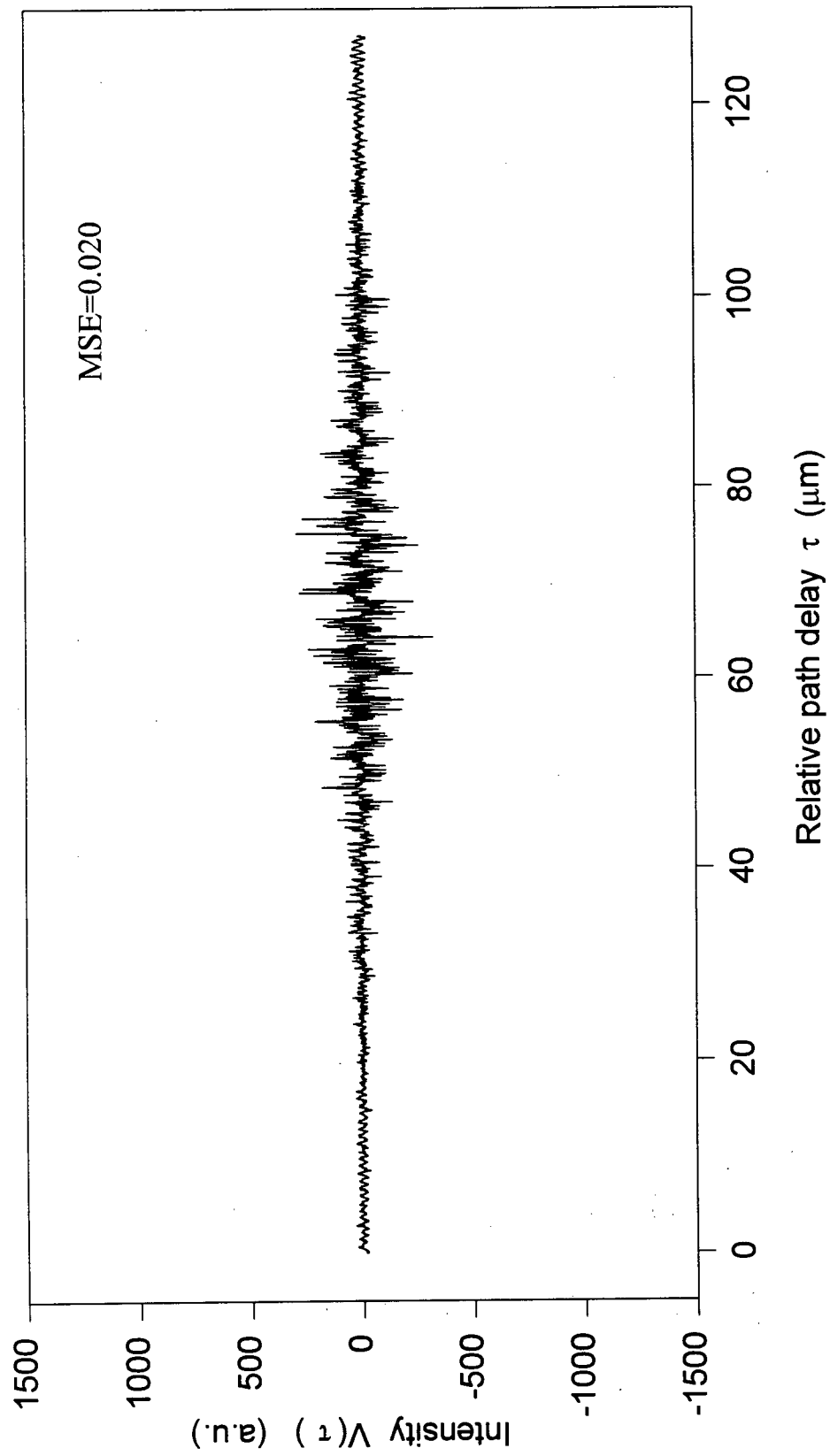


Fig.4.9 (d) The residuals of the polynomial simulation of the interferogram in Fig.4.9 (a).

the degree of averaging and degradations in the time resolution. In this regard the aperiodic motion of the speaker is in fact a benefit because the bin size can be set to the minimum sampling step size, thus not compromising temporal resolution, while slight changes in the exact delay at which the signal is sampled from period to period tend to provide a good distribution of data within the bins for averaging purposes. Fig.4.9(a) is the interferogram averaged from the 8 cycle interferogram in Fig.4.8 using a bin size of 0.2 fs, equivalent to the minimum sampling interval in relative path delay space.

As a means of quantifying the effects of signal averaging, the variously averaged interferograms were fit to a function of the form as predicted by Eqn.(2.25)

$$V_{th}(\tau) = a_0 + EN(\tau) \cos[\phi(\tau)] \quad (4.6)$$

where a_0 corresponds to the DC background signal, $EN(\tau)$ is the slowly varying envelope, and $\phi(\tau)$ is the interferogram phase. Polynomial expansions were used for $EN(\tau)$ and $\phi(\tau)$:

$$EN(\tau) = b_0 + b_1 \frac{\tau - a_2}{a_1} + b_2 \left(\frac{\tau - a_2}{a_1} \right)^2 + b_3 \left(\frac{\tau - a_2}{a_1} \right)^3 + \dots \quad (4.7)$$

$$\phi(\tau) = c_0 + c_1 \left(\frac{\tau - a_2}{a_1} \right)^2 + c_2 \left(\frac{\tau - a_2}{a_1} \right)^3 + \dots$$

where a_2 determines the relative path delay zero location in relative path delay space and a_1 is a measure of the pulse duration.

In the simulation procedure, the mean square error of the theoretical simulation to the experimental measurement, MSE was defined as

$$MSE = \frac{1}{M} \sum_{i=0}^{M-1} [V_{th}(\tau_i) - V_e(\tau_i)]^2 \quad (4.8)$$

where M is the number of samples in the measurement and $V_e(\tau_i)$ is the experimental signal at relative path delay τ_i .

The Levenberg-Marquardt (L-M) method [Ref.38] was used to optimize the MSE to a precision of 10^{-3} . Fig.4.9(b) shows the polynomial fit of the interferogram in Fig.4.9(a), which is averaged from the interferogram consisting of samples from 8 cycles of the scanner, as shown in Fig.4.8, with an averaging window width of 0.2 fs. Terms in Eqn.(4.7) up to the fifth order in the phase shift and to the 15th order in the envelope were used. Fig.4.9(c) presents both the measurement and the simulation on an expanded scale, and Fig.4.9(d) shows the difference between the measured interferogram and the fit interferogram. Fig.4.10 summarizes the MSE data as a function of the number of cycles averaged from 1 cycle to 8 cycles. Multicycle averaging decreases

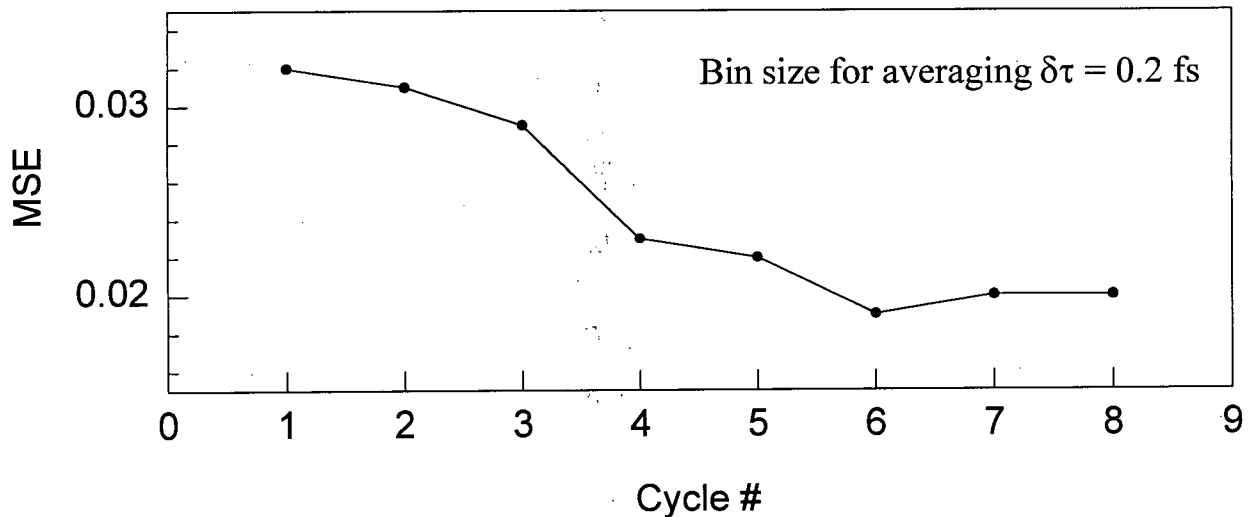


Fig. 4.10 Quantitative evaluation of the efficiencies of the multicycle averaging method on noise reduction.

the MSE from 0.034 to 0.020 for only 8 cycles of averaging.

The memory size in the personal computer limited this analysis to 8 cycles. Further analysis on larger data sets (see Sect.5.2 for recommendations for further work.) is necessary to determine if further averaging would help improve the signal to noise ratio, or whether the systematic noise floor has been reached at 8 cycles.

4.2.2 NONLINEAR INTERFEROGRAMS

Second order interferogram can also be easily obtained with this system. This is relevant because, as described in Sect.2.6, in order to extract the maximum information about an unknown signal field, the reference field must be well characterized. The linear auto-correlation shown above only gives information about the reference power spectrum. Additional information can be obtained by analyzing higher order correlations of the reference field with itself, as can be obtained by frequency doubling, tripling, etc. the output of the signal generating interferometer before detection.

The only difference in the hardware configurations between linear interferogram acquisition and the second order interferogram acquisition is the addition of a lens after the output beam splitter that focuses the overlapped light field from two arms of the signal generating interferometer onto a KDP nonlinear optical crystal to generate a second harmonic signal, and then a color filter is used to cut off the fundamental laser signal from the output of the crystal. The second harmonic signal is much weaker than the linear signal, hence a photomultiplier tube (PMT) with a bias of 1 KV is used to detect the second harmonic signal.

A representative second order interferogram is shown in Fig. 4.11, which was acquired under the same condition as those shown in Fig. 4.7. Instead of being symmetric like the linear

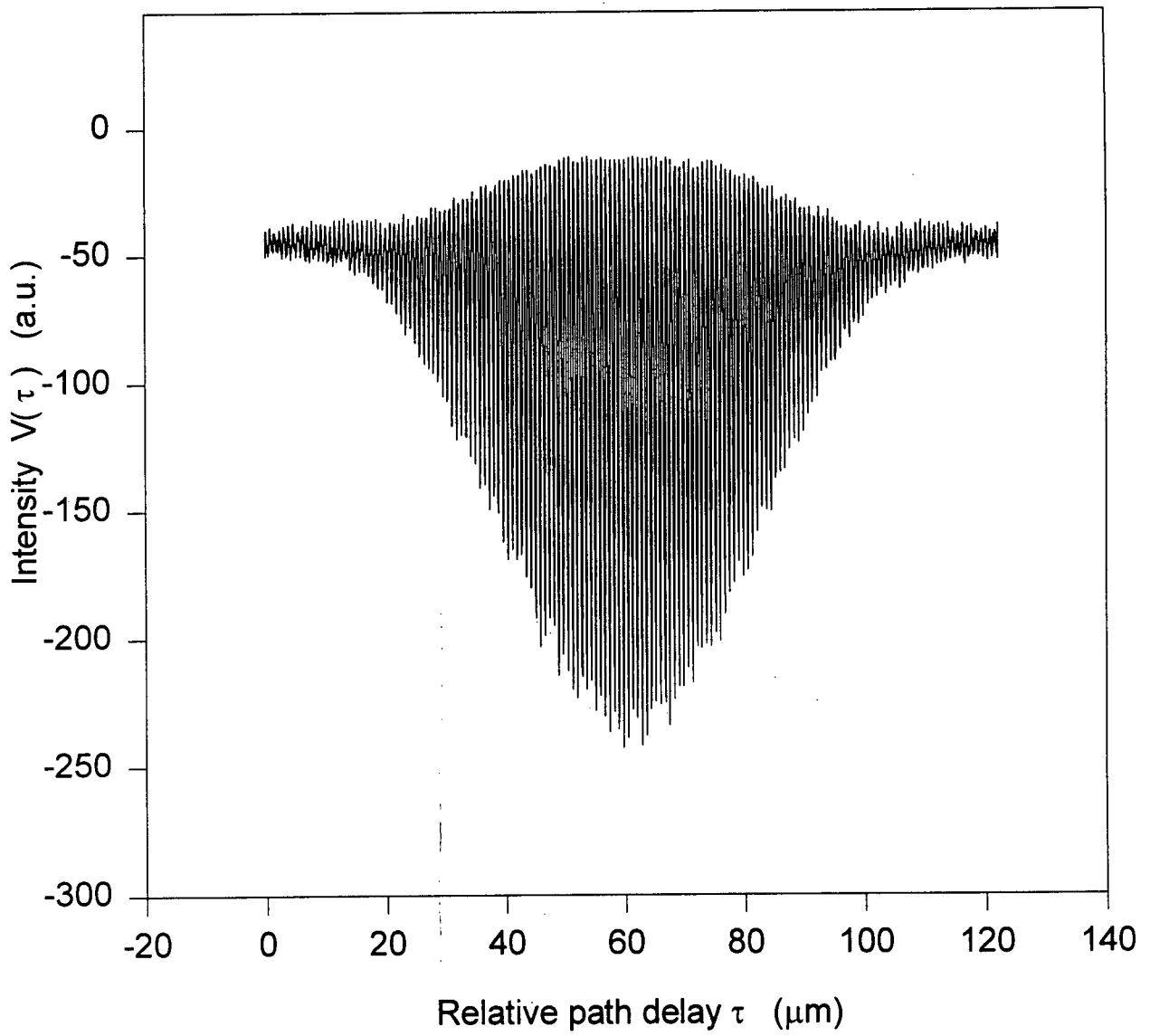


Fig.4.11 The nonlinear signal interferogram in relative path delay space with a speaker frequency of 25 Hz and an amplitude of 0.065 V.

interferogram, the second order interferogram is completely asymmetric with respect to the DC level at long delays. The details of interpreting the second order interferograms can be found in [Ref. 14]. In this thesis, we focus only on the linear interferograms.

4.2.3 POWER SPECTRUM OF THE REFERENCE PULSES

As described in section 2.5 in Chapter 2, under ideal conditions the Fourier transform of the signal pulses can be deduced from the Fourier transforms of the cross correlation and reference pulse auto-correlation signals. These transforms can be easily obtained from the decoded interferograms, in principle. There is a practical complication due to the fact that in this system, even though the interferogram consists of a data set sampled evenly in real time space, this data set is unevenly distributed in relative path delay space, and most numerical FFT algorithms available now are based on evenly sampled data sets. This problem is dealt with by generating an evenly sampled interferogram from the polynomial model fit (Sect.4.2.1) to the actual interferogram, and using a standard FFT algorithms on this data set.

The numerical FFT of the interferogram in relative path delay space from the auto-correlation measurement should give the intensity spectrum of the input pulse. To examine the performance of this system, we measured the auto-correlation interferogram of the ultrashort pulses of duration ~ 70 fs and center wavelength of 805.1 nm and compared its Fourier transform with the intensity spectrum of the same pulses obtained using the FTIR system from Bomem. Fig.4.12 presents the results. The solid line is the amplitude of the numerical FFT of the auto-correlation interferogram obtained by this system, and the dashed line is the intensity spectrum measured by the Bomem system. The spectrum obtained using the rapid-scan system is essentially a lower resolution version

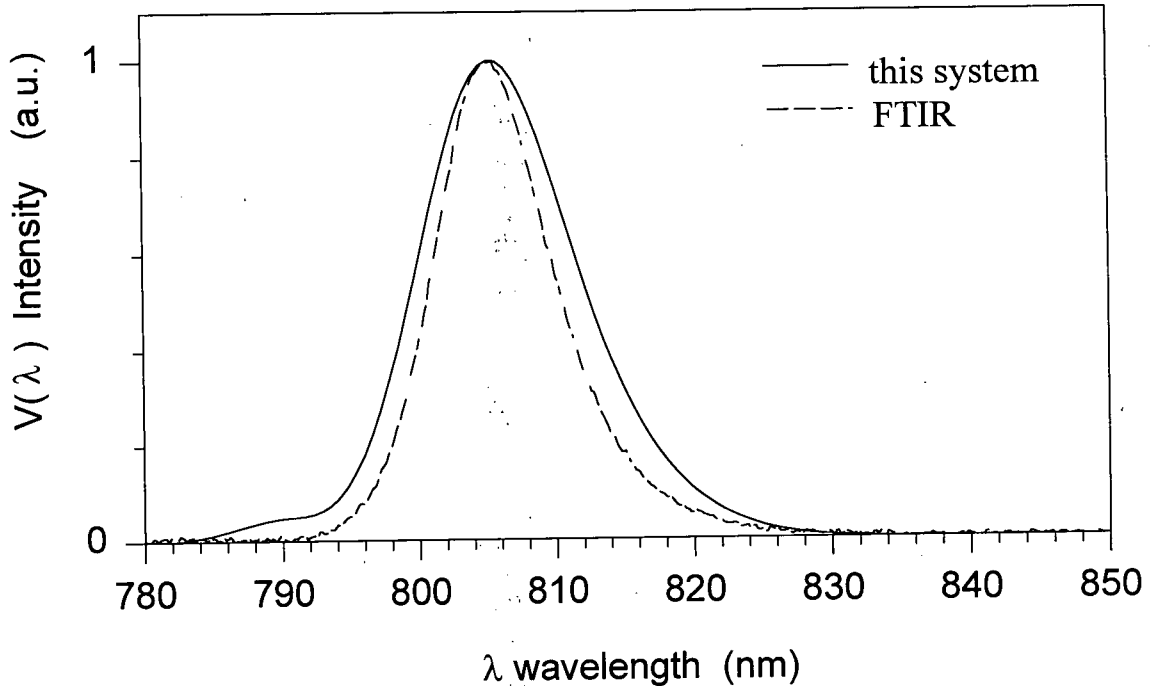


Fig.4.12 The intensity spectrum of a 70 fs pulse with center wavelength of 805.1 nm from the FFT of the interferogram generated by this system and that obtained by the FTIR from Bomem Co.

of that obtained using the Bomem instrument. Both show that the intensity spectrum is asymmetric with the distribution steeper on the shorter wavelength side than on the longer wavelength side, and the center wavelengths from both traces are the same with accuracy of 0.1 nm. The Bomem spectrum was obtained at a resolution of 4 cm^{-1} and it is therefore well resolved, while the speaker scan range of $\pm 45 \text{ } \mu\text{m}$ used to obtain the rapid-scan spectrum corresponds to a resolution of only 211 cm^{-1} .

4.3 CHARACTERIZATION OF TI:SAPPHIRE LASER OUTPUT: AUTOCORRELATOR

For virtually all applications it is important to characterize the reference pulses produced directly from the laser to some extent. The degree of characterization depends on the application.

The present system is capable of recording linear interferograms and nonlinear interferograms produced by putting the output of the interferometer through nonlinear optic crystals before the square-law detector. Linear auto-correlations provide the power spectrum of the pulses while nonlinear interferograms can be analyzed to deduce more subtle information about the phase of different frequency components. As shown in the previous section, the power spectrum is obtained by Fourier transforming the linear auto-correlation interferogram. In many cases, especially when "tweaking up" the laser system, it is very convenient to have a quick and accurate method of measuring the center wavelength and pulse duration. This section describes the way this is accomplished with the present system.

The autocorrelation interferogram consists of a series of uniformly spaced fringes, modulated by a slowly varying envelope in relative path delay space, as discussed in Chapter 2. Putting $f_1 = f_2$ and $\phi_2 - \phi_1 = 0$ into Eqn.(2.25), we can find the space between fringes in relative path delay space is equal to the center wavelength of the laser pulse and the envelope of the interferogram is related to the envelope of the laser pulse as long as the dispersion is compensated. Thus, operated as an autocorrelator for short pulse lasers, this system can be used to monitor the evolution of the mode-locking status in the laser system and the center wavelength of the laser pulses. Using a simple model of the laser pulse, this system can also provide a good estimate of the laser pulse duration.

There are four steps to have this system work as an simple autocorrelator:

1. Take out the block and the signal input reflector, M8, in the signal arm of the Mach-Zehnder interferometer in Fig.3.1, and realign the signal arm to be collinear with the reference arm after the cubic beam splitter.
2. Run the speaker driver: open **Signal Generator.vi** in Labview\r.lib, with appropriate parameter inputs.

3. Find the prescan number, window settings for the turning point finder, and the cutoff number for the relative path delay decoding VI by running the data acquisition VI: **Acq & Proc(Reference Only).vi**.
4. Run the signal data acquisition and processing VI: **Acq & Proc(Two channels only).vi** or **Acq & Proc(two channels).vi**. Both of them can be run in continuous or single acquisition mode. If used to monitor the evolution of the mode-locking quality, they can be run in continuous mode, then it works essentially as an oscilloscope. To determine the center wavelength and pulse duration it is necessary to run them in finite acquisition mode.

4.3.1 EVOLUTION OF MODE-LOCKING STATUS

Fig.4.13 (a), (b) and (c) show the evolution of the auto-correlation interferograms of the output laser pulses from a Tisapphire laser system as a function of the optical dispersion compensation from the prism pair in this laser system (Pr2 and Pr3 in Fig.3.2). With little compensation the interferogram is similar to that due to a cw light source as shown in Fig. 4.13 (a). With some compensation of the optical dispersion from the prism pair, the fs pulse field starts to establish itself. The higher the compensation, the stronger is the pulse field and the weaker is the cw background field as shown in Fig.4.13 (b), which means some of the lasing modes in the laser cavity are mode locked but others are not. Finally when the optical dispersion is properly compensated, the strong fs pulse field is established and there is almost no cw background as shown in Fig.4.13 (c).

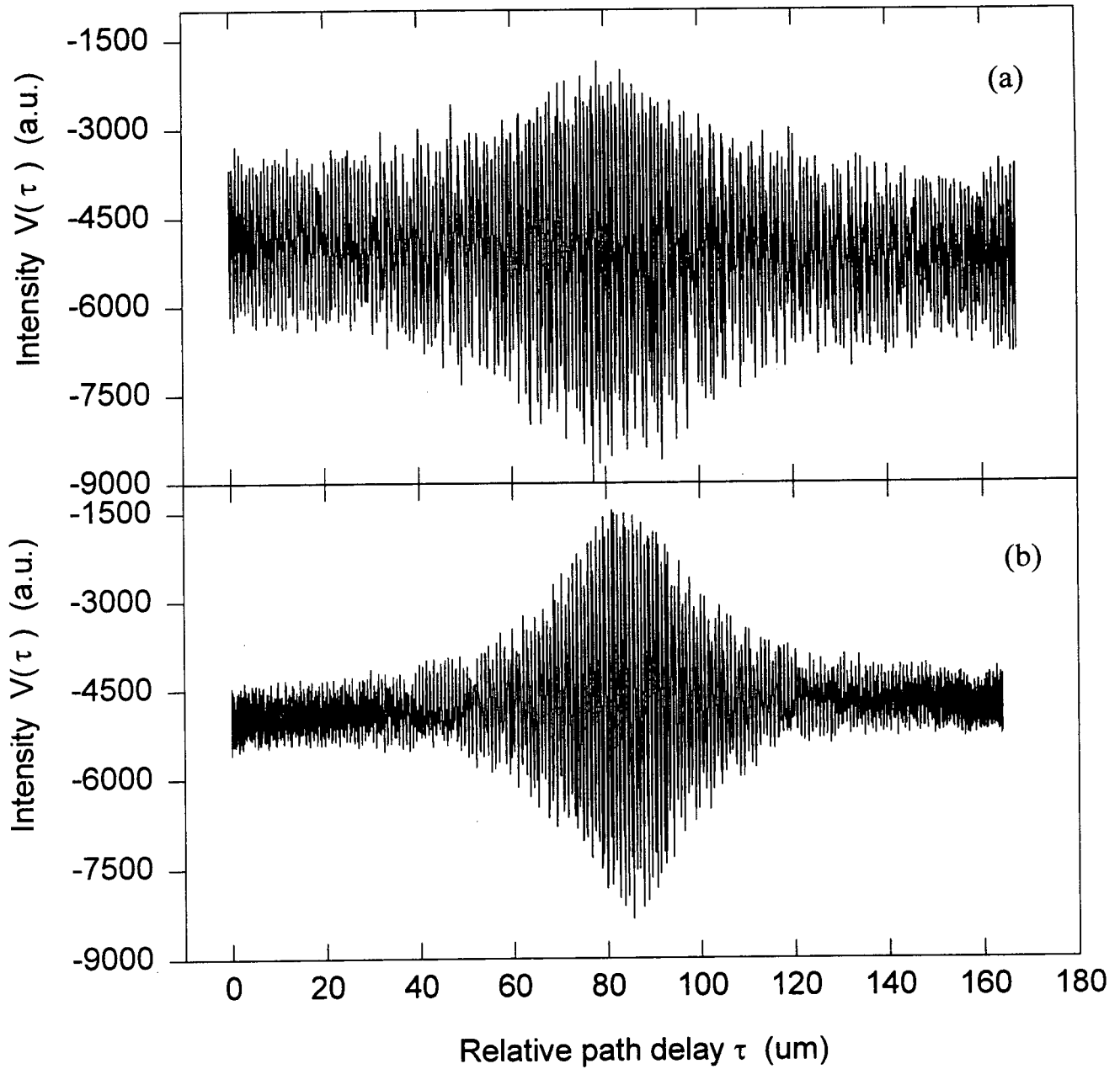


Fig.4.13 (a) The interferogram in relative path delay space generated from a poor mode-locked Ti:sapphire laser output. (b) The interferogram in relative path delay space generated from a better mode locked Ti:sapphire laser output.

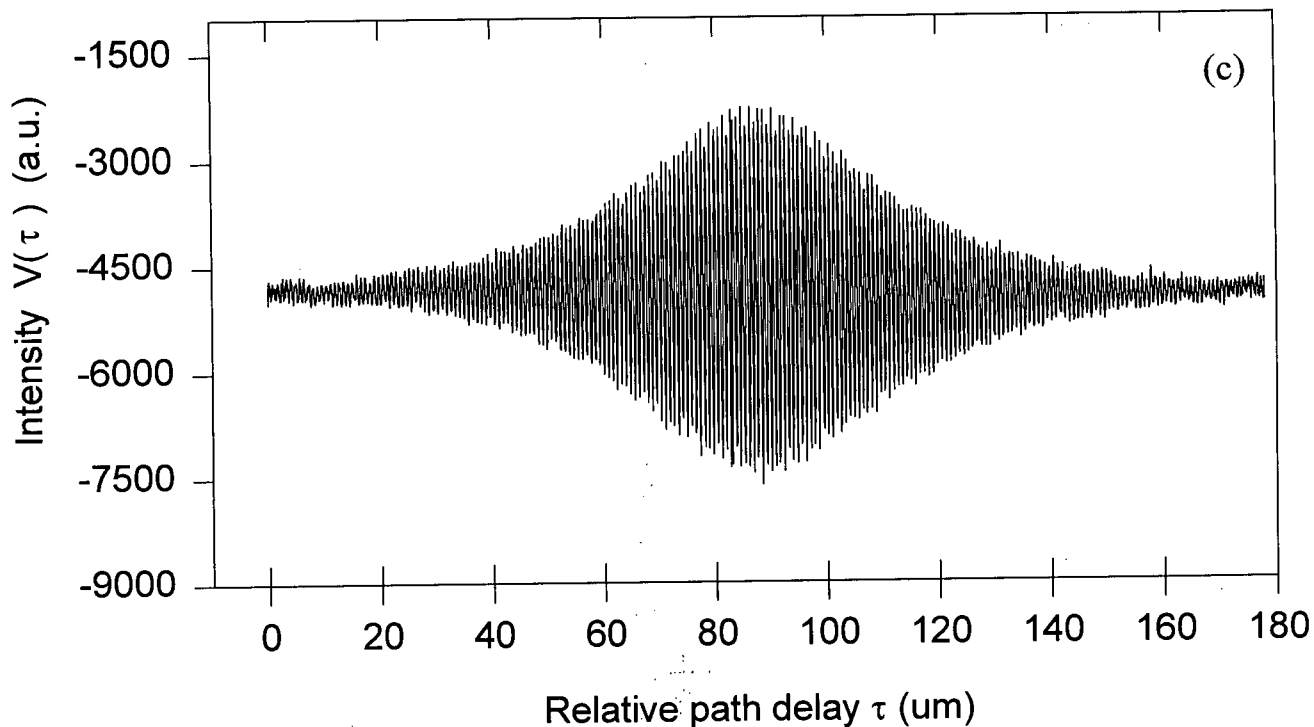


Fig.4.13 (c) The interferogram in relative path delay space generated from a well mode locked Ti:sapphire laser output.

4.3.2 CENTER WAVELENGTH AND PULSE DURATION

The basic algorithm for extracting the center wavelength was presented in Sect. 3.4.4 in Chapter 3. Here we show some results of the wavelength calibration of the pulsed output from the Ti:sapphire laser, and compare these with measurements using the Bomem FTIR system.

In this Ti:sapphire laser, the wavelength of the pulsed output is tuned by shifting the slit as shown in Fig.3.2. Fig.4.14 shows the wavelength as a function of slit position from this system and the system from Bomem. The agreement is excellent.

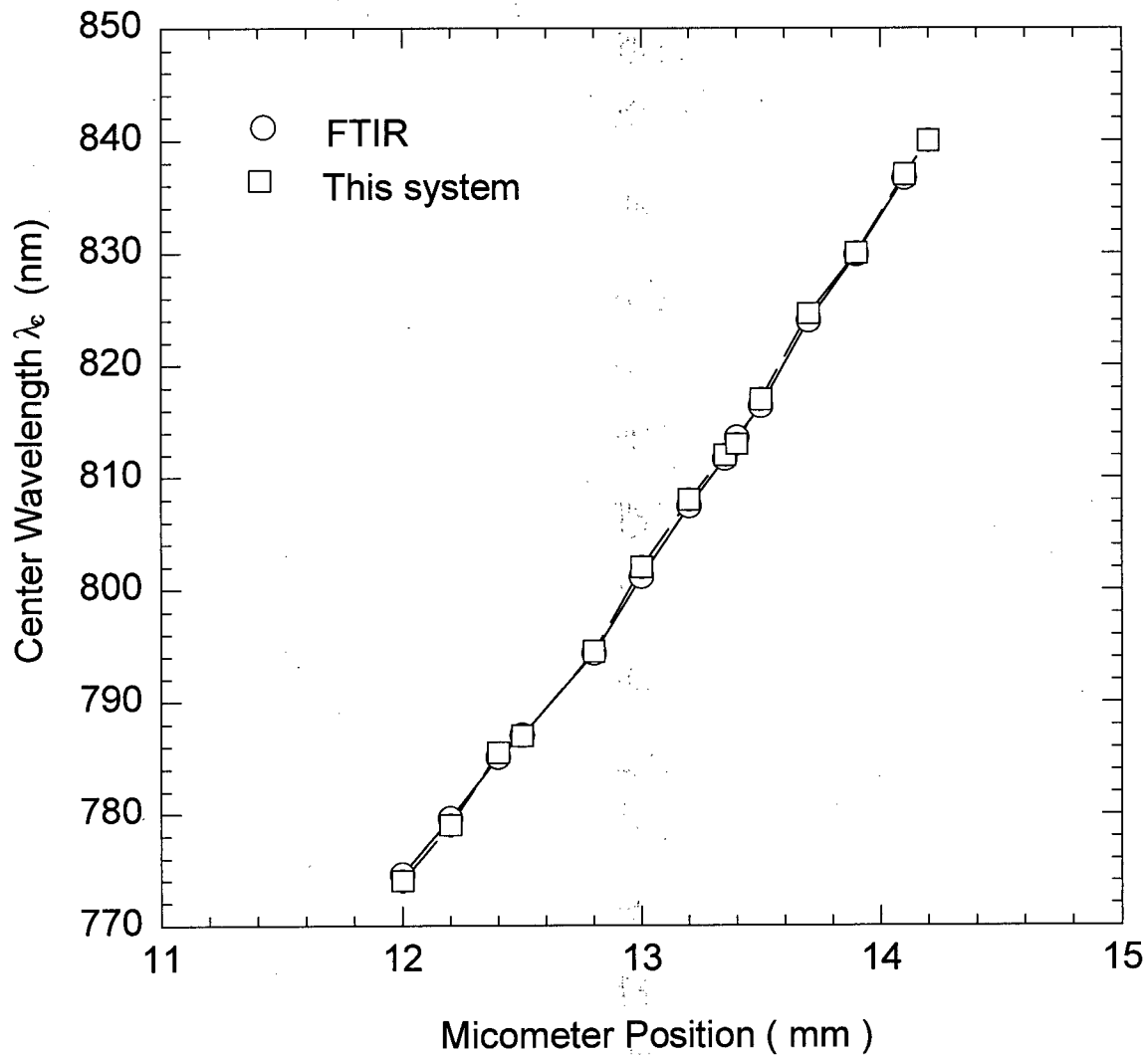


Fig.4.14 Center wavelength calibrations of the output pulses from a Ti:sapphire laser implemented by this system and the FTIR from Bomem Co.

A simple estimate for the pulse duration is obtained by assuming the pulse is transform-limited (i.e. set $\varphi_2 - \varphi_1 = 0$ and $f_1 = f_2 = f(t)$ in Eqn.(2.25)), and that the electrical field amplitude is represented by

$$f(t) = A \operatorname{sech}(-t/\tau_p) \quad (4.10)$$

where A is a constant and τ_p is the pulse duration parameter.

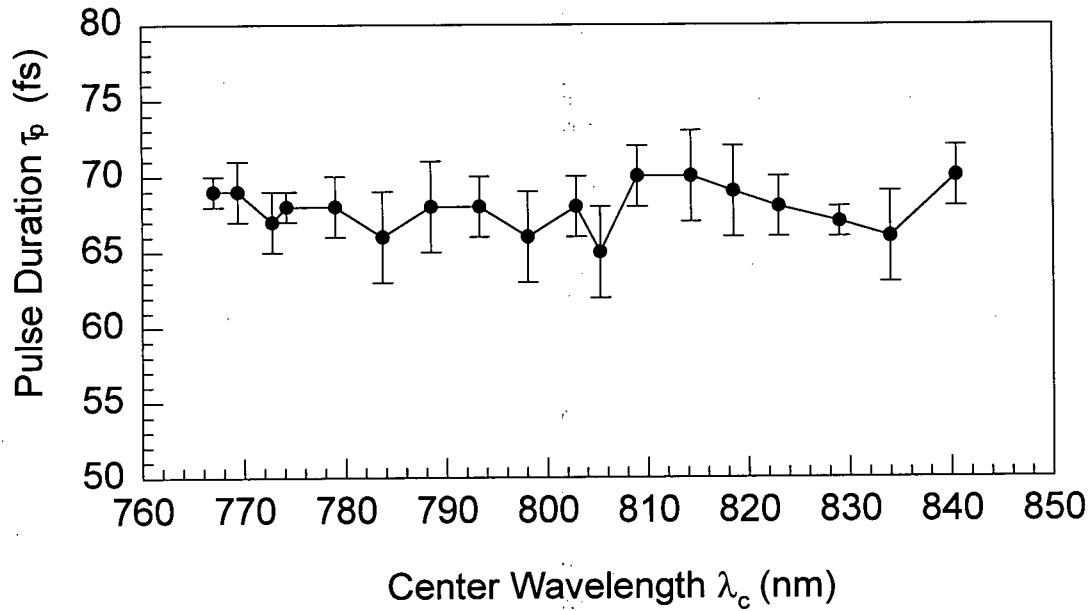


Fig.4.15 Pulse durations from a well-mode locked Tisapphire laser at different center wavelengths.

Putting Eqn.(4.10) into Eqn.(2.25), the pulse duration τ_p is related to $D_{1/2}$, the full width of the envelope of the auto-correlation interferogram, at the half maximum signal intensity in relative path delay space:

$$\tau_p = \frac{D_{1/2}}{0.839} \quad (4.11)$$

Fig.4.16 shows the experimental measurements of the pulse duration using this system, which shows that when the laser system is well mode-locked, the pulse duration is approximately independent of the center wavelength.

4.4 CROSS-CORRELATOR

As perhaps the simplest demonstration of the use of the system as a cross correlator, interferograms were obtained with 4 and 8 mm of quartz glass placed in the signal arm of the Mach-Zehnder interferometer. The imbalance introduced by the propagation of the pulses in one arm through the additional glass is detectable by its effect on the interferograms. As the extra glass affects only the phase of the pulses, this demonstrates the unique ability of the interferometric approach to extract phase information about the signal beam's electric field distribution.

4.4.1 INTERFEROGRAM

The plots in Fig.4.17 and Fig.4.18 show the single cycle interferogram for the cross-correlation between the reference pulse and that transmitted through 4 mm and 8 mm pieces of quartz glasses. For comparison, the auto-correlation interferogram (no glass) is shown in Fig.4.16. Fig.4.19 and Fig.4.20 show the envelopes and phase factors obtained by fitting these interferograms using polynomial model as outlined in Sect. 4.2.1. The effects of the phase modulation due to the quartz glass are small but detectable. Fig. 4.21 shows the difference between the envelopes as a function of relative path delay. These were obtained after normalizing the peaks of the interferogram envelope, each averaged over 4 scans. From Fig. 4.21, the perturbation to the realy symmetric reference envelope (no glass) has both symmetric and asymmetric components, the relative size of which depends on the thickness of the glass in a nonlinear fashion. The following section develops a model that describes the way in which the quartz glass is expected to modify the cross correlation interferogram.

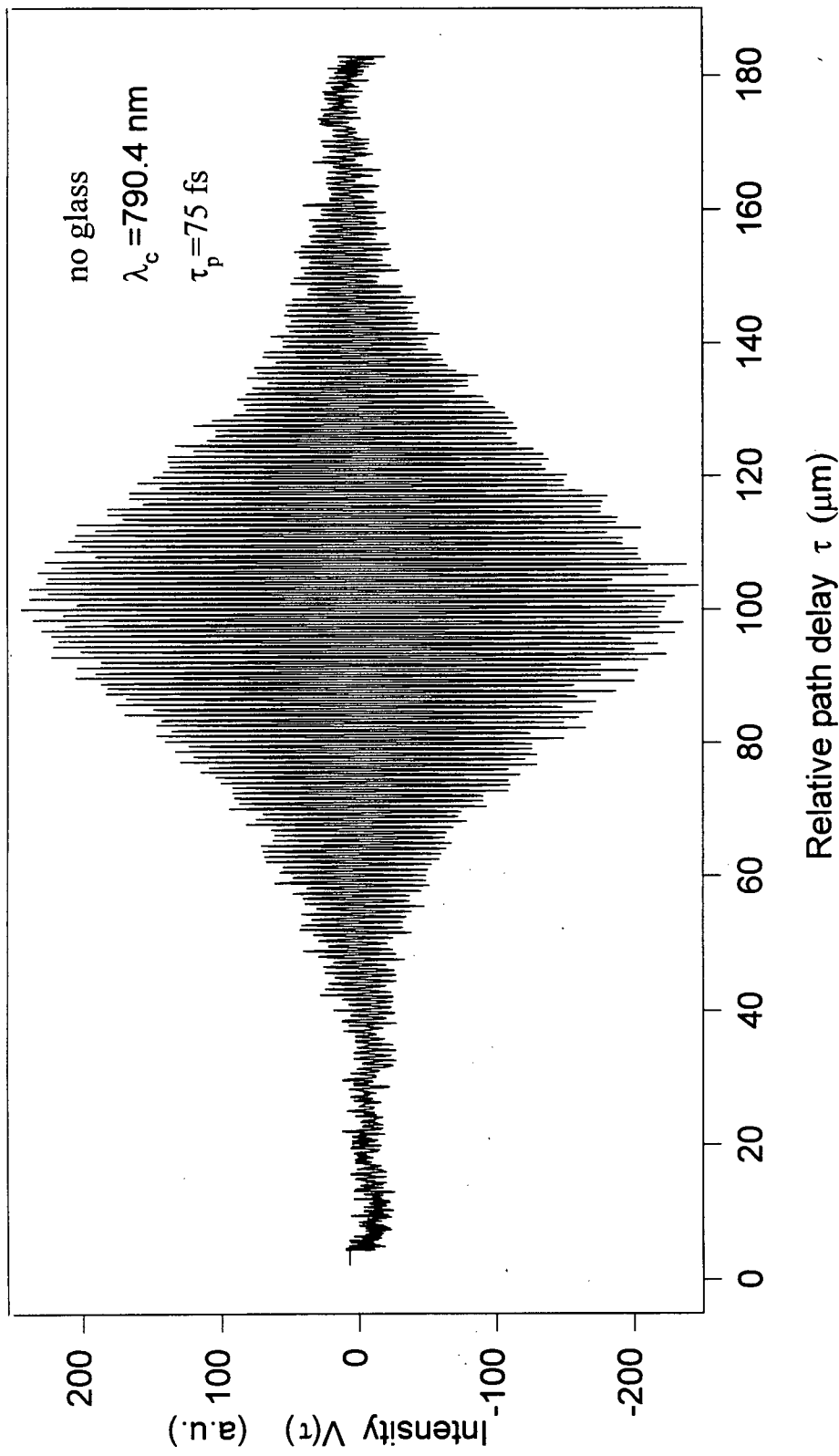


Fig.4.16 The autocorrelation interferogram from the pulse of duration τ_p of 75 fs and λ_c of 790.45 nm.

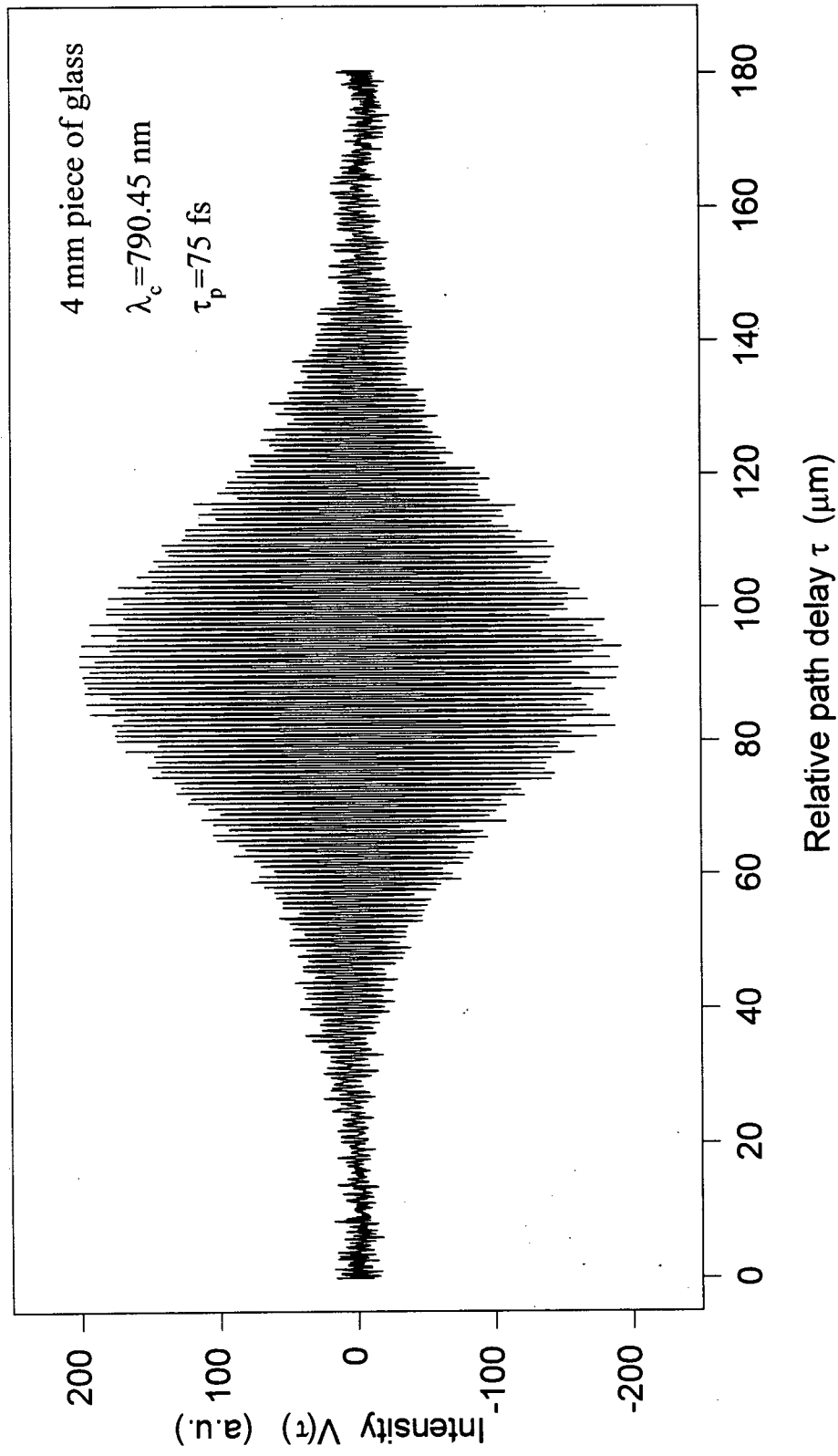


Fig.4.17 The cross correlation interferogram from the pulse of $\tau_p = 75 \text{ fs}$ and $\lambda_c = 790.45 \text{ nm}$ with 4 mm piece of quartz glass inserted in the signal path.

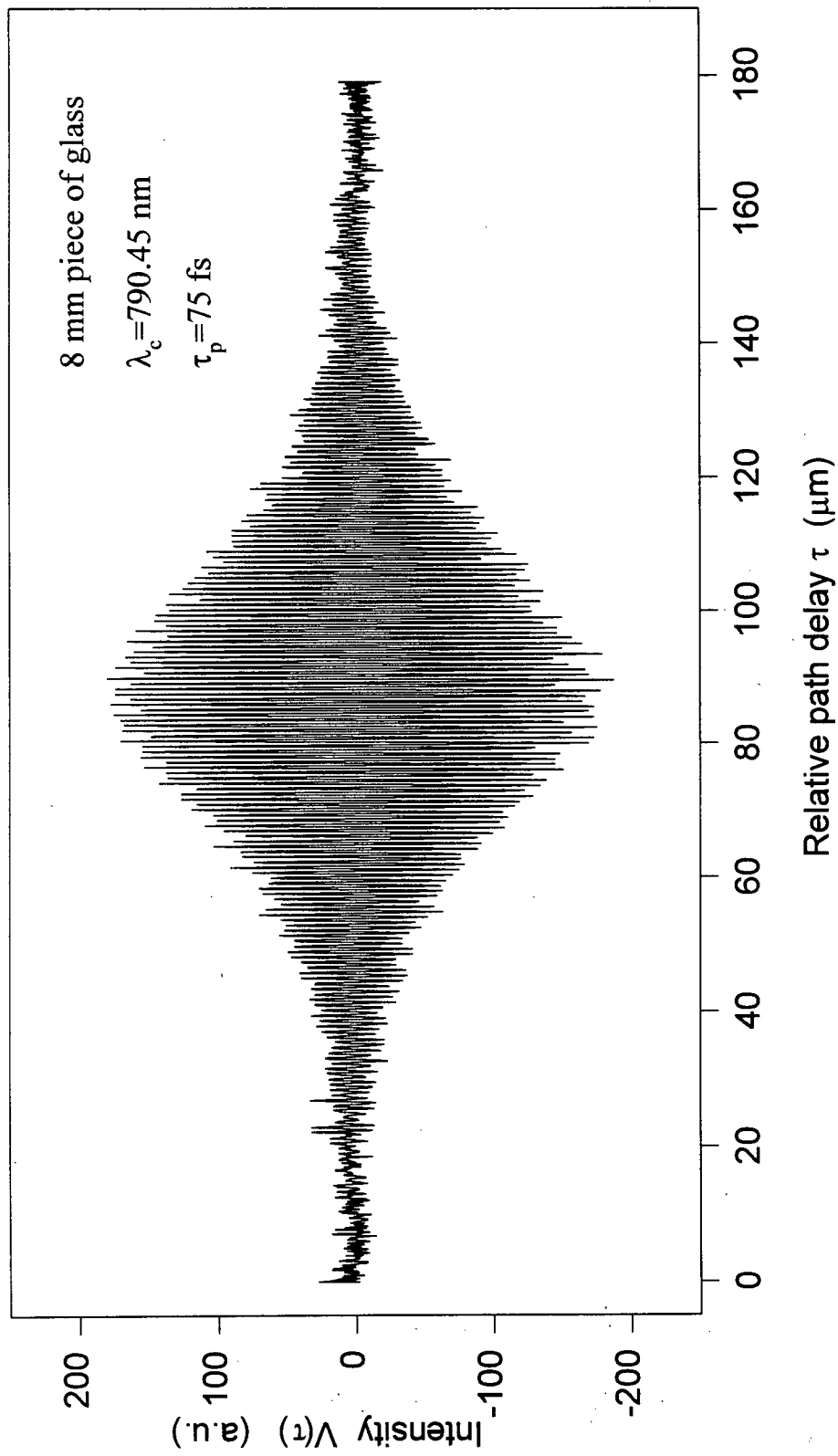


Fig.4.18 The cross correlation interferogram from the pulse of $\tau_p = 75 \text{ fs}$ and $\lambda_c = 790.45 \text{ nm}$ with 8 mm piece of quartz glass inserted in the signal path.

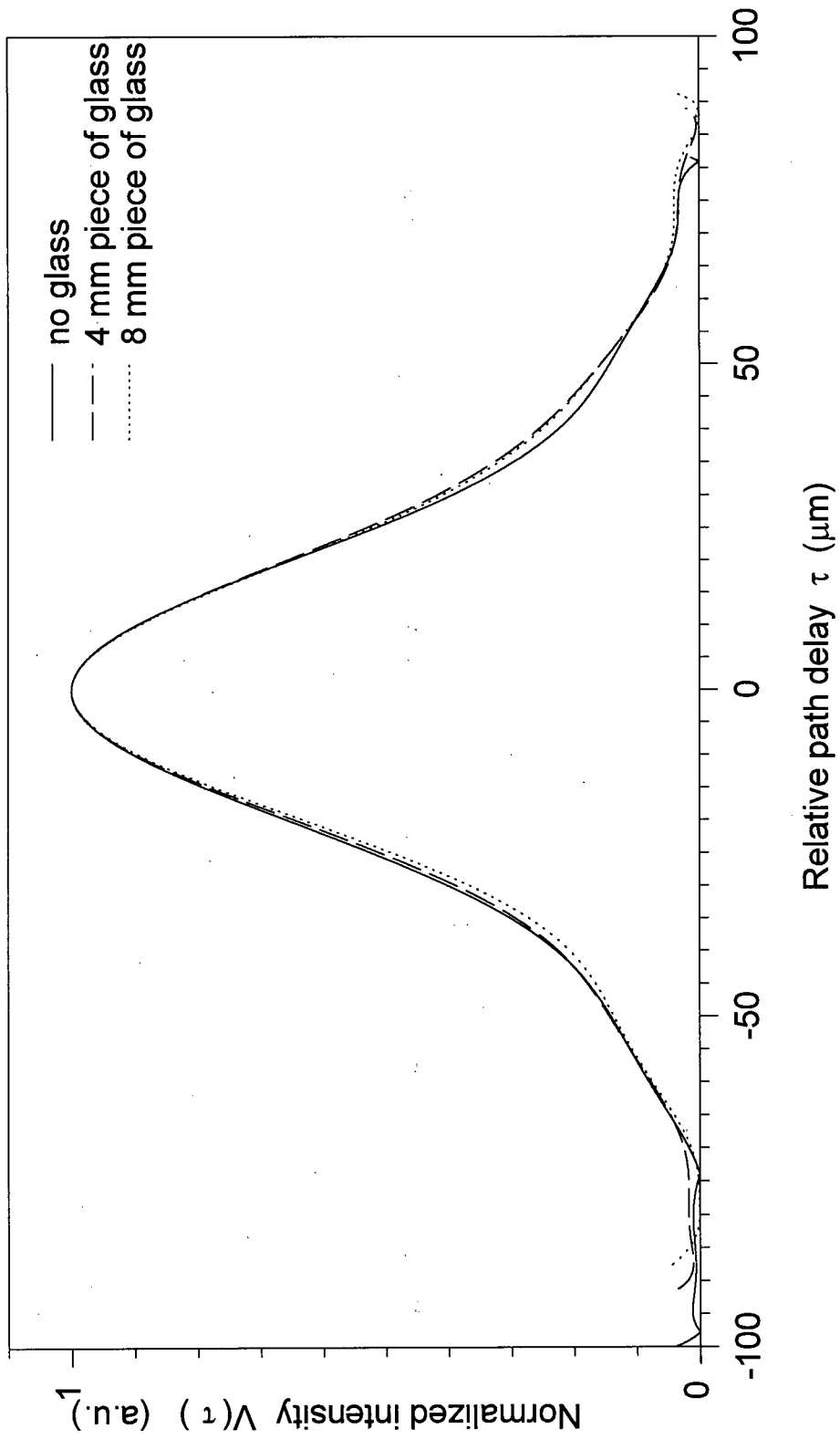


Fig.4.19 The envelopes of the interferograms in Fig.4.16, Fig.4.17 and Fig.4.18.

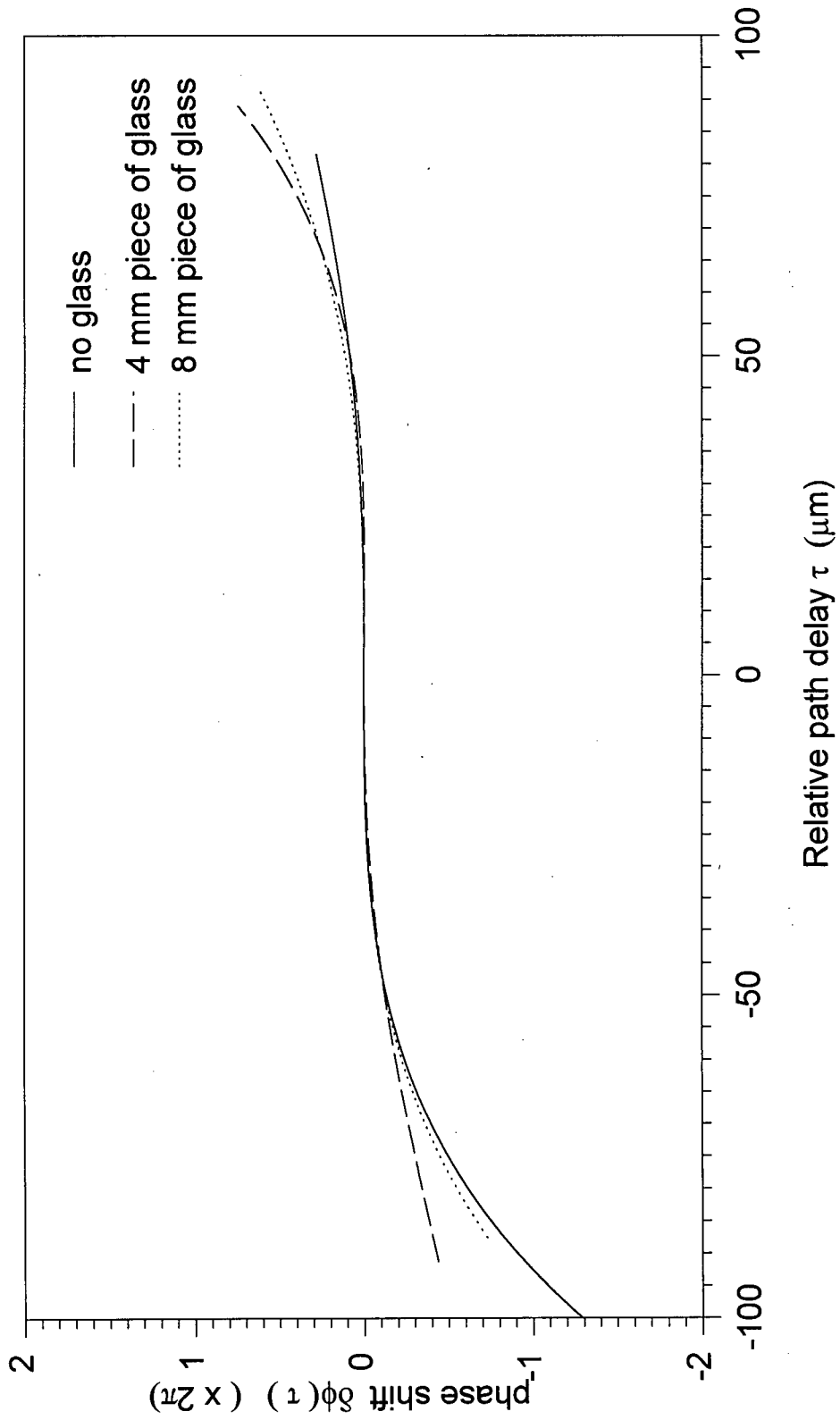


Fig.4.20 The phase shifts in the interferograms in Fig.4.16, Fig.4.17 and Fig.4.18.

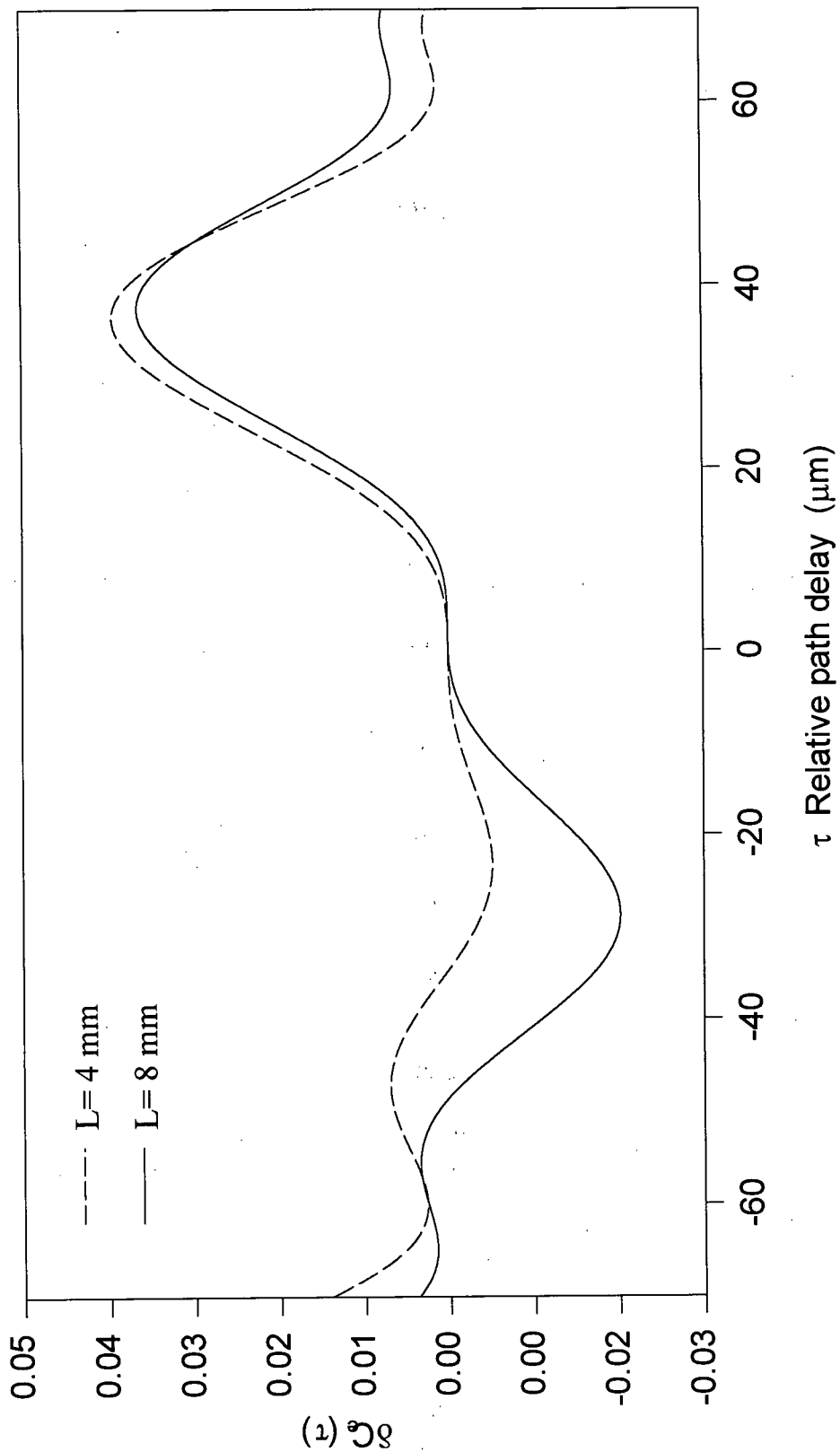


Fig.4.21 The difference between the envelope of the cross correlation interferogram with glass and that without glass as a function of the relative path delay.

4.4.2 ANALYSIS

Fig.4.22 shows the refractive index $n(\omega)$ of quartz glass in the frequency region around the center wavelength $\lambda_c=790.45$ nm of the laser pulse [Ref.31, P3-5]. A regression analysis shows that

$$n(\omega) = 1.45348 + 5.86315 \times 10^{-18} (\omega - \omega_c) \quad (4.13)$$

describes the data extremely well.

For the weak pulse power used in these experiments, the quartz glass is a linear optic material. For simplification, we only treat the effects of the quartz on the transmitted phase of the pulses; reflection loss are neglected. Then the fields from reference arm and signal arm can be

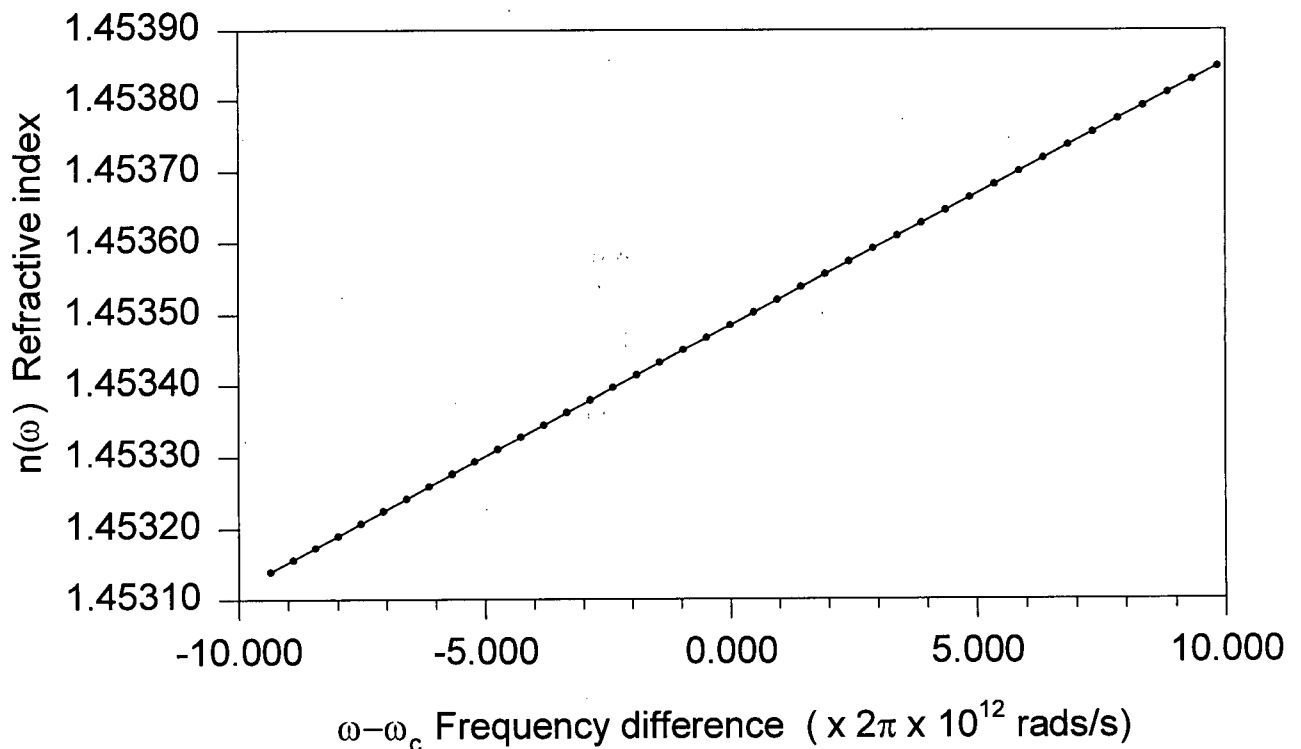


Fig.4.22 The refractive index n of quartz glass (fused silicon) in the region around the center wavelength $\lambda_c=790.45$ nm of the laser pulse.

written as

$$E_r(t) = \int_0^{\infty} d\omega \hat{E}(\omega) \cos[\omega t + \varphi_r(\omega)]$$

$$E_s(t) = \int_0^{\infty} d\omega \hat{E}(\omega) \cos[\omega t + \varphi_s(\omega)]$$
(4.14)

where $\hat{E}(\omega)$, $\varphi_r(\omega)$ and $\varphi_s(\omega)$ are real functions of frequency. $\hat{E}(\omega)$ has a pulsed-shape centered at ω_c . Putting Eqn.(4.14) into Eqn.(2.24), the cross correlation, we have

$$C(\tau) = \iiint d\omega d\omega' dt \hat{E}(\omega) \hat{E}(\omega') \cos[\omega t + \varphi_r(\omega)] \cos[\omega' t + \varphi_s(\omega')]$$

$$= \iiint d\omega d\omega' dt \frac{\hat{E}(\omega) \hat{E}(\omega')}{2} (\cos[(\omega - \omega')t] \cos[\varphi_r(\omega) - \varphi_s(\omega')] - \sin[(\omega - \omega')t] \sin[\varphi_s(\omega) - \varphi_s(\omega')])$$
(4.15)

With $\int dt \cos[(\omega - \omega')t] \rightarrow \delta(\omega - \omega')$, and $\int dt \sin[(\omega - \omega')t] \rightarrow 0$, finally we obtain

$$C(\tau) = \int_0^{\infty} d\omega \hat{E}^2(\omega) \cos[\omega\tau + \varphi_r(\omega) - \varphi_s(\omega)]$$
(4.16)

Let $\Delta\varphi(\omega) = \varphi_r(\omega) - \varphi_s(\omega) = \Delta\varphi_0(\omega) + \Delta\varphi_g(\omega)$, where $\Delta\varphi_0(\omega)$ is the intrinsic phase shift due to any (small) imbalance in the signal generating interferometer, and $\Delta\varphi_g(\omega)$ is the phase shift due to the glass inserted. From Eqn.(4.13), $\Delta\varphi_g(\omega)$ is equal to $\omega[n_0 + n_1(\omega - \omega_c)L/c]$. Thus quite generally

$$C(\tau) = \int_0^{\infty} d\omega \hat{E}^2(\omega) \cos \left[\omega(\tau + \delta\tau) - \theta + \left(\frac{\omega - \omega_c}{\omega_c} \right)^2 \theta + \Delta\phi_0(\omega) \right] \quad (4.17)$$

where $\delta\tau \triangleq (n_0 + n_1 \omega_c)L/c$, and $\theta \triangleq n_1 \omega_c^2 L/c$. Since the imbalance due to the quartz is much larger than that within the interferometer itself, we set $\Delta\phi_0(\omega) = 0$. Considering that typically $\delta\omega = \omega - \omega_c \leq 2\pi \times 5 \times 10^{12}$ rads/s, and $L \leq 8$ mm, then

$$\left(\frac{\omega - \omega_c}{\omega_c} \right)^2 \theta \Big|_{\max} = 0.154 \ll 1 \quad (4.18)$$

therefore

$$\begin{aligned} C(\tau) &= \int_0^{\infty} d\omega \hat{E}^2(\omega) \left(\cos[\omega(\tau + \delta\tau) - \theta] \cos \left[\left(\frac{\omega - \omega_c}{\omega_c} \right)^2 \theta \right] \right. \\ &\quad \left. - \sin[\omega(\tau + \delta\tau) - \theta] \sin \left[\left(\frac{\omega - \omega_c}{\omega_c} \right)^2 \theta \right] \right) \\ &\approx \int_0^{\infty} d\omega \hat{E}^2(\omega) \left(\cos[\omega(\tau + \delta\tau) - \theta] \right. \\ &\quad \left. - \frac{\theta}{\omega_c^2} (\omega - \omega_c)^2 \sin[\omega(\tau + \delta\tau) - \theta] \right) \\ &= \int_0^{\infty} d\omega \hat{E}^2(\omega) \left(\cos[\omega(\tau + \delta\tau)] \cos(\theta) + \sin[\omega(\tau + \delta\tau)] \sin(\theta) \right) \\ &\quad - \theta \int_0^{\infty} d\omega \hat{E}^2(\omega) \left(\sin[\omega(\tau + \delta\tau)] \cos(\theta) - \cos[\omega(\tau + \delta\tau)] \right) \\ &\quad + \frac{2\theta}{\omega_c^2} \int_0^{\infty} d\omega \omega \hat{E}^2(\omega) \left(\sin[\omega(\tau + \delta\tau)] \cos(\theta) - \cos[\omega(\tau + \delta\tau)] \right) \\ &\quad - \frac{\theta}{\omega_c^2} \int_0^{\infty} d\omega \omega^2 \hat{E}^2(\omega) \left(\sin[\omega(\tau + \delta\tau)] \cos(\theta) - \cos[\omega(\tau + \delta\tau)] \right). \end{aligned} \quad (4.19)$$

Thus,

$$\begin{aligned}
 C(\tau) &= C_0^S(\tau) \cos(\theta) + C_0^{AS}(\tau) \sin(\theta) \\
 &\quad - \theta [C_0^{AS}(\tau) \cos(\theta) - C_0^S(\tau) \sin(\theta)] \\
 &\quad - \frac{2\theta}{\omega_c} \frac{d}{d\tau} [C_0^S(\tau) \cos(\theta) + C_0^{AS}(\tau) \sin(\theta)] \\
 &\quad + \frac{\theta}{\omega_c^2} \frac{d^2}{d\tau^2} [C_0^{AS}(\tau) \cos(\theta) - C_0^S(\tau) \sin(\theta)]
 \end{aligned} \tag{4.20}$$

where $\tau' = \tau + \delta\tau$, $C_0^S(\tau) \triangleq \int d\omega \hat{E}^2(\omega) \cos(\omega\tau)$, and $C_0^{AS}(\tau) \triangleq \int d\omega \hat{E}^2(\omega) \sin(\omega\tau)$. $C_0^{S/AS}(\tau')$ will be symmetric/asymmetric, $dC_0^{S/AS}(\tau')/d\tau$ will be asymmetric/symmetric, and $d^2C_0^{S/AS}(\tau')/d\tau^2$ will be symmetric/asymmetric about $\tau = -\delta\tau$, thus

$$C(\tau) = C^S(\tau) + C^{AS}(\tau) \tag{4.21}$$

where

$$\begin{aligned}
 C^S(\tau) &= C_0^S [\cos(\theta) + \theta \sin(\theta)] \\
 &\quad - \frac{2\theta}{\omega_c} \sin(\theta) \left[\frac{d}{d\tau} C_0^{AS}(\tau) \right] \\
 &\quad - \frac{\theta}{\omega_c^2} \sin(\theta) \left[\frac{d^2}{d\tau^2} C_0^S(\tau) \right]
 \end{aligned} \tag{4.22}$$

which consists of symmetric terms in Eqn.(4.21), and

$$\begin{aligned}
C^{AS}(\tau) = & C_0^{AS} [\sin(\theta) - \theta \cos(\theta)] \\
& - \frac{2\theta}{\omega_c} \cos(\theta) \left[\frac{d}{d\tau} C_0^S(\tau) \right] \\
& + \frac{\theta}{\omega_c^2} \cos(\theta) \left[\frac{d^2}{d\tau^2} C_0^{AS}(\tau) \right]
\end{aligned} \tag{4.23}$$

which consists of the asymmetric terms in Eqn(4.21).

To compare this analysis with the experimental results, first note that θ for 4 mm and 8 mm quartz glass cases are very big. Thus it is not possible to Taylor-expand the $\sin(\theta)$ and $\cos(\theta)$ terms, and therefore the dependence of $C(\tau)$ will be nonlinear in L , and consistent with the results in Fig. 4.20 and Fig. 4.21. In particular, the relative contributions of the symmetric "corrections" to the originally asymmetric interferogram will depend on L . This is also qualitatively consistent with the results in Fig. 4.21 where for $L=4$ mm there are comparable contribution for symmetric and asymmetric corrections whereas for $L=8$ mm the asymmetric contribution dominates.

In conclusion, the effects of phase modulation can be easily measured with the cross correlation and they are qualitatively consistent with the theory.

CHAPTER 5 CONCLUSIONS AND SUGGESTIONS

5.1 CONCLUSIONS

This thesis describes the development and testing of a rapid-scan interferometric cross correlation system. The system includes a Michelson interferometer and a Mach-Zehnder interferometer that share a common arm with a length that is periodically modulated by mounting the end reflector on an audio speaker driven at < 25 Hz. The Michelson interferometer has a cw HeNe laser beam passed through it in order to provide a measure of the path delay introduced by the moving mirror. The Mach-Zehnder interferometer coherently combines reference pulses from a Ti:sapphire mode-locked laser with signal pulses derived from the reference pulses interacting with some systems of interest. The interferograms detected at the outputs of the two interferometers are recorded in a personal computer. Much of the work entailed developing software to transform the cross correlation signal from the Mach-Zehnder interferometer from real time space to relative path delay space, using the HeNe reference interferogram.

The performance of the system was tested by using it to obtain the auto-correlation of the reference pulses and the cross correlation of the reference pulses with pulses that were passed through several millimetres of quartz glass. The results of the auto-correlation tests, which essentially measure the power spectrum of the pulses, were compared with the spectra of the reference pulses obtained using a commercial interferometric spectrometer. These tests showed that the center wavelength was measured to an accuracy of four parts of 10^5 , and that the spectral shape was consistent with the resolution limit imposed by the scan range. By modelling the auto-

correlation interferograms using analytic pulse shapes, pulse-width parameters were obtained with errors of ~ 2 fs.

The cross correlation experiments demonstrated the ability of the system to distinguish relative phase differences down to at least 5.847 rads over the spectral extent of the pulses.

In summary, a personal-computer-based rapid scan interferometric cross correlator was successfully developed. It will be used for characterizing the amplitude and phase of femtosecond optical pulses derived from a variety of sources. The system is very flexible, and can easily be modified to serve as a rapid-scan non-interferometric pump/probe system.

5.2 RECOMMENDATIONS FOR FUTURE DEVELOPMENT

There are two principal drawbacks of the current system. The first is that the maximum scan range is limited by the maximum sampling rate of the ADC board in combination with minimum frequency at which the speaker can be reliably driven. Neither of these are fundamental limitations since higher-speed ADCs and custom-made scanners can be obtained at a cost. The second problem is the inability to co-add interferograms as they are acquired. The main reason for this is the non-ideal motion of the mirror caused by acoustic pick-up through the speaker.

Both of these basic problems could be solved by developing a custom scanner that moves at constant velocity except near the turning points, and that moves periodically on time scales of a few seconds (time enough to co-add tens or hundreds of scans). The decoding interferogram could then still be recorded, but only for the purpose of checking for any imperfections in the scanner motion that might have compromised the co-added interferogram. The constant velocity scans would also

solve the present problem of having to Fourier transform unevenly sample data in relative path delay time space.

REFERENCES

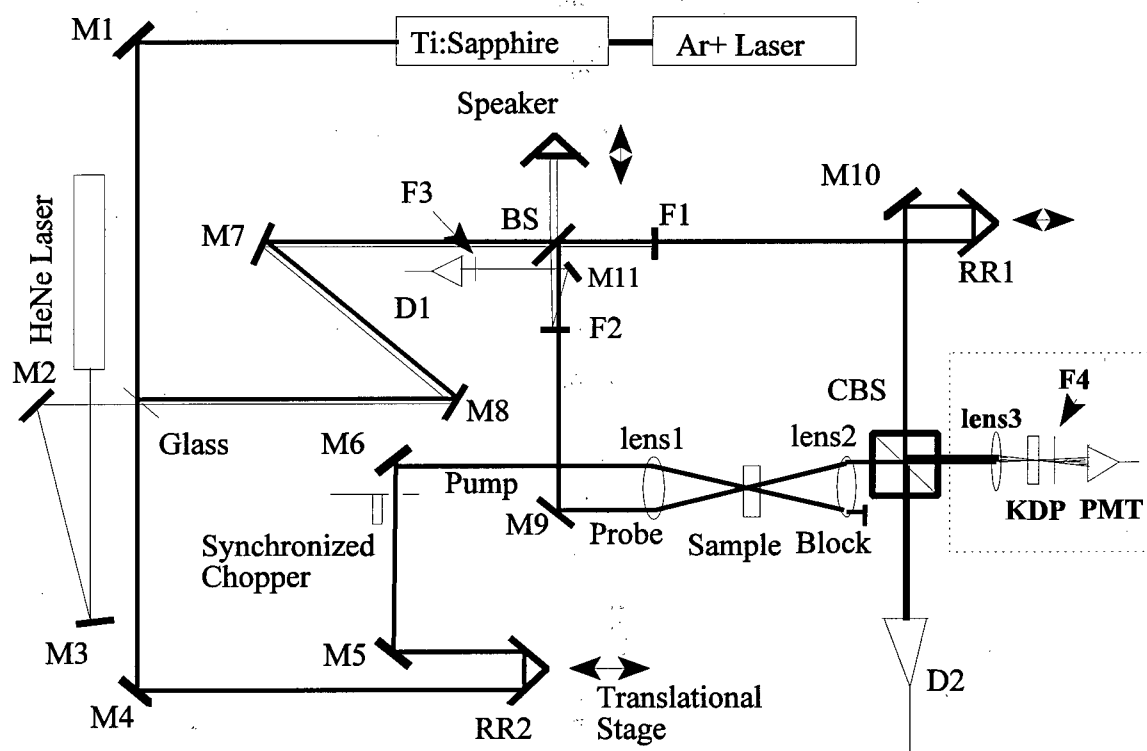
1. Ultrafast dynamics of laser-excited electron distributions in Silicon, J. R. Goldman, and J. A. Prybyla, *Phys. Rev. Lett.*, Vol 72, No.9, P1364-1367 (1994).
2. Femtosecond relaxation of localized plasma excitations in Ag islands, D. Steinmüller-Nethl, R. A. Höpfel, E. Gornik, A. Leitner, and F. R. Aussenegg, *Phys. Rev. Lett.*, Vol 68, No.3, P389-392 (1992).
3. Generation and detection of coherent optical phonons in Germanium, T. Pfeifer, W. Kütt, H. Kurtz, and R. Scholz, *Phys. Rev. Lett.*, Vol 69, No.22, P3248-3251 (1992).
4. Ultrafast optical evidence for resonance electron capture in quantum wells, M. R. X. Barros, P. C. Becker, D. Morris, B. Deveaud, A. Regreny, and F. Beisser, *Phys. Rev. B* 47, No.16, P10951-10954 (1993).
5. Coherent optical polarization of bulk GaAs studied by femtosecond photon-echo spectroscopy, A. Lohner, K. Rick, P. Leisching, A. Leitenstorfer, T. Elsaesser, T. Kohn, F. Rossi, and W. Stolz, *Phys. Rev. Lett.*, Vol 71, No.1, P77-80 (1993). 4. Ultrafast laser probe phenomena in bulk and microstructure semiconductors II, the Proceedings of SPIE, -- the international society for optical Engineering, ed. by R. R. Alfano, Vol 942 (1988)
6. Ultrafast phenomena VII, ed. by C. B. Harris, E. P. Ippen, G. A. Mourou, and A. H. Zewail, Springer Series in Chemical Physics 53, Springer-Verlag (1990).
7. Ultrafast phenomena VIII. ed. by J. -L. Martin, A. Migus, G. A. Mourou, and A. H. Zewail, Springer Series in Chemical Physics 55, Springer-Verlag (1993).
8. Ultrafast transport measurements in bulk semiconductors and tunneling devices using electro-optic sampling, K. E. Meyer, in *Spectroscopy of Semiconductor Microstructures*, ed. by G. Fasol, A. Fasolino, and P. Lugli, NATO ASI Series B, Physics Vol 206, P585-604 (1990).
9. Ultrafast optical nonlinearities of type II $\text{Al}_x\text{Ga}_{1-x}\text{As}/\text{AlAs}$ multiple quantum wells, J. Feldmann, E. Göbel, and K. Ploog, *Appl. Phys. Lett.*, Vol 57, No.15, P1520-1522 (1990).
10. Influence of scattering on the resonant transfer of holes between two-dimensional states, P. Brockmann, J. F. Young, Z. Wasilewski, and M. Buchanan, *Phys. Rev. B* 44, P13787-13790 (1991).
11. Photoluminescence up-conversion induced by intersubband absorption in asymmetric coupled quantum wells, P. Vagos, P. Boucaud, F. H. Julien, J. -M. Lourtioz, and P. Planel, *Phys. Rev. Lett.*, Vol 70, No.7, P1018-1021 (1993).

12. Ultrafast thermalization of photoexcited carriers in polar semiconductors, L. Rota, P. Lugli, T. Elsaesser, and J. Shah, *Phys. Rev. B* 47, P4226-4236 (1993).
13. H. T. Grahn, H. Schneider, W. W. Rhle, K. Von Klitzing, K. Ploog, *Phys. Rev. Lett.*, 64, 2426 (1990).
14. Control and measurement of ultrashort pulse shapes (in amplitude and phase) with femtosecond accuracy, J. -C. M. Diels, J. J. Fontairre, I. C. McMichael, and F. Simoni, *Appl. Opt.*, Vol 24, No.9, P1270-1282 (1985).
15. Analysis of ultrashort pulse-shape measurement using linear interferometers, V. Wong, and I. A. Walmsley, *Opt. Lett.*, Vol 19, No.4, P287-289 (1994).
16. Using phase retrieval to measure the intensity and phase of ultrashort pulses: frequency-resolved optical gating, R. Trebino, and D. J. Kane, *J. Opt. Soc. Am. A*, Vol 10, No.5, P1101-1111 (1993).
17. Femtosecond time-resolved interferometry for the determination of complex nonlinear susceptibility, K. Minoshima, M. Taiji, and T. Kobayashi, *Opt. Lett.*, Vol 16, No.21, P1683-1685 (1991).
18. Nonlinear optical pulse propagation in a semiconductor medium in the transient regime — I. temporal and spectral effects, N. Finlayson, E. M. Wright, and G. I. Stegeman, *IEEE J. Quantum Electron*, QE-26, No.4, P770-777 (1990).
19. Nonlinear optical pulse propagation in a semiconductor medium in the transient regime - II. interferometric sampling, N. Finlayson, and G. I. Stegeman, *IEEE J. Quantum Electron*, QE-26, No.4, P778-787 (1990).
20. Femtosecond pulse distortion in quantum wells, D. -S. Kim, J. Shah, D. A. B. Miller, T. C. Damen, W. Schäfer, and L. Pfeiffer, *Phys. Rev. B* 48, No.24, P17902-17905 (1993).
21. Coherent ultrafast nonlinear optical processes in semiconductor quantum wells, D. S. Chemla, *Solid State Comm.*, Vol 92, No.1-2, P37-43 (1994).
22. Ultrafast phase dynamics of coherent emission from excitons in GaAs quantum wells, D. S. Chemla, J. -Y. Bigot, M. -A. Mycek, S. Weiss, and W. Schäfer, *Phys. Rev. B* 50, No.12, P8439- 8452 (1994).
23. Instantaneous frequency dynamics of coherent wave mixing in semiconductor quantum wells, j. -Y. Bigot, M. -A. Mycek, S. Weiss, R. G. Ulbrich, and D. S. Chemla, *Phys. Rev. Lett.*, Vol 70, No.21, P3307-3310 (1993).

24. Measurement of photonic band structure in a two-dimensional periodic dielectric array, W. M. Robertson, G. Arjavalingam, R. D. Meade, K. D. Brommer, A. M. Rappe and J. D. Jeannopoulos, *Phys. Rev. Lett.*, Vol 68, No. 13, P2023-2026 (1992)
25. Rapid-scanning autocorrelator with extended scanning span for monitoring short optical pulses, A. Watanabe, H. Saito, T. Tokizaki, Y. Ishida, and Y. Yajima, *Rev. Sci. Instrum.*, 58, 1852 (1987).
26. K. L. Sala, G. A. Kenney-Wallace and G. E. Hall, *IEEE J. Quantum Electron*, QE-16, 990 (1980).
27. Rapid programmable 300 ps optical delay scanner and signal-averaging system for ultrafast measurements, D. C. Edelstein, R. B. Romney, and M. Scheuerman, *Rev. Sci. Instrum.*, Vol 62, No.3, P579-583 (1991).
28. Rate equation in semiconductor electronics, J. E. Curroll, Cambridge University Press 1985, P117-119.
29. Signals, Systems and communication, B. P. Lathi, John Wiley & Sons, Inc., Chapter 11, 1965.
30. AVI automotive series, AVI Sound International Ltd. 1993.
31. Optics guide 5, Melles Griot 1990, P17-29.
32. The art of electronics, 2nd., P. Horowitz, and W. Hill, Cambridge University Press, Chapter 1 and Chapter 5, 1990.
33. Newport catalog 1992, Newport Corporation, K-32.
34. User's Manual, Tsunami Mode-locked Ti:sapphire Laser, Spectra-Physics Lasers, Oct. 1992.
35. AT-MIO-64F-5, User Manual, National Instruments, October 1992 Edition.
36. A new method to measure the wavelength of single-mode pulsed lasers with a scanning Michelson interferometer, R. Chaux, *Appl. Phys. B58*, P63-67 (1994).
37. Labview™ VI reference manual, National Instruments, August 1993 Edition.
38. Numerical recipes, W. H. Press, B. P. Flannery, S. A. Teukalsky, and W. T. Vetterling, Cambridge University Press, 1990. (Levenberg-Marquardt Method)

APPENDIX A. CONFIGURATION FOR PUMP/PROBE INTERFEROMETRIC MEASUREMENT

Pump/probe technique is very popular in research on ultrafast phenomena. The pump/probe interferometric technique combines pump/probe technique and interferometric technique, takes their advantages and extends their ability from only amplitude measurement or phase measurement to the measurement of amplitude and phase simultaneously. Fig.A1 is the configuration for pump/probe interferometric measurement based on the cross correlator we developed in this thesis. The modification to the general configuration in Fig.3.1 is that instead of generated by the external apparatus, the signal pulse is the transmitted pulse from the studied system, which is optically or electronically modulated by the time delayed pump pulse. 92% of the fs output from Ti:sapphire laser goes through the slow scanner and synchronized chopper, and then is focused on the same spot on the studied system as is the other arm, the probe pulse, in the Mach-Zehnder interferometer. The pump pulse here is used to generate required optical and electronic states we intend to study in the studied system. In this testing system, as a slow scanner, a translational stage from Newport Co. provides the relative time delay between the pump pulse and probe pulse. The chopper is synchronized with the motion of the fast scanner to open or block the pump pulse radiating on the studied system. The design of the chopper driver will be discussed in Appendix B.



The speaker and translational stage are controlled by computer, and electronic signals from D1 and D2 are input to computer.

Fig.A1 System schematic for pump/probe interferometric measurement

APPENDIX B. SYNCHRONIZED PUMP BEAM CHOPPER PACKAGE

In this system, we use the waveform output from one of two output channels on board to trigger its data acquisition. In the configuration for pump/probe interferometric measurement, we also use it to drive the synchronous motor. Here there are two things need to consider. Firstly, the

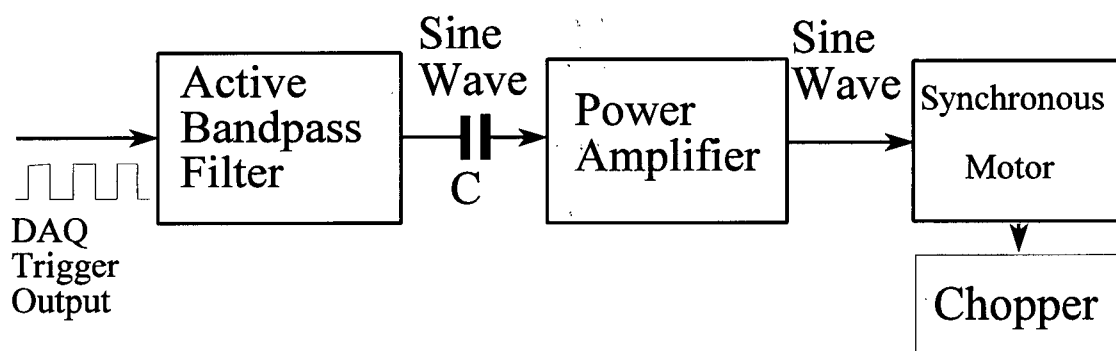


Fig. B1. Synchronized Chopper Package

triggering signal is square wave, which must be converted to sine wave before it is input to the motor to meet the operation requirement for the motor. Secondly, the function of the chopper here is to block the pump beam for one optical delay scan cycle, and open it for the next scan cycle, then the comparison between the interferograms acquired in both cycles will provide us the amplitude and

phase information about the optical and electronic process induced by the pump beam in the studied system. So the frequency of the chopper should be twice as that of the waveform driving the fast scanner and also the switch point between block and open for the chopper should match with the turn point of the fast scanner. To do these, we put an electronic processing package between the triggering output on board and the motor input. As shown in Fig. B1, this package consists of an active filter, and a power amplifier. We usually drive the fast scanner at 25 Hz. So, the active filter bandpasses 50 Hz with 1 Hz width to convert input square waveform to sine waveform of the same frequency, and it also amplifies the input voltage to meet the requirement for motor operation. The function of the power amplifier following the active filter is just to bust up the current to meet the power requirement for motor operation. The phase between the fast scanner driving channel and triggering signal channel is programmable, which can help us to phase match the fast scanner and the chopper. Fig.B2 shows the results, where Fig.B2 (a) is the input waveform to this package and Fig.B2 (b) is the waveform we got after the processing of this package. We can see that with square wave input to this package the output turns out to be high quality sine wave with the same frequency as that of input, and after test we can also find the phase shift between the input square wave and output sine wave is fixed, which is exactly what we want.

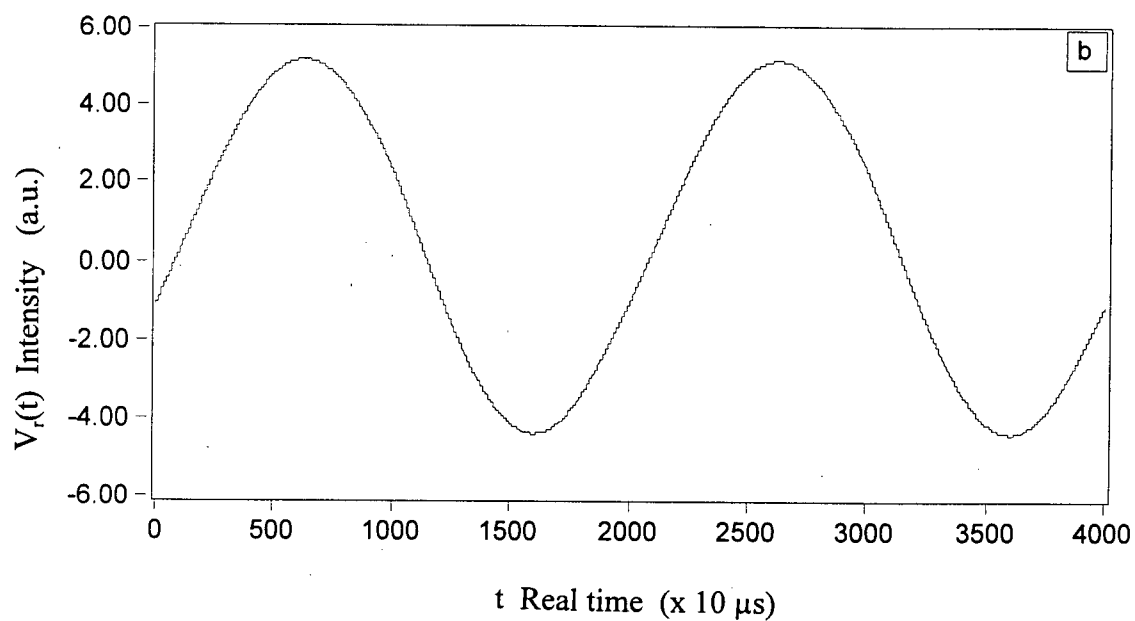
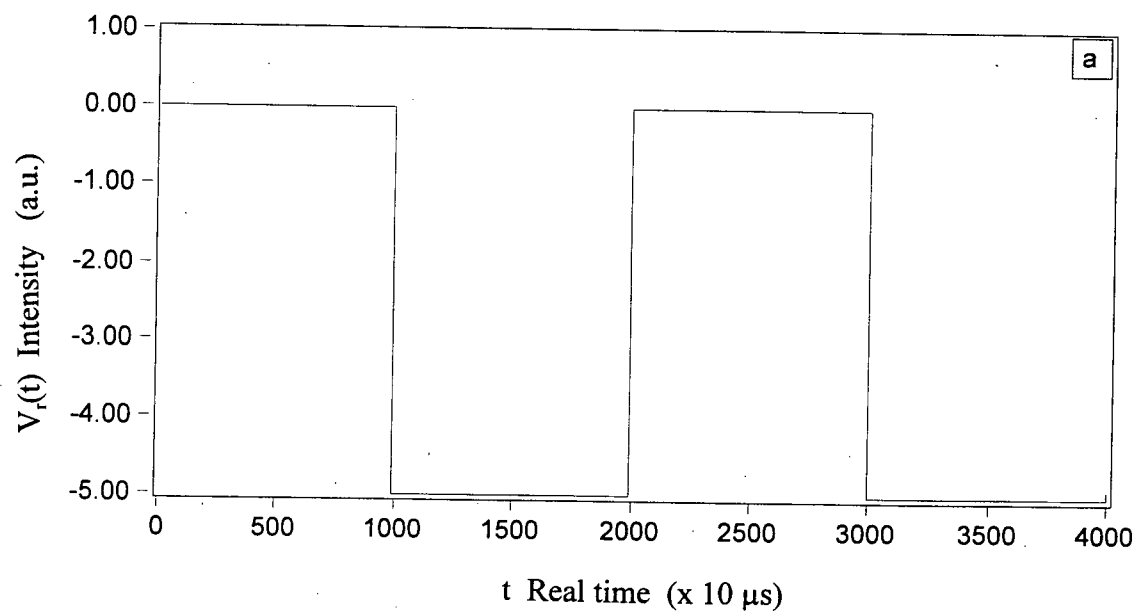


Fig.B2 (a) The input waveform to the synchronized chopper package at 50 Hz.
(b) The output waveform from the synchronized chopper package at 50 Hz.